RUI MIGUEL LOURENÇO ROCHA DE ALMEIDA

NMR STUDIES OF TRANSIENT PROTEIN COMPLEXES

LISBOA

2010

Nº DE ARQUIVO:

COPYRIGHT:

RUI MIGUEL LOURENÇO ROCHA DE ALMEIDA

NMR STUDIES OF TRANSIENT PROTEIN COMPLEXES

Dissertação apresentada para obtenção do

Grau de Doutor em Bioquímica,

especialidade Bioquímica Física,

pela Universidade Nova de Lisboa,

Faculdade de Ciências e Tecnologia

LISBOA

2010

Agradecimentos

Uma tese de doutoramento, embora corolário de quatro anos de esforço e dedicação individual, decerto não poderia ser levada a cabo com sucesso sem a importante ajuda de muitos intervenientes em diversos campos. Aqui deixarei o meu agradecimento a todos os que de alguma forma ajudaram ao sucesso desta desafiante mas estimulante tarefa.

Ao Prof. Doutor José J. G. Moura, meu orientador, agradeço-lhe ter-me acolhido no seu laboratório, e por fazer o seu melhor para estar sempre disposto a ajudar e apoiar, apesar dos seus muitos afazeres. O seu grau de dedicação à ciência e gosto pessoal pela área da química bioinorgânica servem como uma fonte de inspiração inesgotável.

À Doutora Sofia Pauleta agradeço o sua incansável vontade e rigor científico que me permitiram não só aprender bastante como também melhorar ao máximo o trabalho apresentado. Sem as suas valiosas sugestões, decerto este trabalho não teria sido levado a bom porto.

À Prof. Doutora Isabel Moura agradeço ter-me levado debaixo da sua asa e ensinado a purificar proteínas logo em tenra idade. Tive desde logo oportunidade de observar o seu estilo pessoal e inconfundível de fazer ciência, rigoroso, sério e pragmático, que serviu de grande fonte de inspiração.

À Prof. Paola Turano e ao Prof. Ivano Bertini (CERM, Universitá degli Studi di Firenze, Italia) agradeço a oportunidade de três meses de trabalho frutuosos em Florença, Itália, onde pude aperfeiçoar os meus conhecimentos de NMR bi-dimensional. Queria também aproveitar para agradecer aos Drs. Marco Allegrozzi e Leonardo Gonnelli todo o apoio técnico prestado, bem como as estimulantes discussões sobre a importância do Rui Costa no panorama do futebol mundial e da cidade de Florença em particular.

Ao Prof. Edgar Groenen, ao Dr. Peter Gast, à Jennifer Mathies e a todos os elementos do grupo MoNOs da Universidade de Leiden (Holanda), agradeço a magnífica oportunidade de ter passado uma semana a aprender elementos básicos de EPR de alta frequência.

A todos os membros dos grupos BioIn e BioProt, passados e presentes, entre estagiários e pós-docs e investigadores, agradeço-vos toda a ajuda prestada, quer profissional quer em termos pessoais. Sem a vossa ajuda este trabalho dificilmente teria dado tão bons frutos. Às vezes bastam pequenas coisas como facilitar a troca de um horário de utilização ou dar um olhinho por uma experiência que decorre para nos fazer sentir mais seguros e descansados. Por isso, Patrícia, Marta, Gabi, Pablo, Cristiano, Luísa, Célia, Alexandra, Florina, Jacopo, Simone, Ana Teresa, Raquel, Bruno, Carlos e Tiaguinho, obrigado por tudo – esta é para vocês. Destaco ainda o Rui Duarte, que me acolheu logo ao início e partilhou comigo conselhos importantes. Infelizmente, já não nos poderá acompanhar nesta parte final do trajecto…

Outras pessoas merecem também especial menção:

- Ao Filipe Folgosa (actualmente no grupo de Biofísica Molecular), agradeço o facto de me ter alertado para esta oportunidade de vir trabalhar para a REQUIMTE. Sem a sua amizade, espírito crítico (como bom algarvio emprestado como é) e boa-disposição, dificilmente conseguiria encarar os últimos anos com o mesmo sorriso. Obrigado também pelos momentos de gargalhada (alguns!).

- À minha correligionária Susana agradeço o facto de ter mantido presente o melhor sotaque do mundo™ no laboratório. Obrigado por todos os momentos de boa-disposição e carinho.

- Ao Américo agradeço toda a ajuda prestada na parte de Biologia Molecular e pela animação constante que a sua presença confere ao 6º piso.

- À Cristina Cordas agradecerei sempre os bons conselhos prestados, com aquela sapiência que só a experiência adquirida ao longo do tempo pode trazer.

- Ao Pedro e à Alice só posso agradecer toda a ajuda prestada, bem como as estimulantes discussões que versaram desde pormenores científicos relevantes até à eterna guerra entre PCs e Macintosh.

- Ao Ludi agradeço todo o tempo e ensinamentos partilhados comigo à volta do BiGGER.

Agradeço também profusamente ao Prof. Eurico Cabrita, ao Aldino Viegas e ao Daniel Jana todo o apoio técnico e sabedoria transmitidos sobre os novos AvanceIII 400 e 600 MHz, em especial quando surgiam estranhas mensagens de erro no ecrã de aquisição (algo muito recorrente para quem está habituado a trabalhar com software da Bruker). Agradeço-lhes também a amizade e solicitude que sempre demonstraram, e o sotaque algarvio que sempre me ajudou a sentir em casa. Não posso esquecer também os valiosos ensinamentos da Dra. Rosário Caras Altas, que me transmitiu as primeiras noções de NMR experimental no velhinho mas robusto AMX-400.

Não podia também deixar de agradecer aos restantes amigos e colegas da FCT que, de uma maneira ou de outra, ajudaram a que esta minha experiência se tornasse mais agradável ou completa. Leonor, Filipe Freire, Filipe Duarte, Inês & Inês, Vítor, e muito em especial, Engª Lúcia, Pedras, Carla e Marta, esta é para vocês.

Aos meus amigos, em especial o Pedro, o João ("Dr. Froufe"), o Daniel e o Barata, velhos companheiros de há longos anos, de outras batalhas e andanças, agradeço toda a amizade e a necessária perspectiva diferente das coisas.

Ao meu irmão Pedro e à minha mãe agradeço terem estado sempre presentes quando precisei, em momentos de maior dúvida. Adoro-vos. Mesmo apesar da insistente sugestão por parte do meu irmão que "Engenharia no Técnico é que é!».

Finalmente, queria também agradecer à Sílvia, a quem dedico esta tese. Sem todo o seu carinho e amor, bem como compreensão e infindável paciência, decerto não teria conseguido levar esta tarefa a tão bom porto.

Agradeço ainda à Fundação para a Ciência e Tecnologia a Bolsa de Doutoramento que me foi concedida (SFRH/BD/25342/2005) no âmbito do Programa Operacional Potencial Humano, da União Europeia (Fundo Social Europeu).

PROGRAMA OPERACIONAL POTENCIAL HUMANO
UNIÃO EUROPEIA Fundo Social Europeu
FCT Fundação para a Ciência e a Tecnologia
MINISTÉRIO DA CIÊNCIA, TECNOLOGIA E ENSINO SUPERIOR

Resumo

O trabalho descrito nesta tese versa sobre a utilização de sondas paramagnéticas no estudo de interacções protein-proteína (complexos transientes), e no desenvolvimento de metodologias para o mapeamento das superficies de interacção com base no efeito paramagnético causado pela presence de centros metálicos com electrões desemparelhados. Para esse efeito, foram utilizados em conjunto algoritmos computacionais e NMR 2D em sistemas marcados com ^{15}N.
O citocromo c_3 de *Desulfovibrio gigas*, uma proteína tetra-hémica, foi escolhida como proteína-alvo para estudar o efeito da sonda paramagnética, rubredoxina-Fe^{3+}, que causa alargamentos de linha específicos nas ressonâncias M2 e M18 do hemo IV. Os resíduos de rubredoxina envolvidos na interacção foram identificados por titulação NMR 2D. O citocromo c_3 possui uma superfície de lisinas carregadas positivamente em torno do hemo IV que atrai electrostaticamente a rubredoxina, que é acídica. Os complexos mais prováveis previstos por *docking* com restrições corroboram os resultados experimentais. Pequenas alterações conformacionais foram também detectadas no citocromo após ligação da rubredoxina. Esta interacção tem um K_d de 25 μM.

O potencial uso de duas sondas de Gd derivadas de cicleno, DOTAM (carregada positivamente) e DOTP (carregada negativamente), como indutoras de PRE (Aumentos de Relaxação Paramagnética) na determinação de interacções proteína-proteína foi estudada no modelo acima descrito. A complementaridade electrostática confere uma ligação específica da sonda Gd-DOTP junto ao hemo IV do citocromo c_3, causando fortes PREs nas ressonâncias dos metilos deste hemo. A interacção, baseada na diferença dos desvios químicos observados, tem um K_d = 20 μM. A sonda Gd-DOTAM interage especificamente com uma superfície bem-definida junto ao centro metálico da rubredoxina, causando fortes PREs, que são parcialmente revertidos com adição de excesso de citocromo c_3. Ambas as sondas revelaram-se causadoras de fortes PREs mesmo a longas distâncias (>10 Å), servindo como sondas eficientes e reversíveis para a identificação de superfícies de interacção.
A experiência previamente adquirida foi usada na determinação do complexo formado entre o redutase do superóxido (SOR) de *D. gigas* e os seus parceiros de transferência electrónica, rubredoxina e desulforedoxina. Este sistema é importante na destoxificação de espécies reactivas de oxigénio, formadas quando organismos anaeróbios são expostos a oxigénio. A interacção foi caracterizada por NMR 2D e cinética de estado estacionário. A superfície da rubredoxina envolvida no complexo de transferência electrónica com o SOR é constituída pelos resíduos adjacentes ao seu centro metálico (C9, V10, C42, G43, A44). O K_d estimado para esta interacção, a uma força iónica de 50 mM, é de 3.0 ± 0.4 μM. Um estudo sobre a dependência da velocidade de reacção com a força iónica revelou um k_{app} máximo de 37 $\underline{+}$ 12 min^{-1} a I = 150 mM. Embora não se tenha conseguido determinar um complexo definido entre o SOR e a desulforedoxina devido ao curto tempo de meia-vida do complexo na escala de tempo da espectroscopia de NMR, foi possível provar a ocorrência de transferência electrónica com um k_{app} máximo de 31 $\underline{+}$ 7 min^{-1} a I = 50 mM. Ensaios de competição por NMR 2D e cinética de estado estacionário usando Fe-desulforedoxina na presença de Zn-rubredoxina mostraram uma competição das duas proteínas pelo mesmo local de ligação à superfície do enzima, dado que foi corroborado *in silico* nos cálculos de docking da estrutura-modelo dos complexos.

Abstract

The work described in this thesis aims to study the utilization of paramagnetic probes in the study of protein-protein interactions (transient complexes) and the development of methodologies, using the paramagnetic effect due to the presence of a metal center with unpaired electrons, for the mapping of interacting surfaces. 2D-NMR in ^{15}N labelled systems in conjunction with computational algorithms was used to model the structure of those complexes.

D. gigas cytochrome c_3, a tetra-hemic cytochrome, was chosen as target to study the effect of the paramagnetic probe, Fe^{3+}-rubredoxin), which specifically broaden the resonances of the heme IV methyl resonances $M2^1$ and $M18^1$. The Rd residues at the complex interface were identified by heteronuclear 2D NMR titration. Cytochrome c_3 heme IV is surrounded by a patch of positive charges (lysine residues) that drives an electrostatic interaction with the negatively charged Rd. Indeed, predicted complexes obtained by restrained molecular docking shows a cluster of possible solutions near heme IV and small conformation rearrangements were detected upon binding of the two proteins, which as a dissociation constant of 25 μM.

Two cyclen-derived Gd probes, DOTAM (positively charged) and DOTP (negatively charged) were assessed as Paramagnetic Relaxation Enhancement (PRE)-inducing probes for protein-protein interactions, and tested in the previous model system. As predicted by electrostatic complementarity, in a NMR titration Gd-DOTP binds to cytochrome c_3 near heme IV, causing pronounced PREs in its heme methyl resonances. A K_d of 20 μM was determined based on chemical shift perturbation. Gd-DOTAM caused the same PREs on a well-defined patch near the metal center of rubredoxin. This effect was partially reversed when excess cytochrome c_3 was added to this system, mapping the interacting surface. Thus, both probes were successful in causing PREs at large distances from the binding site, serving as good, reversible probes for the identification of interacting surfaces.

The previous acquired experience was used to probe the complex formed between *D. gigas* superoxide reductase and two redox partners (rubredoxin and desulforedoxin). This molecular system is important in detoxification of reactive oxygen species, formed when the anaerobic bacteria is transiently exposed to oxygen. The interaction between SOR and its electron donors was probed by 2D NMR titrations and steady-state kinetics. The Rd surface involved in the electron transfer complex with SOR comprises the solvent exposed hydrophobic residues in the vicinity of its metal center (C9, V10, C42, G43, A44). The K_d for this interaction was estimated to be 3.0 ± 0.4 μM, at 50 mM ionic strength. An ionic strength dependence study on the activity was performed, showing maximum activity at 150 mM, with a k_{app} of 37 $\pm$ 12 min^{-1}. Although a complex between Dx and SOR could not be detected in a 2D NMR titration, due to the very short half-life of the complex in the NMR time scale, it was shown to be able to transfer electrons to SOR, with a maximum k_{app} = 31 $\pm$ 7 min^{-1} at I=50 mM. Kinetic assays and competition NMR experiments using Fe-desulforedoxin in the presence of Zn-rubredoxin showed that these two proteins compete for the same site on the enzyme surface, as shown in the model structure of the complex, using restrained molecular docking calculations.

Abbreviations

APSY – Automated Projection Spectroscopy

D. – Desulfovibrio

DOTAM – 1,4,7,10-tetraazacyclododecane-1,4,7,10-tetraacetamide

DOTP - 1,4,7,10-tetraazacyclododecane-1,4,7,10-tetrakis(methylenephosphonate)

Dx – Desulforedoxin

ET – Electron Transfer

FID – Free Induction Decay

HPLC – High-Performance Liquid Chromatography

HSQC – Heteronuclear Single Quantum Coherence

IPTG - Isopropyl-β-D-thio-galactopyranoside

LIS – Lanthanide Induced Shift

M. – Methanocaldococcus

MAS – Magic Angle Spinning

Ngr - Nygerythrin

nOe – Nuclear Overhauser Effect

NROR - NADPH:rubredoxin oxidoreductase

P. – Pyrococcus

PCS – Pseudo-Contact Shift

PDB – Protein Data Bank

PRE – Paramagnetic Relaxation Enhancement

Ps. - Pseudomonas

Rbr - Ruberythrin

Rd – Rubredoxin

RDC – Residual Dipolar Coupling

RMSD – Root Mean Square Deviation

ROO - Rubredoxin:oxygen oxidoreductase

ROS – Reactive oxygen species

SOD – Superoxide dismutase

SOR – Superoxide reductase

ssNMR – Solid State NMR

T. – Thermotoga

Tr. – Treponema

TROSY – Transverse Relaxation Spectroscopy

ZFS – Zero Field Splitting

General Index

Figures Index

Tables Index

CHAPTER I – GENERAL INTRODUCTION

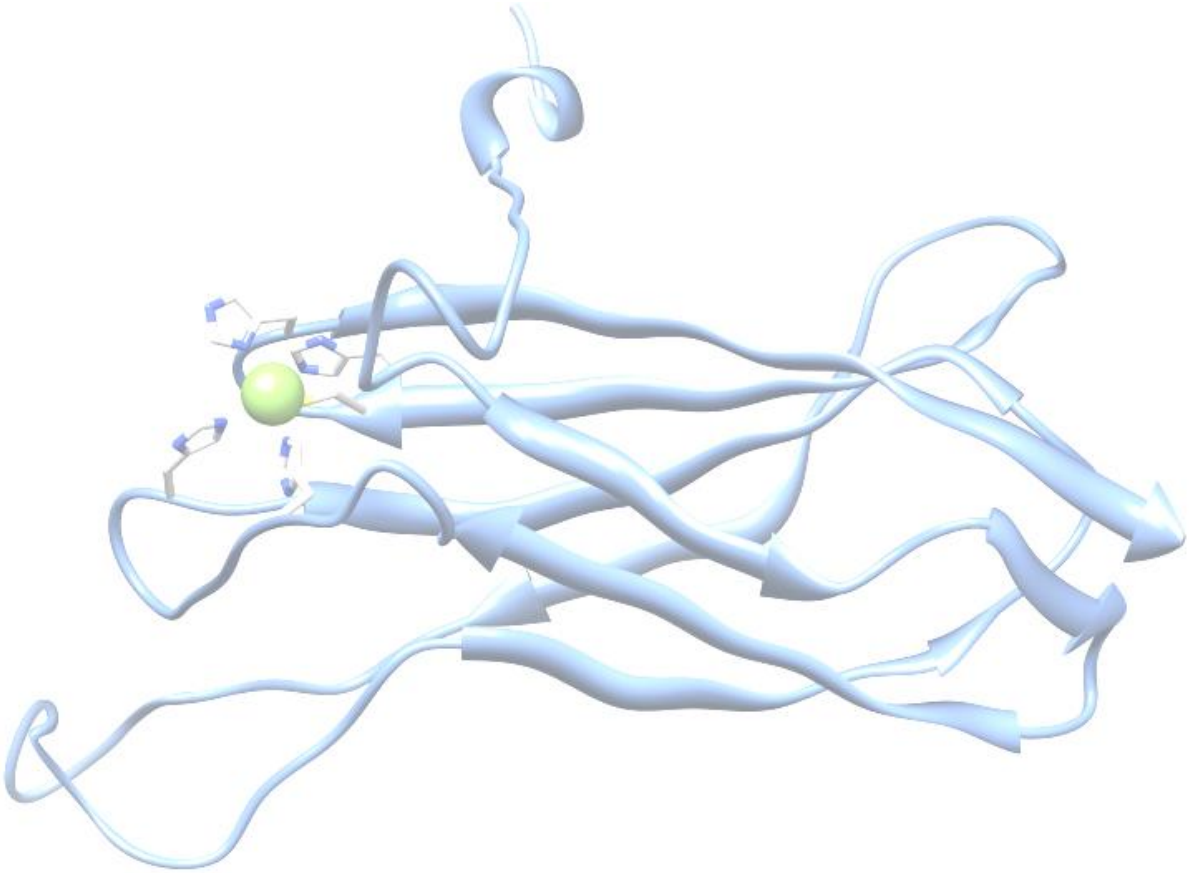

Anybody who has been seriously engaged is scientific work of any kind realizes that over the entrance to the gates of the temple of science are written the words: “Ye must have faith”.

- Max Planck

Index

I. General Introduction

Ever since oxygen started being produced by some early-developed microorganisms, the intracellular effects of reactive oxygen species (ROS) generated by incomplete reduction of this molecule became a problem for organisms, which were unprepared to deal with lipid oxidation, DNA damage and protein degradation. Radical anion superoxide ($O_2^{\cdot -}$) scavenging, among others, became tantamount with survival in an increasingly harsher environment for anaerobes when exposed to aerobic environments.

In this section, one of the enzymatic systems developed by anaerobes to overcome this oxidant burden, the superoxide reductase (SOR), will be briefly described, as well as its two putative physiological electron donors, rubredoxin and desulforedoxin. These two small electron transfer proteins, containing a simple FeS center, reduce the catalytic center of SORs to its ready state, among other electron transfer (ET) partners (*vide infra*).

The electron transfer ET complexes that are formed between SOR and its partners belong to a class termed weak or transient protein complexes. Therefore, they have a number of characteristics, such as very fast dissociation rate constants that has always made their analysis somewhat more difficult than for strong protein complexes.

This chapter will start by explaining the properties that govern the formation of protein complexes, with special focus on the subgroup of electron transfer complexes, and the techniques that can be applied to characterize them.

I.1 Protein complexes

In vivo, the function of most cellular processes involves the interaction between one protein and one or more protein partners. Hence, it is of the utmost importance to understand the way that proteins interact with each other and which factors influence or dictate the formation of these complexes. One of the current topics that draw the most interest in Biochemistry and Life Sciences, lies in the characterization of the interactome, coupled to systems biology. Since at the molecular and cellular level, biological structure and function are related to complex interactions between proteins and other molecules, there has been a renewed source of interest in this field with the aim to predict and validate all possible

protein interactions *in vivo*. To that effect, techniques such as genomic analysis, *ab initio* predictions using algorithms based solely on primary structure and domain conservation (although still with a very large number of false positives and negatives), or co-immunoprecipitation and yeast two-hybrid assays can be employed [1-5].

The affinity of these interactions can range from very specific to almost non-specific, and from the very tight (dissociation constant [K_d] values in the 10^{-15} M range) to the very loose (K_d in the 10^{-3} M range, where $K_d = k_{off} / k_{on}$). The most stable complexes are usually defined by very large complementary surface, and examples of these types of complexes include antibody-antigen interactions, and protease inhibitors - protease complexes.

On the other hand, pathways that require a high turnover for a controlled flow of substrate or electrons are usually populated/composed by complexes with low binding specificity [6]. This arises from the fact that these proteins need to interact with two (or more) partners, thus the forces that drive the formation of these complexes are necessarily different in nature. Hence, the k_{off} values need to be large in order to guarantee a high turnover, resulting in contact lifetimes that can be as short as 100 μs [7].

There have been numerous hypotheses put forward to identify the factors that govern protein association and dissociation in the case of electron transfer proteins. Poorly packed geometric surfaces may be responsible for this phenomenon. Furthermore, the presence of polar residues in the vicinity of the electron transfer centers may help in the re-solvation process which is essential for the dissociation process. Usually, the electron-transfer assembly is formed by surface charge complementarity between the two partners acting as a tether or pre-orientation step, resulting in an ensemble of possible conformations known as the encounter complex, which is characterized by a reduction in the dimensionality of the diffusional search [6, 8]. The hydrophobic patch will then confer specificity and increased affinity, resulting in enhanced rates of electron transfer when compared to chance encounters.

I.2 Characterization of Transient Protein Complexes: Electron-Transfer Proteins

ET protein complexes are notoriously difficult to co-crystallize due to the weak interaction between the partner proteins, which can be disrupted by the crystallization conditions or eventually end up co-crystallizing the complex in a non-physiologically relevant structure [9]. One alternative that has been on the rise since the mid-1990's to characterize these complexes consists of multidimensional NMR experiments. In these experiments one can follow the effect on the resonances of one protein upon binding of its partner (another protein or a ligand) and thus extract information on the surface of interaction, K_D or even make use of nuclear Overhauser effect (nOe) restraints to calculate the structure of the partner proteins upon complex formation. NMR methods, however, can be cumbersome and time-consuming – the cost of over-expressing ^{15}N and/or ^{13}C-labelled proteins aside, backbone resonance assignment must be performed on at least one of the interaction partners, but preferably on both, a task that becomes increasingly difficult with the increased size of the protein. Furthermore, increase in tumbling times resulting from complex formation can result in severe line broadening (not to mention spectrum crowding), thus hampering a straight-forward analysis of the obtained spectra. However, in the last decade a range of new NMR methods have been developed to help overcome these effects (section I.5).

One of the most used NMR experiments is the Heteronuclear Single Quantum Coherence (HSQC), which establishes a correlation between the proton and the nitrogen (^{15}N isotope) of an amine or amide group. In a ^{15}N-labeled protein, the HSQC spectrum gives rise to roughly as many resonances as there are amino acid residues, thus being considered the "fingerprint" of the protein. Briefly, by a combination of scalar coupling and pulse sequences, coherent resonance is transferred from the proton to the nitrogen and back before acquiring the free-induction decay (FID) signals, after a certain time of evolution according to the chemical shift (t_1). By varying t_1 systematically a determined number of times, one can obtain several ^{1}H spectra that are effectively modulated by the ^{15}N chemical shift [9]. Fourier transformation applied to the frequency domain of the resulting FIDs will yield a plane containing the relevant amide resonances (all the amides from the peptide bonds minus the prolines, plus all the resonances from side chain NH groups, such as

glutamine, asparagine and tryptophan), with one axis representing the ^{15}N chemical shifts, and the other the ^{1}H chemical shifts.

A typical NMR-based methodology for complex characterization revolves around chemical shift perturbation mapping. In this experiment, a ^{15}N-labelled protein (or, in rare cases, a protein with special, well-resolved resonances, such as cytochrome c_3 used in Chapters II and IV that has several resonances belonging to the heme methyl groups shifted downfield due to the paramagnetism of its Fe center, described in more detail below) is titrated against an unlabelled partner. By monitoring the chemical shift changes of amide proton resonances that echo the changes in the chemical environment, one can establish the region of interaction [10]. Furthermore, titrations can also help establish the stoichiometry and affinity of the complex by fitting observed chemical shifts or linewidth broadenings to a quadratic equation that depends on the dissociation constant (K_d).

However, the short interaction time of some of these complexes and/or the existence of several, dynamic, short-lived (ns to μs) functional ET orientations of both partners can lead to small or virtually undetectable chemical shift differences. In this case, other techniques based on ^{15}N spin relaxation can provide information about the encounter-complex formation by establishing the change in correlation time and changes in local dynamics reflected on the relaxation rate constants R_1 and R_2 (longitudinal and transverse relaxation, respectively). Cross-saturation transfer techniques (Fig. I.1 A) (in which one of the partners is perdeuterated) take advantage of the spin-diffusion effect caused by irradiating a specific region of the non-deuterated partner (usually the methyls region at ~1 ppm) onto the binding partner, thus decreasing its signal intensity. Finally, paramagnetic relaxation enhancements (PRE) can also be used to predict the binding interfaces of very weak complexes (Fig. I.1, see also chapters II, III and IV).

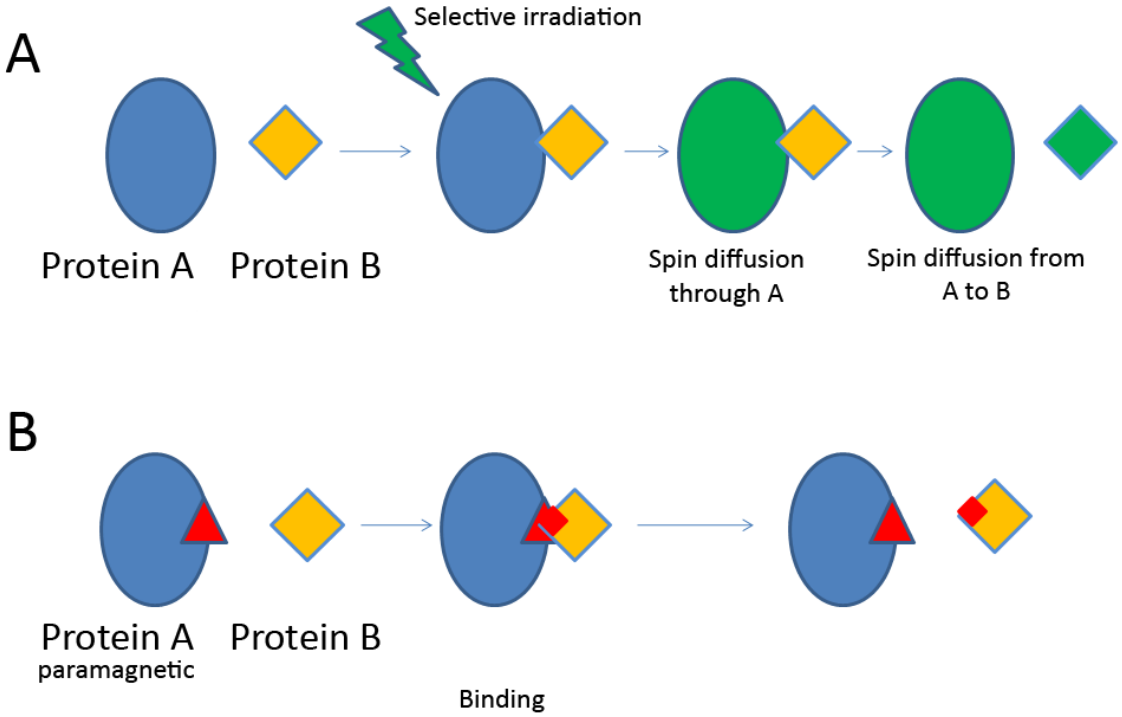

Figure I.1 – A) Schematic representation of a Cross-Saturation Transfer experiment. Resonances of a non-deuterated partner (Protein A) are selectively irradiated until saturation. Spin-diffusion phenomena will transfer said saturation throughout the polypeptide chain. Upon binding of a perdeuterated partner (Protein B), and depending on the intensity and time of irradiation, the saturation will be transferred either to the interacting residues, or to the whole protein, enabling the identification of the binding region. B) A partner with a paramagnetic center or probe (A) will cause pseudo-contact shifts (PCS) and PRE to a partner (B) that binds at or near the paramagnetic site. Since these effects are distance dependent, this allows the mapping of the interacting surface.

I.3 NMR applied to biomolecules – state of the art and latest developments

NMR has become an incredible and robust tool for investigating matter, ranging from powder solids to dilute macromolecules in solution, from 3D body imaging to inorganic chemistry. All stemming from the same principle: the behavior of magnetization of nuclei with $I \geq 1/2$ in an applied external magnetic field, when a radio-frequency pulse is applied. Techniques that allow the researcher to assign resonances and determine the three-dimensional structure of small proteins have become standardized in the past two decades. Overexpression and purification of single or double-labeled (^{15}N and ^{13}C) proteins has become an increasingly easier process, and the pulse sequences needed for a complete

determination of resonance assignment (2D HSQC, 3D HNCO, HNCA, HNCACO, among others) and distance constraints (NOESY) are readily available and easier to implement. Recent years have also seen the development of spectrometers with more potent magnetic fields (up to 23 T at the moment) and cryo-cooled probeheads that enable increased resolution and sensitivity, crucial aspects thatfor larger systems that require the correct assignment of closely co-localized resonances, as well as for less concentrated samples.

X-ray crystallography has been the preferred method for protein structure determination. In the PDB, the structures solved by X-Ray outnumber the NMR-solved structures by 7 to 1 (as of September 2010). X-ray crystallography, however, presents a series of drawbacks: membrane proteins require lipid bi-layers and the right combination of detergents for stabilization, rendering their crystallization a much more difficult task [11, 12]. Likewise, it is a harder task to garner insight about molecular dynamics from the static nature of crystals (though there are several examples of mechanism elucidation of enzymes by analyzing crystals obtained in different steps of the mechanism [13, 14]). Furthermore, the structure of complexes, especially weak-binding ones, becomes increasingly difficult to calculate due to the disruption of the interactions by crystal packing forces. In addition, these structures reflect the state of minimum energy, which may not reflect the actual complex *in vivo*. NMR has proved to be a viable alternative to overcome these difficulties in complex characterization. Solid State NMR (ssNMR) can be applied to magnetically-aligned lipid layers containing membrane proteins, taking advantage of the anisotropy of magnetic interactions to infer structural constraints [15]. Magic Angle Spinning (MAS) NMR, in which samples are spun at the magic angle (54.7º) thus eliminating one of the components responsible for fast relaxation (see chapter III), also becomes useful in larger systems for extensive resonance assignments, as they produce narrow lines [16]. Transverse-relaxation optimized pulse sequences, such as TROSY [17, 18] may also prove helpful in these cases.

Since most of the broadening effects are dependent on the gyromagnetic ratio of the observed nucleus (according to the relevant Solomon-Bloembergen equations [19]), direct detection of heteronuclei such as ^{13}C instead of ^{1}H will lead to narrower bands [20]. Finally, the recent development of fast methods such as SOFAST-HMQC and APSY [21], which take advantage of reduced sampling in the indirect dimensions, can help decrease the acquisition

time of spectra (plus the probability of protein degradation and the associated costs) from several days to within a few hours for smaller subjects.

Furthermore, since most ET complexes possess metal centers that are paramagnetic in nature, the added NMR spectral effects were also considered a nuisance (line width broadenings, enhanced chemical shifts; see below for further details). In recent years, however, paramagnetic effects have also been taken as an advantage in numerous aspects of biomolecular NMR. Indeed, in the present work, the paramagnetic effects of metal centers and lanthanide probes will be used to describe the binding surfaces. This will be achieved by analyzing quantitatively and qualitatively the presence and magnitude of both chemical shifts and resonance broadening.

I.4 *In silico* docking

Ab initio docking studies can also be used to predict the structure of a complex from which no information about relative orientation of the proteins is known *a priori*. Using the structures of the interacting proteins in their free form as a starting point, docking algorithms will search the conformational space of one protein (the target) by varying the orientation of the other (the probe), calculating and ranking several aspects of the interaction, including (but not limited to) steric complementarity of the interaction sites, electrostatic energy minimization upon binding, and hydrogen bonding [22-24]. It can also be used to validate complex geometries calculated based on experimental work, or incorporate information from it for docking refinement – the so-called restrained docking approach.

Several docking algorithms are currently available (reviewed in detail in [25]). In general, they all operate in a similar manner: starting from protein structures deposited in databases, such as the Protein Data Bank (PDB), the algorithms will try to move one molecule (the probe) in all six degrees of freedom (rotational and translational) relative to the other protein (the target), calculating in each step several parameters, such as Coulombic charge repulsion, accessible solvent area and geometric complementarity. Experimental restraints, such as definition of interaction surface residues by NMR titrations, or identification of key

residues for the interaction by site-directed mutagenesis can help filter out wrong solutions by limiting the search to complexes that do not violate these restraints.

Others may include refining steps after the initial searching methodology, by allowing the most probable structures some conformational mobility, reflecting the small conformational changes that are likely to occur *in vivo* [25]. Since it is unfeasible to calculate all possible conformations, flexibility is usually restricted to the side-chains of surface residues.

Scoring is also a key point in *in silico* protein docking. Usually, docking algorithms will present the lowest energy solutions as the top putative complexes. In order to ensure that this calculation is indeed correct, several individual (referring to an atom) or collective (referring to the entire macromolecule) parameters can be used: steric complementarity, electrostatic energy repulsion minimization, and hydrogen bonding.

BiGGER is one of these algorithms [26, 27], which was developed in Prof. Moura's laboratory in the past decade, and the one chosen here to perform the molecular docking studies. Its main advantages over other docking software include fast computational time and no need of any *a priori* information or constraints. The mode of action of this algorithm will be described in further detail on subsequent relevant chapters (chapters II and III). Other algorithms available (such as HADDOCK or RosettaDock) can present a subset of other functionalities (side-chain and backbone mobility, simulated annealing) that can, in theory, help in predicting more accurately complexes (specially those with higher affinities wherein conformational modifications can occur); however, the long computational times and the need for experimental restraints can hinder their efficient use for some systems [25]. Furthermore, for the type of complexes under study on this thesis, no significant gain would be achieved from using these algorithms.

I.5 Dealing with oxygen

Rubredoxin, desulforedoxin, cytochrome c_3 and superoxide reductase are involved in (though not necessarily limited to) cellular processes dealing with the presence of O_2 or one of its reactive species, in anaerobic organisms. In the *Desulfovibrio* genus, from which all the proteins used in this work were isolated (either directly or by overexpression of recombinant proteins in *E. coli*), rubredoxin and cytochrome c_3 take part in respiratory pathways that use

O_2 as the final electron acceptor, while SOR, desulforedoxin and rubredoxin have been implicated in the detoxification of the radical anion superoxide. In the next sections, the problem of oxygen exposure in anaerobes and the pernicious effects of reactive oxygen species will be explained in more detail, as well as, the fundamental characteristics of the proteins under study.

I.6 Reactive Oxygen Species

Oxygen is an essential molecule for the aerobic domain of life. After the advent of oxygenic photosynthesis some 2.5 x 10^9 years ago [28], the atmosphere rapidly started to show increased concentration of its reaction product, oxygen, thus leading to the development of aerobic organisms that utilize it as a final electron acceptor in respiratory chains. This, however, posed a problem to many anaerobic organisms that used methane, hydrogen or other small reduced molecules as electron acceptors, and were not prepared to deal with the consequences of intracellular oxygen (see next section). Oxygen, while essential for life, can have a lethal effect by promoting the production of ROS. Addition of electrons to anti-bonding orbitals in the triplet state to form the radical anion superoxide ($O_2^{\cdot-}$) or peroxide anion (O_2^{2-}) leads to weakening of the O-O bond. The anions generated by the reduction of oxygen can then react with a myriad of different targets *in vivo*.

For anaerobes, one option would be to only colonize or restraint their growth to safe environmental niches (sediments where oxygen cannot penetrate, for instance). One other complementary option would be to develop anti-oxidant defenses.

Although *Desulfovibrio* strains generally exhibit oxygen reduction rates comparable to those of aerobic bacteria (up to 670 nmol O_2 reduced per minute and per milligram of total protein), the microorganisms do not seem to survive after prolonged exposure to moderate oxygen concentrations, nor to repeated oxygen exposure [29].

I.7 ROS targeting of biological macromolecules

Here we focus on the effect of ROS in Prokaryotes, which constitute the scope of this thesis.

Superoxide can cause damage to cellular components either directly or indirectly by originating further ROS. Reaction of $O_2^{\cdot -}$ with iron-sulfur clusters can lead to iron release [30], with its subsequent participation in Fenton-like chemistry generating hydroxyl radicals. The reaction of hydrogen peroxide with reduced heme groups can also generate superoxide and heme degradation, with release of more Fe ions [31]. Condensation of superoxide with the $^{\cdot}NO$ radical generates peroxynitrite ($ONOO^-$), one of the main culprits in DNA damage. The lack of any intracellular lipid bilayers, which are chemically neutral and would thus constitute a barrier for the diffusion of charged ROS makes DNA damage especially prevalent and pernicious in prokaryotic organisms.

I.8 Coping with ROS - Iron and Iron Centers

Iron has long been considered an essential element for the preservation and proliferation of life forms, being present in metalloproteins throughout all domains of life. It is a proeminent co-factor in several proteins, and can be found in different coordination states and environments: either bound directly to aminoacid residues (cysteine, histidine side chains) or as a part of prosthetic groups (hemes, Iron-sulfur centers, among others) [32]. Over two-hundred different FeS center enzymes have been identified and characterized, participating mainly in electron transfer or redox catalysis processes, as well as oxygen sensors or gene regulators [33]. The most common geometry of Fe centers consists of a [4Fe-4S] cluster wherein each Fe atom is tetrahedrally coordinated to three inorganic sulfur atoms plus one sulfur from a cysteine side chain, commonly found in ferredoxins, reductases and hydrogenases, though several other types of Fe centers exist in nature ([2Fe-2S], [3Fe-4S], [8Fe-8S] and the FeMoCo moiety in nitrogenases, among others).

The simplest metal center containing Fe consists of the metallic atom coordinated to four sulfur atoms from cysteine side-chains [FeS_4], in a tetrahedral fashion, which could be distorted depending on the way the cysteine residues are distributed in the primary sequence of the protein (see below) [34, 35]. Rubredoxin and desulforedoxin, described in detail below, possess one FeS_4 center each (per monomer in the case of desulforedoxin). These centers, with potentials ranging from -600 mV to +400 mV [36], are capable of donating electrons to a variety of Electron Transfer (ET) partners, including (but not

restricted to) SORs [37], Rubrerythrin (Rbr) [38], Nigerythrin (Ngr) [39] and Rubredoxin:Oxygen Oxidoreductase (ROO), proteins that are involved in oxygen respiration or ROS detoxification pathways in the *Desulfovibrio* genus [40, 41]. It is worthy pointing out that all these proteins also contain at least one Fe center.

Since ROS are capable of releasing Fe into the intracellular pool with concomitant increase in Fenton and Haber-Weiss reactions that can lead to disruption of cellular processes and oxidative damage, it is of the utmost importance that prokaryotes possess mechanisms capable of handling these pernicious elements swiftly. In anaerobes, one such pathway consists of superoxide reductases (described above). Rbr and ROO are also capable of converting H_2O_2 and O_2 to water, respectively, without concomitant formation of oxygen unlike their aerobic counterparts, SOD and catalase.

I.9 The proteins studied in this work

I.9.1 Rubredoxin

Rubredoxin (Rd) from *Clostridium (C.) pasteurianum* was the first protein to be purified and have its FeS_4 center characterized, over four decades ago [42]. From then on, this protein has been isolated from several different species of bacteria and archaea, mostly anaerobic or microaerotolerant – sulfate-reducing bacteria from the *Desulfovibrio (D.)* genus, methanogens (*Methanocaldococcus (M.) jannaschii*), hyperthermophiles (*Pyrococcus (P.) furiosus, Archaeoglobus fulgidus, Thermotoga (T.) maritima*), human pathogens (syphilis spirochete *Treponema (Tr.) pallidum*, *Mycobacterium tuberculosis*), as well as some aerobes (mainly the *Pseudomonas (Ps.)* and *Acinetobacter* genera) [43-48]. More recently, rubredoxin was also found in the plastids of a cryptomonad alga, *Guillardia theta*, the first time a rubredoxin-like protein was characterized from an eukaryotic organism [49].

The common feature of these rubredoxins lies in its metal coordination motif: two CX_2CG segments, separated by a variable number of aminoacid residues (Fig. 1.2 A). The number of residues in the primary structure of rubredoxins seldom exceeds 54 residues, with *D. desulfuricans* rubredoxin being the smallest with only 45 residues [50]. On the other hand, *Ps. oleovorans* rubredoxins 1 and 2 are constituted by 132 and 173 residues, respectively.

Recently, a second type of rubredoxins has been described in some species of *Desulfovibrio*, where the N-terminal metal-binding motif consists of a CX_4C segment [51].

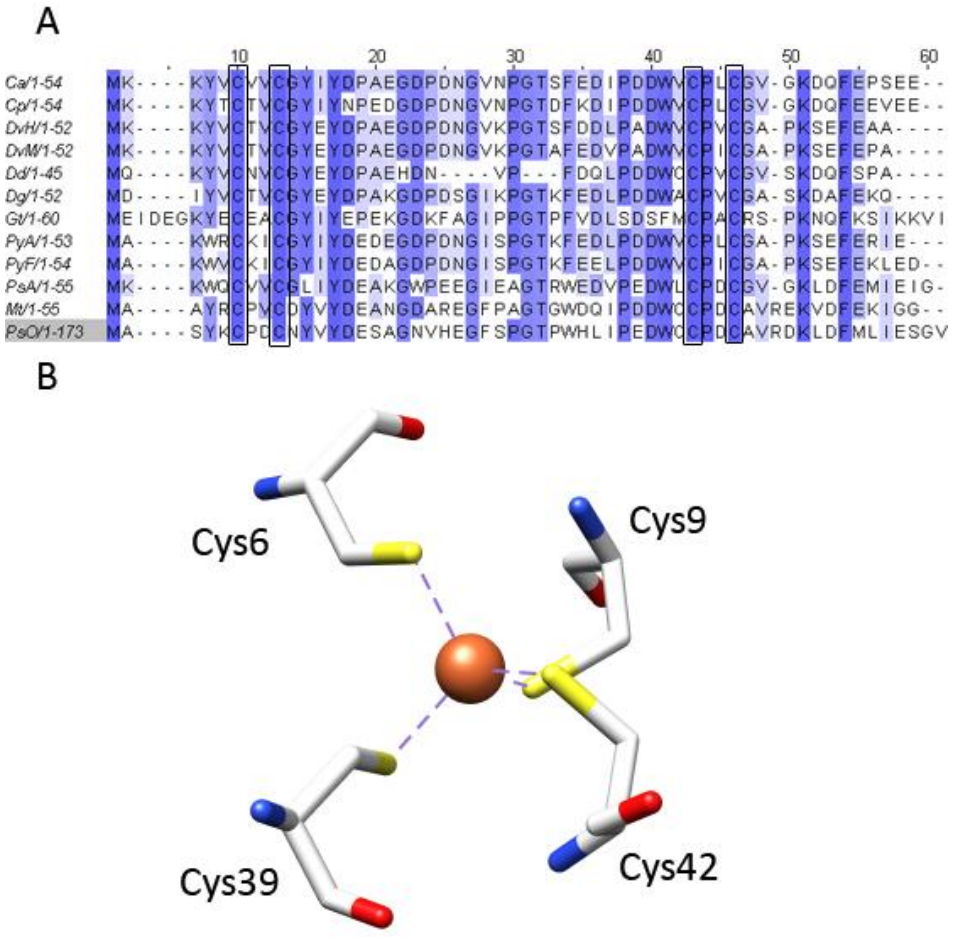

Fig. I.2 – A) Primary sequence alignment of the 12 available rubredoxin structures in the Protein Data Bank (www.rscb.org/pdb) in July 2010. Sequence alignment was performed using ClustalW. Conserved cysteine residues are highlighted by binding boxes. *Ca* = *Chlostridium acetobutylicum*. *Cp* = *Chlostridium pasteurianum*. *DvH* = *Desulfoviibrio vulgaris* strain Hildenborough. *DvM* = *Desulfovibrio vulgaris* strain Miyazaki F. *Dd* = *Desulfovibrio desulfuricans* ATCC 27774. *Dg* = *Desulfovibrio gigas*. *Gt* = *Guillardia theta*. *PyA* = *Pyrococcus abyssi*. *PyF* = *Pyrococcus furiosus*. *PsA* = *Pseudomononas aeruginosa*. *Mt* = *Mycobacterium tuberculosum*. *PsO* = *Pseudomonas oleovorans* rubredoxin type-2. B) FeS_4 center from *D. gigas* rubredoxin, displaying its characteristic tetrahedral geometry. Image created with UCSF Chimera [52].

The structure of the metal center is remarkably well conserved geometrically on all proteins available in the Protein Data Bank (PDB - www.pdb.org), and Fig. I.2 B depicts the *D. gigas* rubredoxin FeS_4 center.

Although it was established early on that rubredoxin could serve as an electron-carrier, its specific function only started to be ascribed decades later, when it was found that the protein from *Ps. oleovorans* was an electron carrier for the alkane oxidation pathway, receiving electrons from a reductase containing a flavin group and donating them to a membrane-bound alkane hydroxylase [53]. Other rubredoxins function in a similar manner in oxygen-scavenging pathways, donating the electrons to SORs (*Desulfovibrio* genus, *P. furiosus, C. pasteurianum*), hydrogen peroxide-reductant protein rubrerythrin [38], or to terminal reductases, such as ROO that allow the organisms to actually produce ATP from oxygen reduction (in *D. gigas*) [41, 45].

Its iron center has a number of characteristic properties (Fig. I.2 B): in the oxidized state it has a high-spin S = 5/2, which leads to the characteristic UV-visible absorption bands (two major absorption bands at ~380 nm and 490 nm, and a broad band at 570 nm in the oxidized state) and EPR signals which are characterized by strong rhombicity (E/D ~0.3) and *g* values of 4.3 and 9.4. Moreover, the presence of five unpaired electrons in its *d* shells leads to strong paramagnetic relaxation enhancements and pseudo-contact shifts that, while hampering the detection of resonances near the metal center in standard NMR pulse sequences, can also become an advantage in other cases, as it will be explained in chapter II.

1.9.2 Desulforedoxin

Desulforedoxin (Dx) shares some characteristics with rubredoxin: it is a small (2 x 3.7 kDa), homodimeric, non-heme iron protein, containing a FeS_4 center that differs from the one of rubredoxin in terms of the Fe coordinating sequence. In the case of desulforedoxin, there are two C-terminal cysteine residues in adjacent positions, that impose small distortions in the tetrahedral geometry of its metal center and give rise to slightly-altered UV-visible absorption bands (slight shifted absorption maxima), EPR and Mössbauer spectra [35, 54]. The distorted tetrahedral geometry of desulforedoxin from *D. gigas* and center I of SORs has

been attributed to the fact that the C-terminal metal-binding cysteines are adjacent to one another – structural studies involving mutants of desulforedoxin in which aminoacids have been inserted between the adjacent cysteines show that the geometry of the center becomes similar to the one of rubredoxin [55] This protein has only been isolated and characterized from *Desulfovibrio gigas* so far, with putative genes for desulforedoxin-type genes found in *Methanosarcina acetivorans* and *Dehalococcoides ethanogenes*. It is postulated that it may serve as an electron transfer partner to superoxide reductase in *Desulfovibrio gigas* (see below) [36].

1.9.3 Superoxide Reductase

Despite some evidence that, in certain conditions, members of the *Desulfovibrio* genus actually have the ability to utilize O_2 as an electron acceptor in periplasmic respiratory pathways, these organisms cannot withstand exposure to aerobic environments for prolonged periods of time without compromising its viability [56-58]. In order to deal with the negative aspects of ROS, oxygen-intolerant organisms present systems that can minimize the deleterious effects of ROS (among others, lipid oxidation, protein cleavage, DNA damage). One system present in several microorganisms (from anaerobes to microaerophilic bacteria) consists of superoxide reductase (SOR). SOR, which catalyzes the reduction of the superoxide anion ($O_2^{\cdot -}$) to H_2O_2 presents a clear advantage relative to Superoxide Dismutases (SOD) for these organisms (see below).

SODs and catalases are ubiquituous enzymes present in both eukaryotes and prokaryotes and are responsible for the elimination of ROS. Since radical anion superoxide is readily formed by attachment of a single electron to O_2 (and excess electrons can easily build up in solution from cellular redox processes), and can react particularly well with the S atoms of cysteines, methionines and iron-sulfur clusters. SOD can rapidly catalyze the dismutation of this radical species to both O_2 and H_2O_2 (eq. 1), and the later can be dealt by catalase [59].

$M^{(n+1)+} + O_2^{\cdot -} \rightarrow M^{n+} + O_2$

$M^{n+} + O_2^{\cdot -} (+ 2H^+) \rightarrow M^{(n+1)+} + H_2O_2$

Overall: $2O_2^{\cdot -} + 2H^+ \rightarrow O_2 + H_2O_2$ (eq.1)

All four types of SOD can catalyze this reaction, regardless of the metal center they possess: copper (Cu,ZnSOD), manganese, iron or nickel. The Fe-only enzyme is mostly found in less developed organisms; the Mn-containing SOD is usually found in plants (chloroplasts) and mitochondria; Cu,Zn SOD is found ubiquitously in the intra- and extra-cellular space of eukaryotic organisms; while the Ni-SOD form is commonly found in proteobacteria [60]. In anaerobic bacteria, though some evidence of SOD and catalase activity has been found [61, 62], the generation of O_2 as an end product meant that an alternative strategy for superoxide detoxification would be preferred. SOR is one such alternative.

SOR (EC 1.15.1.2) was first discovered in crude extracts of *D. desulfuricans* ATCC 27774, and *D. vulgaris* Hildenborough two decades ago [63]. The protein in these organisms belongs to the class I SORs, as they contain one Fe atom coordinated to four equatorial histidine residues sidechains, and one axial cysteine sulfur (the so-called center II, the catalytic center, wherein superoxide reduction occurs, Fig. I.3), as well as a second Fe atom bound by four cysteines, with a binding pattern and geometry similar to the one of *D. gigas* Dx (center I, or ET center, Fig. I.3 A). This class of proteins was thus originally named Desulfoferredoxin (Dfx) due to the unusual combination of Fe centers that are present in two different domains. Class II SORs (such as the ones from *D. gigas* and *P. furiosus*), first discovered when a blue-colored protein was isolated from *D. gigas* cellular extracts [64], do not possess the N-terminal desulforedoxin-like domain that bind the Fe atom in center I, thus containing only center II. They are commonly named Neelaredoxins (Neela means “blue” in Sanskrit) due to the spectroscopic features of the only Fe center present – a very broad absorbance band with maximum near 665 nm, responsible for its characteristic blue color [64]. Recently a third type of SORs has been isolated and characterized: the protein from *T. pallidum* (also commonly called neelaredoxin due to its blue color in the oxidized form) has a similar fold/3D structure and aminoacid composition to the class I SORs [65] – however, the lack of crucial Cys residues of the center I binding motif does not allow for a Fe atom to be coordinated – thus its spectroscopic properties are similar to the ones of class II SORs (Fig. I.3).

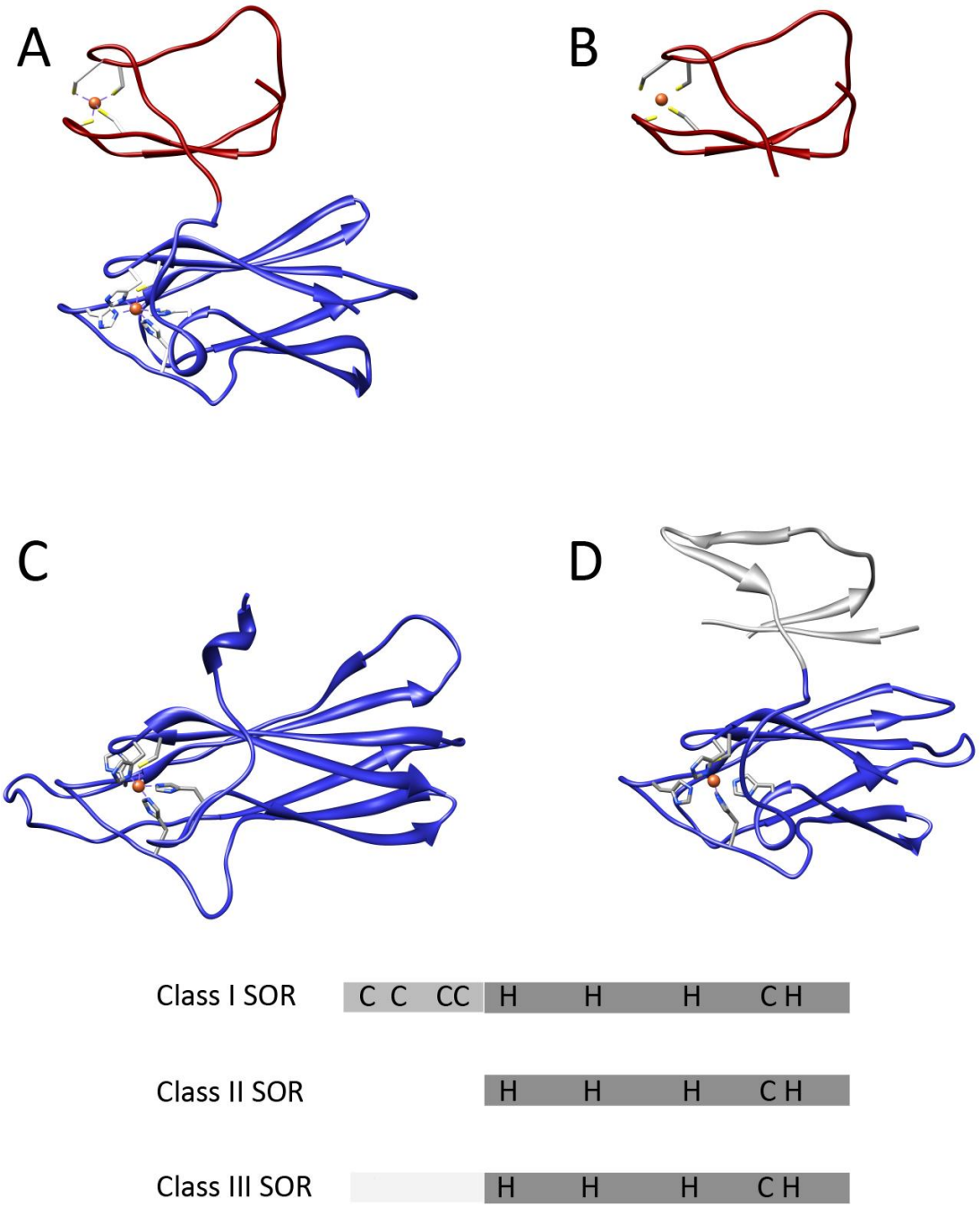

Figure I.3 – A) *D. desulfuricans* ATCC 27774 Class I SOR monomer (from PDB file 1DFX). The Dx-like domain with ET center is depicted in dark red, while the catalytic domain is colored blue. B) Desulforedoxin monomer from *D. gigas* (from PDB file 1DXG). C) *Pyrococcus furiosus* Class II SOR monomer (from PDB file 1DQI). Notice the absence of the Dx-like domain. D) *Treponema pallidum* Class III SOR (from PDB file 1Y07). The N-terminal domain (colored gray), although similar in geometry to Class I SORs, does not possess the necessary cysteine residues in order to coordinate a Fe ion.

Although isolated in the early 90's, the function of these proteins was only established almost a decade later when the protein from *Desulfoarculus baarsii* was shown to be able to suppress ROS-related damage in *E. coli* cells with SOD genes knocked out [66]. Subsequently, *D. vulgaris* Hildenborough mutants lacking the *rbo* gene, which encodes SOR, were found to be 100-fold more sensitive to oxygen.

The definitive proof, however, was described in 1999 when Adams and co-workers successfully demonstrated the reductase activity of the tetrameric *P. furiosus* SOR [13], in an elegant assay that also demonstrated the lack of dismutase activity of this class of proteins. Furthermore, it was postulated that in this organism rubredoxin and NROR (NAD(P)H:rubredoxin oxidoreductase) would also be part of the superoxide-detoxifying system. It is also important to mention that SOR, rubredoxin and ROO are usually encoded by the same operon, linking the expression of these proteins as a complete response unit towards ROS detoxification [67]. In *D. gigas*, however, the operon that encodes for SOR includes two other genes coding for chemotaxis-like proteins. Since *D. gigas* can use O_2 in respiratory processes, this operon seems to serve as a sensor for the presence of oxygen in the cell [68, 69].

All three classes of SOR possess a Fe center coordinated to four histidines in the axial plane and one cysteine sulfur in the axial plane (Fig. I.4)

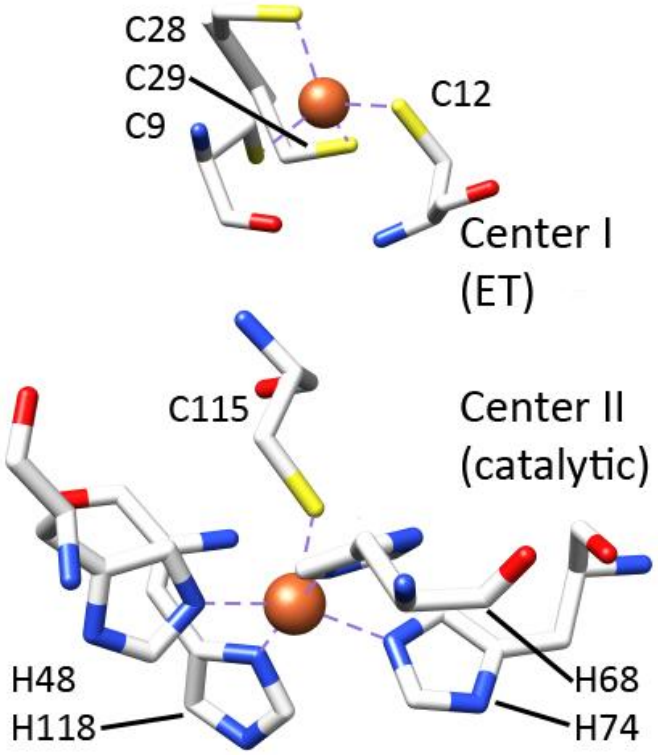

Figure I.4 – Schematic representation of the two centers of a class I SOR from *D. desulfuricans* ATCC 27774 (PDB: 1DFX). Above: desulforedoxin-like center (center I). Below: center II of SOR. Blue: Nitrogen atoms. Yellow: Sulphur atoms. Red: Oxygen atoms. White: Carbon atoms. Orange: Iron atoms.

The mechanism of superoxide reduction

In the oxidized state, the Fe atom is coordinated in the equatorial plane by four nitrogen atoms from histidinyl side chains, and one cysteine sulfur in the axial position, resulting in a square pyramidal geometry. An additional ligand, either a conserved glutamate carboxylate side chain or a hydroxide anion has been observed to bind in the sixth (axial) position and it has been proposed to serve as a gateway by loop readjustment, and also as a proton donor in intermediate steps of superoxide reduction (reviewed in detail in ref. [70]), although its role is still controversial and far from being established [71]. The currently accepted mechanism is shown in Fig. I.5.

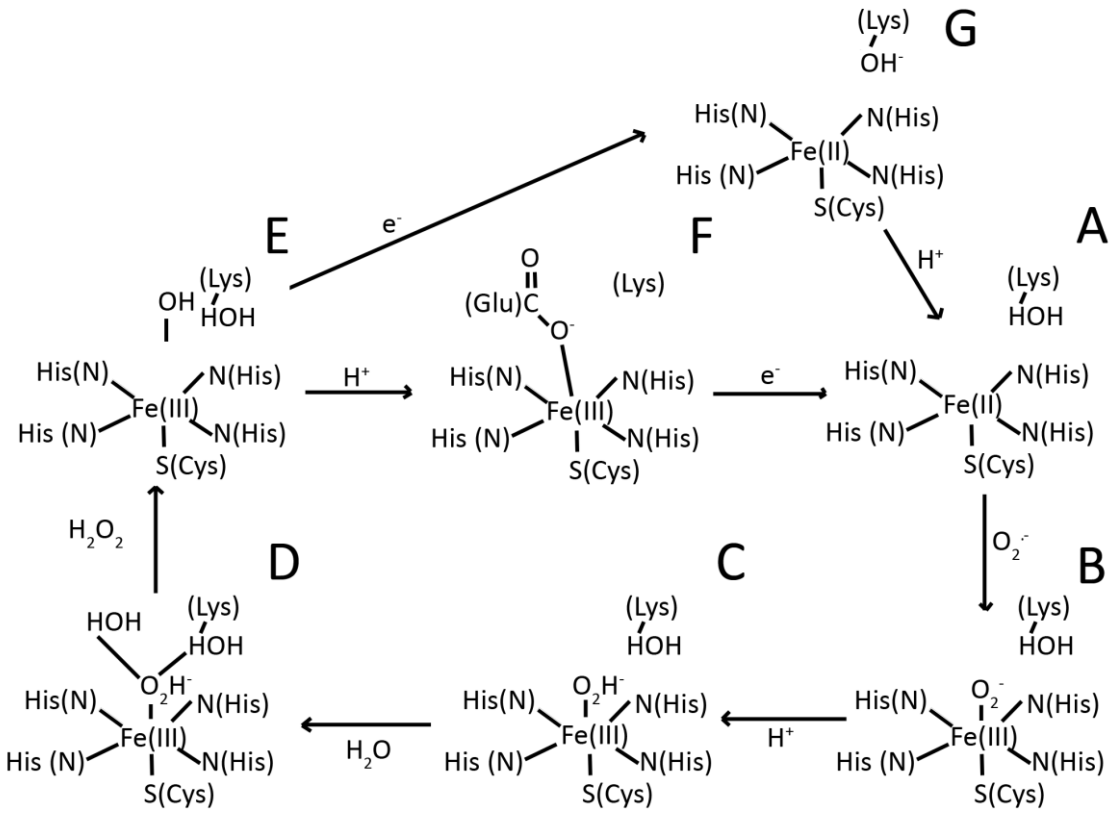

Figure I.5 – A) Resting, reduced state. B) Coordination of radical anion superoxide leads to Fe oxidation. C, D and E) Upon protonation of superoxide (with the protons coming from either the surrounding environment or a nearby lysine residue) and complexation with two other water molecules that can come, an hydroxide ion remains bound to the ferric ion. F) Another protonation step leads to the release of a water molecule. A nearby conserved glutamate residue (when available) will then coordinate Fe(III) in the remaining axial position. Reduction of the catalytic center by one of the redox partners of SOR brings the protein back to its ready state. G) Regeneration may also occur by direct reduction of the Fe ion, with the hydroxide ion being captured by the sidechain amine of the aforementioned lysine residue. Protonation of this hydroxide ion will bring the center again to the ready state.

The overall reaction catalyzed by SOR is then:

$O_2^{\cdot -} + 2H^+ \rightarrow H_2O_2$ (eq. 2)

In order to reduce the oxidized Fe center for the next reaction cycle, SOR must receive electrons from a physiological electron donor protein, which has been proposed to be rubredoxin or desulforedoxin (see above) [13, 36, 47]. However, in Class I SORs, the

presence of a Dx-like electron-transfer center could lead to a faster regeneration rate, though no concrete evidence has been established yet [63, 72, 73]. Class I SOR remain fully functional *in vitro* even when the residues that coordinate the Fe in center I have been mutated [74].

This work focused on the study of class II SOR from *D. gigas* [64]. Other enzymes from the class II SOR family have been isolated from the thermophiles *Pyrococcus furiosus and Pyrococcus horikoshii* (PDB: 1DQI and 2HVB) [13, 75] *Archeoglobus fulgidus* [76], and *Thermotoga maritima* (PDB: 2AMU) [77].

I.9.4 Cytochrome c_3

Cytochrome c_3 is a periplasmic, soluble protein (M ≈15 kDa), usually found in large amounts in the *Desulfovibrionaceae* family (up to 30% of the total amount of proteins in the periplasm), and is characterized by the presence of four *c*-type heme groups, axially coordinated by the imidazole rings of two histidine sidechains [78, 79], which present a remarkable conservation of heme core architecture in terms of heme-heme distances and angles of their substituents (Fig. 1.6 and 1.7).

Cytochrome c_3 was first isolated from *D. vulgaris*, over half a century ago [80], and has since been isolated from a number of sulfate-reducing bacteria [79]. This protein belongs to the cytochrome *c* family, a group of *c*-type heme binding proteins that possess a number of spectral characteristics. Owing to the bis-histidine axial coordination, the heme iron are in the low-spin configuration and thus are diamagnetic (S = 0) when reduced and low spin paramagnetic (S = 1/2) when oxidized. The UV–visible spectra of cytochromes c_3 are typical for this coordination mode and spin states with a strong Soret band centered close to 410nm in the oxidized form and 419nm in the reduced form. In the reduced form, two sharp α and β bands are found in the vicinity of 552 and 525 nm, respectively. This makes the protein not only easy to detect and purify from cellular extracts, but also easy to be used in spectroscopic techniques, such as steady-state kinetics or stopped-flow assays.

This cytochrome has also a number of specific characteristics in its NMR spectra. In the oxidized state, the presence of a paramagnetic iron leads to contact and pseudocontact

shifts on the heme methyls resonances, shifting several of these signals to very high frequency, up to 32-33 ppm at 298 K. The spectral discrimination provided by the resonances of the heme substituents was applied to the determination of interaction surfaces by NMR and the microscopic reduction potentials of the hemes, allowing the identification of cooperativities in the binding of hemes and protons by these cytochromes [81]. In the reduced state, the lack of paramagnetic effects leads to the disappearance of these resonances.

Cytochromes c_3 are thought to be involved in several reactions, ranging from electron transfer in anaerobic and aerobic respiration to peroxide scavenging [82]. The cytochrome c_3 from *D. gigas,* that was used in this work, is proposed to be an electron/proton carrier from periplasmic hydrogenase to several membrane proteins, such as high molecular weight cytochromes (9-heme Hmc in *D. desulfuricans* ATCC 27774, 16-heme cytochrome in *D. vulgaris*) and Type II cytochrome c_3 in *D. africanus* and *D. vulgaris*, as part of the respiratory electron transfer chain that enables ATP production or/and sulfate reduction that occurs in the cytoplasm of these organisms [83-86]. Cytochrome c_3 has also been implicated in the aerobic respiration of members of the *Desulfovibrio* genus when transiently exposed to aerobic environments (Fig. I.7) [87].

In all cases, only one heme is implicated in the ET reactions: heme IV, possibly due to the positively charged lysine patch in its vicinity, as well as the hydrophobicity conferred by exposure of heme methyl groups instead of propionates (discussed in more detail on subsequent chapters). This cytochrome has also been proposed to act as a sulfur reductase [88].

Cytochromes c_3 have some conserved residues: heme iron-coordinating histidines and heme-binding cysteines (two per heme group), usually in the motif CX_nCH (n = 2 or 4), as well as the hydrophilic, positively-charged patch around heme IV, proposed to be a specific recognition site for hydrogenase [86].

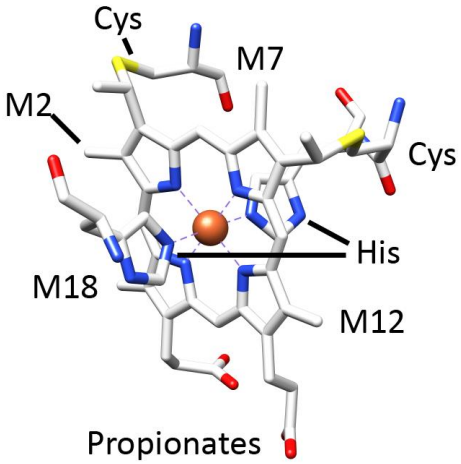

Figure I.6 – Schematic representation of a type *c* heme. Methyl groups, which will be analyzed in further detail in coming sections, are identified and numbered according to the IUPAC recommendations [89].

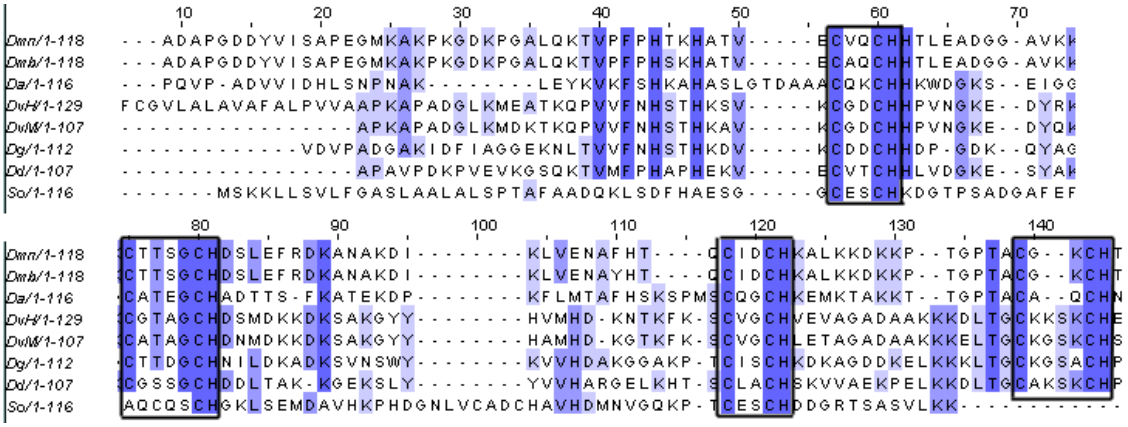

Figure I.7 – Primary sequence alignment of selected cytochrome c_3 which structure is available in the PDB. *Dsm* = *Desulfomicrobium norvegicum*. *Dmb* = *Desulfomicrobium baculatus*. *Da* = *D. africanus*. *Dv*H = *D. vulgaris* Hildenborough. *Dv*M = *D. vulgaris* Miyazaki F. *Dg* = *D. gigas. Dd* = *D. desulfuricans* ATCC 27774. *So* = Shewanella oneidensis. Black binding boxes identify the heme-binding conserved sequences CX_nCH (n = 2 or 4). Alignment performed with Clustal W.

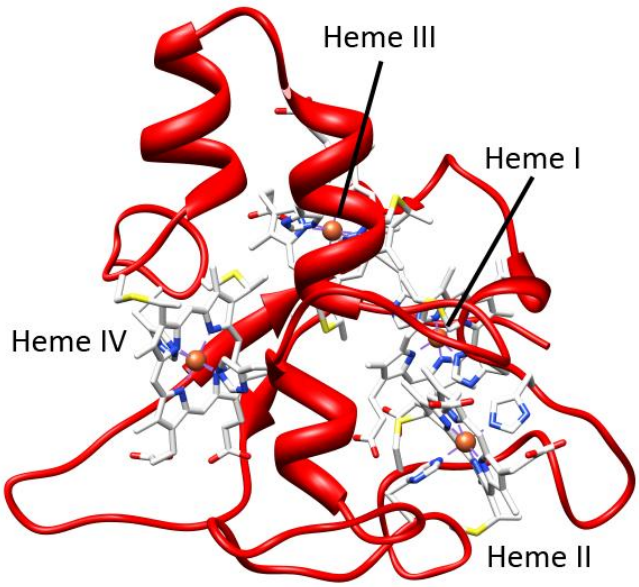

Figure I.8 –Cytochrome c_3 from *Desulfovibrio gigas* (PDB: 1WAD). Notice the exposed methyl groups of heme IV, while other heme groups usually have the propionate chains exposed.

The coordination of the Fe atom of the heme groups is completed by four nitrogen atoms from the porphyrin ring. The heme groups in this cytochrome usually have low redox potentials (-400 mV to -120 mV). The redox-Bohr effect [90] allows the cytochrome molecule to become reduced, at the metal center, and at the same time protonated at certain protonable residue, thus providing the electrons for the cytoplasmic respiratory chain, as well as the protons necessary for the energy-producing gradient of ATP synthase.

Since this protein contains four *c*-type hemes in different chemical environments (heme IV is surrounded by a positively charged lysine patch, thought to interact with a strongly negative patch of hydrogenase surface, while other hemes are surrounded by more neutral environments) and surface orientations (heme III has its charged propionate groups exposed to solvent, while heme IV has apolar methyl groups most exposed) make this protein a prime candidate to serve as a multi-purpose probe for interaction studies involving heme proteins. This characteristic will be discussed in more detail in subsequent chapters (chapter II and III).

I.10 Objectives

The aim of this work was the characterization of transient complexes using different NMR methodologies. *D. gigas* rubredoxin, due to its small size, can be used as a model for the interaction of iron-sulfur cluster proteins with other partners, as well as a model for proteins with a pronounced negatively charged electrostatic landscape. In this work, the interaction with cytochrome c_3, a tetraheme protein with different electrostatic environments around each heme, was chosen to establish its potential role as a paramagnetic relaxation inducing probe, which was studied by ^{1}H NMR, 2D NMR and *in silico* docking (chapter II).

In this work the feasibility of two Gd-containing cyclen-derived probes (DOTAM and DOTP) as paramagnetic relaxation enhancement (PRE) probes, that bind non-covalently at the surface of proteins, to predict protein-protein interactions was also assessed (chapter III).

Finally, the knowledge obtained in characterizing transient complexes was put to use in the characterization of the physiological complex between *D. gigas* rubredoxin and SOR, by 2D NMR, steady-state kinetics and *in silico* docking. A model structure for this physiological complex was attained. Furthermore, one other putative electron donor to this enzyme, desulforedoxin, was also characterized using the same methodologies. Competition assays between rubredoxin and desulforedoxin were also performed to establish whether these two ET proteins competed for the same binding-site, at the enzyme surface, to donate electrons to the SOR catalytic center.

CHAPTER II – RUBREDOXIN AS A PARAMAGNETIC RELAXATION-INDUCING PROBE

Case Study with a multi-heme protein (cytochrome c_3) using NMR spectroscopy.

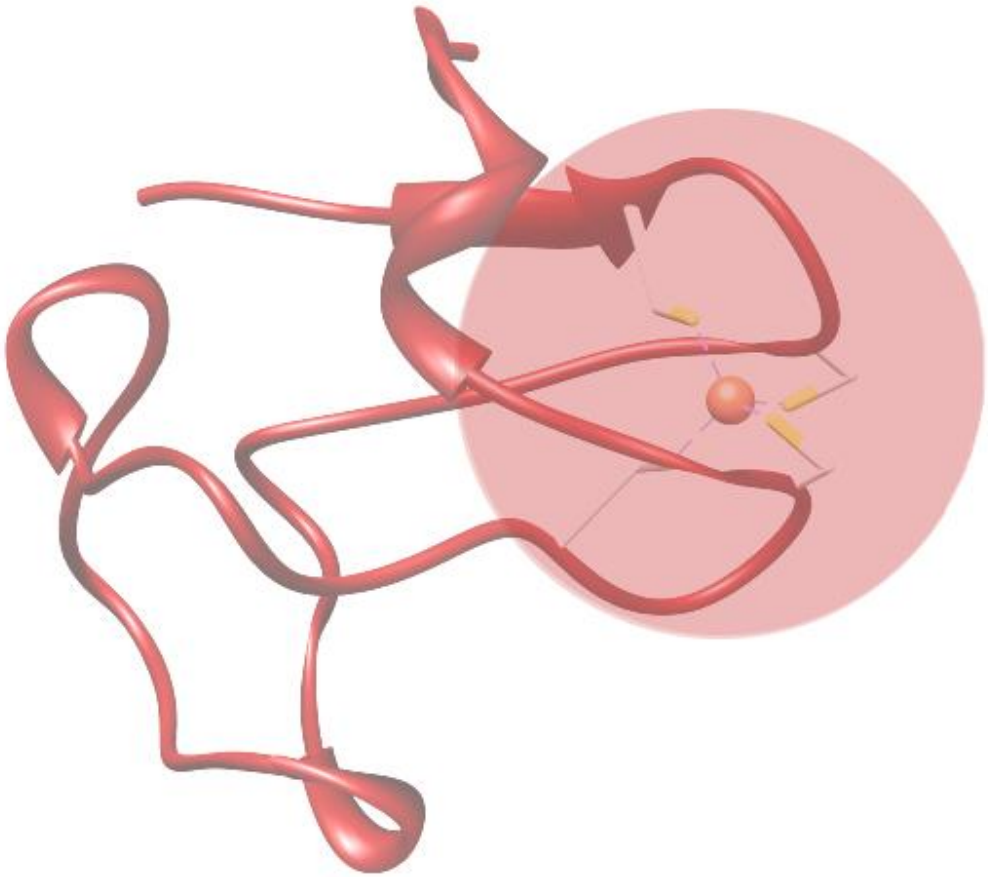

This work was published in Almeida *et al.* (2009) *Journal of Inorganic Biochemistry* **103(9)**:1245-53.

Chapter II Index

II.1 Abstract

In this chapter, the paramagnetic effect due to the presence of a metal center with unpaired electrons was used to map the interface of an electron transfer complex. *Desulfovibrio gigas* cytochrome c_3 was chosen as target to study the effect of the paramagnetic probe, Fe-rubredoxin, which produced specific line broadening in the heme IV methyl resonances M2 and M18. The rubredoxin binding surface in the complex with cytochrome c_3 was identified in a heteronuclear 2D NMR titration. The identified heme methyls on cytochrome c_3 are involved in the binding interface of the complex, a result that is in agreement with the predicted complexes obtained by restrained molecular docking, which shows a cluster of possible solutions near heme IV. The use of a paramagnetic probe in ^{1}HNMR titration and the mapping of the complex interface, in combination with a molecular simulation algorithm proved to be a valuable strategy to study electron transfer complexes involving non-heme iron proteins and cytochromes.

II.2 Introduction

As mentioned in Chapter I, rubredoxin is a small electron-transfer protein, containing a Fe atom coordinated to the sulfur atoms of four cysteinyl residues' sidechains. Due to the high-spin configuration of this tetrahedral-geometry center, the Fe-S center in its oxidized state has S = 5/2, which can give rise to different paramagnetic effects on the NMR spectrum. One of those effects is the Zero-Field Splitting (ZFS), which causes the splitting of a resonance into 2S+1 peaks, with the decrease of intensity in each individual peak. Moreover, due to increased relaxation pathways generated by the stochastic magnetic fields generated by unpaired electrons, nuclei in the vicinity of this center (up to a distance of ~5 Å) may have their resonances broadened up to the point of no detection [1-3].

While for some time, paramagnetic effects have been a hindrance in acquiring and providing a complete outlook of NMR spectra of paramagnetic species, recent developments in the technology and pulse sequences make it now possible to assign resonances that are near the paramagnetic center, thus allowing for more precise estimation of structural features or mechanistic effects.

In addition, the paramagnetic effects are being increasing used to gather paramagnetic restraints, such as pseudocontact shifts andcross-correlation effects. dynamics. Residual Dipolar Couplings, which can also arise from the alignment of paramagnetic species in solution when an external magnetic field is applied, have also been increasingly used for structure determination and characterization of protein dynamics

Concomitantly, techniques such as direct ^{13}C detection, perdeuteration and TROSY-type pulse sequences take advantage of the lower sensitivity of the ^{13}C isotope to paramagnetic effects (as they depend on the square of the gyromagnetic ratio), limited relaxation pathways and the detection of only the slow-relaxing components of scalar-coupled nuclei, thus increasing sensitivity [2, 4, 5].

Furthermore, protein-protein complexes have also been characterized using paramagnetism-derived information [6-9].

In this chapter it is described the use for the paramagnetic relaxation enhancement potentialities of *D. gigas* rubredoxin, in ^{1}H and 2D NMR experiments, to characterize

the complex formed with *D. gigas* cytochrome c_3. This cytochrome contains four *c*-type hemes linked to the polypeptide chain through tioether bonds to cysteine residues that are in the CXXCH or CXXXXCH motif, and the surface near each of those hemes presents different electrostatic properties.

Cytochrome c_3 heme methyl resonances appear between 10 and 35 ppm of the ^{1}H NMR spectrum (Fig. II.1), the so-called paramagnetic region, due to the interaction with the low-spin heme iron (S = ½) [10, 11]. These resonances are usually well resolved, facilitating the analysis of the effects caused by the binding of another protein, which in this case study is rubredoxin. In the case of *D. gigas* cytochrome c_3 it is possible to observe 11 of the expected 16 methyl resonances belonging to the 4 heme groups, which were previously assigned [12].

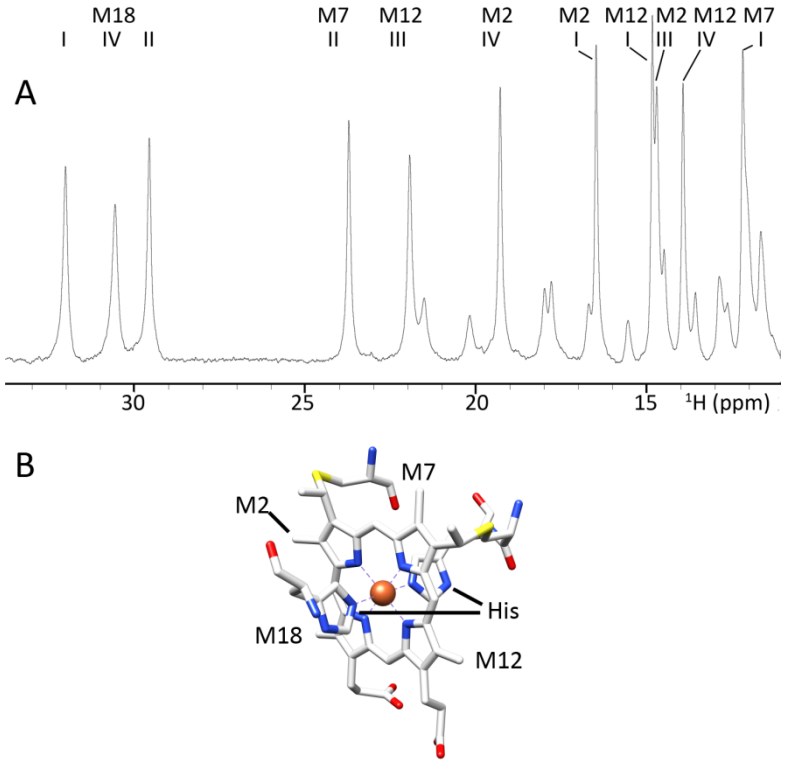

Figure II.1 – A) ^{1}H NMR spectrum of *D. gigas* cytochrome c_3 between 34 and 11 ppm. All resonances belong to heme methyl groups and propionate protons. The spectrum was obtained in 10mM Tris-HCl in 100% D_2O, pH 8.0 (uncorrected for isotope effect) in a 400 MHz spectrometer. Heme methyls are labeled according to the IUPAC nomenclature. B) Scheme of a type *c* heme, with heme groups lined out.

Therefore, the assigned heme methyl resonances can be used to determine which heme will be closer to the partner upon complex formation via chemical shift variations and/or half-height line width broadening brought upon by paramagnetic effects. These experiments will also allow the determination of the complex stoichiometry and binding affinity.

On the other hand, rubredoxin, with its high spin Fe center, with a S=5/2, does not present any well-resolved resonance in the paramagnetic region of a ^{1}H-NMR spectrum. This is due to very fast relaxation of nuclei resonances deriving from the very strong electron momenta, which cause strong linewidth broadenings, masking other additional paramagnetic effects. In a 2D NMR spectrum, such as HSQC, the resonances of residues near the metal center (up to 5-6 Å distance) become broadened beyond detection due to this effect (Fig. II.2). The metal center, however, can be easily replaced by another metal ion (such as, diamagnetic Zn^{2+}, see below and chapter IV for an illustration of this), which will enable not only the detection of amide resonances near the metal, but also chemical shift mapping via 2D NMR titration of the residues affected in a titration, even if these residues are near the metal center.

Although rubredoxin and cytochrome c_3 are not physiological electron transfer partners due to their localization in different compartments of the cell (cytoplasm and periplasm, respectively), the methodology and the information obtained in this study can be applied to other complexes that also involve the interaction between a cytochrome and an iron-sulfur protein, such as in the case of the interaction between putidaredoxin and cytochrome P450 from *Pseudomonas putida* [13], or the interaction between tetrahemic cytochromes and high potential iron sulphur proteins in the photosynthetic reaction centre complex of purple bacteria [14, 15].

Molecular docking algorithms such as BiGGER [17, 18], described in detail in chapter I, in conjunction with the NMR data will help predict a model structure for this complex. A diamagnetic version of rubredoxin, in which the Fe atom was substituted with Zn, was used in the NMR titrations in order to analyze the paramagnetic effects and to determine the residues involved in the binding surface with cytochrome c_3, by 2D NMR experiments.

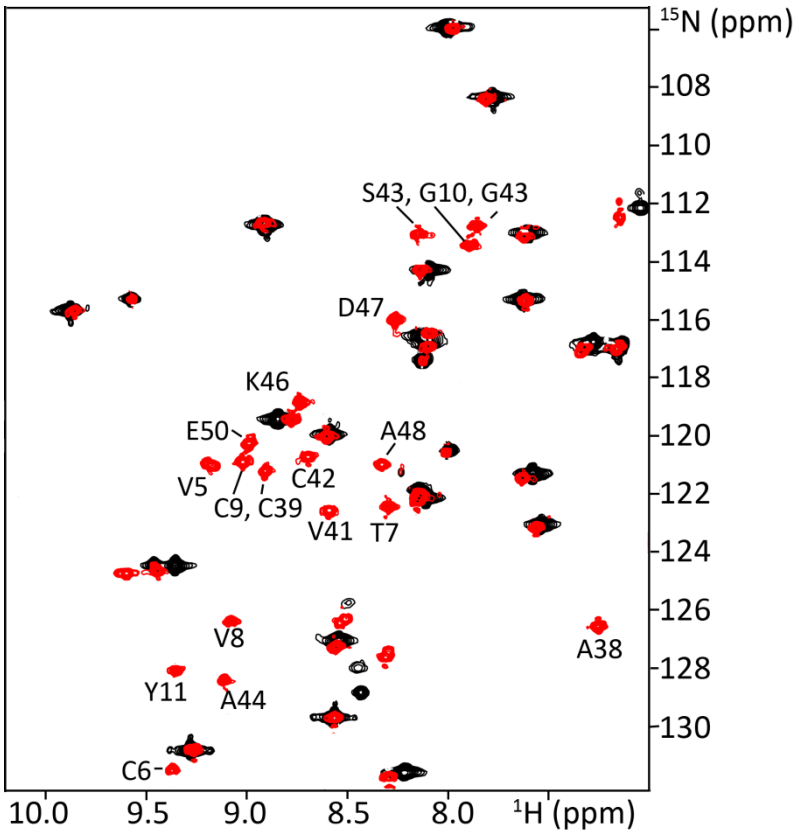

Figure II.2 – Comparison between the ^{1}H -^{15}N HSQC spectra of Fe-rubredoxin (black resonances) and Zn-substituted rubredoxin (Red resonances). The resonances broadened beyond detection, which belong to residues that coordinate or are near the metal center, are identified in the figure. The highlighted area (7.0 – 10.2 ppm in the proton frequency, 105-132 ppm in the ^{15}N frequency) contains 30 resonances of the expected total of 48 (52 residues, minus the first methionine and five proline residues, plus two from Q52's sidechain) [16]. Spectra were acquired at 298K with the proteins dissolved in Tris-HCl 20 mM pH 7.6 buffer.

II.3 Materials and Methods

Unless otherwise stated, all reagents were of analytical grade or higher and purchased from Sigma–Aldrich, Fluka or Riedel-de-Häen. The purification procedures were performed at pH 7.6 (room temperature) and at 4 ºC using an ÄktaPrime Plus HPLC apparatus, except in the first step of cytochrome c_3 purification.

II.3.1 Purification of *D. gigas* cytochrome c_3

D. gigas cytochrome c_3 was purified from the soluble fraction of homogenized *D. gigas* cell extract, which was loaded onto a DEAE-52 anionic exchange resin (Whatman), equilibrated with 10 mM Tris–HCl. The proteins were eluted using a linear ionic strength gradient (0–500 mM NaCl). The fractions containing cytochrome c_3 were combined, and loaded onto a hydroxyapatite column (BioRad) equilibrated with 10 mM Tris–HCl, and eluted with a linear gradient of 500–0 mM NaCl in 10 mM Tris–HCl. The fractions containing cytochrome c_3 were pooled and concentrated using a Diaflo apparatus over an YM10 membrane (Millipore) and loaded onto a Superdex 75 (GE Biosciences) column, equilibrated with 300 mM Tris–HCl. The purity ratio ($[A_{553,\ reduced} - A_{570,\ reduced}]/A_{280,\ oxidized}$) at the end of the purification was 2.8 [36], and the purity was also confirmed by SDS–PAGE.

II.3.2 Purification of *D. gigas* rubredoxin

II.3.2.1 Strains, vectors, and growth conditions

E. coli BL21(DE3) cells (Novagen) containing the pSPRb plasmid coding for *D. gigas* rubredoxin [19] were used for expression of the protein and grown aerobically at 37 ºC in M9 minimum medium [20] (1.0 g/L NH_4Cl, 3.0 g/L KH_2PO_4, 6.0 g/L $Na_2HPO_4.7H_2O$, 0.5 g/L NaCl, 0.4% (w/v) glucose, 1 mM $MgSO_4$, 0.1 mM CaCl.2H2O) supplemented with 100 μg/mL ampicillin, 100 μM FeCl3 and vitamins (5 mg thiamine–HCl, 1 mg biotin, 1 mg choline, 1 mg folic acid, 1 mg nicotinic acid, 1 mg panthotenic acid, 1 mg pyridoxal and 0.1 mg riboflavine per liter), for 10–12 h, after induction with 1 mM isopropyl-β-D-thio-galactopyranoside (IPTG), at an OD_{600nm} of 0.8. During induction, to

avoid foaming, the growth was shaken at a lower speed. In order to obtain the ^{15}N-labelled or unlabelled Zn-containing rubredoxin that were used, the same clone was grown in the same minimum medium, but 100 μM $ZnCl_2$ was added instead of $FeCl_3$.

II.3.2.2 Purification of rubredoxin

Cells containing heterologously expressed Fe-rubredoxin or Zn-rubredoxin were harvested by centrifugation at 4100*g* and resuspended in 10 mM Tris–HCl buffer at a 1 g/mL wet cell ratio. The cells were disrupted at 15000 psi using an Emulsiflex-C5 cell homogenizer (Avestin), and then ultracentrifuged at 138,000*g* for 90 min. The supernatant was then filtered and injected onto a DEAE-Sepharose Fast Flow anionic exchange resin (GE Biosciences), equilibrated with 10 mM Tris–HCl. A linear gradient (0–500 mM NaCl) was applied and the rubredoxin-containing fractions were concentrated in a Diaflo apparatus over an YM3 membrane (Millipore). This fraction was loaded onto a Superdex 75 column (GE Biosciences), equilibrated with 300 mM Tris–HCl buffer, and fractions containing pure rubredoxin were combined. Throughout the purification the purity of the rubredoxin fractions were assessed by SDS–PAGE and, in the case of Fe-rubredoxin, by measuring the A_{280}/A_{493} ratio. The pure Fe-rubredoxin fraction presented an A_{280}/A_{493} ratio of 2.4.

II.3.3 NMR titration

II.3.3.1 Sample preparation

Protein samples for the 1D NMR titration were dialyzed against 10 mM Tris–HCl pH 7.6 overnight before being lyophilized three times. Between each lyophilization step, samples were re-suspended in a small amount of $^{2}H_2O$. The concentrations were adjusted to 750 μM for cytochrome c_3 and 3 mM for Fe-rubredoxin and Zn-rubredoxin. Before the titration, the pH was adjusted to 8.0 using 1:500 solutions of ^{2}HCl and $NaO^{2}H$ in $^{2}H_2O$ (not corrected for isotope effect). Protein samples for the 2D NMR titration were desalted into 10 mM Tris–HCl pH 7.6 using a HiTrap Desalting™ column

(GE Biosciences). The NMR samples used in the 2D titration contained 550 μM ^{15}N–Zn-rubredoxin and 300 μM cytochrome c_3 in 10 mM Tris–HCl pH 7.6 and 10% ^{2}H2O.

II.3.3.2 ^{1}H NMR titration

Aliquots of the Fe-rubredoxin or Zn-rubredoxin were added to a 750 μM cytochrome c_3 solution, up to a [Rubredoxin]/[cytochrome c_3] ratio of 3.0. The ^{1}HNMR spectra were obtained at 298 K on a Bruker AMX-400 NMR spectrometer equipped with a QNPz probe and a temperature control unit. Spectra were processed using TOPSPIN 2.0 (Bruker), and TSP (Trimethylsilyl propanoic acid) was used as an internal reference.

II.3.3.3 2D NMR titration

Aliquots of *D. gigas* cytochrome c_3 were added to 550 μM ^{15}N– Zn-rubredoxin solution up to a ratio [cytochrome c_3]/[^{15}N–Zn-rubredoxin] of 1.6. A ^{1}H–^{15}N HSQC spectrum was recorded after the addition of each aliquot. Titrations were performed at 298 K with spectra recorded on a Bruker Avance III Ultrashield 600 MHz spectrometer equipped with a CP TCI cryo-probehead and a temperature control unit. Spectra were processed using TOPSPIN 2.0 (Bruker) and analysed with CARA [21]. The *D. gigas* cytochrome c_3 induced changes in amide peak position of ^{15}N-Zn-rubredoxin, ΔδHN (in ppm) were reported as a combination of the changes in the proton (ΔδH) and nitrogen (ΔδN) dimensions according to the following equation $\Delta\delta_{HN} = \sqrt{\frac{(\Delta\delta H)^2 + \left(\frac{\Delta\delta N}{5}\right)^2}{2}}$ [8].

II.3.3.4 Data analysis of binding

The chemical shift difference of the cytochrome c_3 heme methyls upon binding of Zn- or Fe-rubredoxin was analysed considering a model for a single binding site. The chemical shift difference of the ^{15}N-Zn-rubredoxin amide resonances upon binding of cytochrome $c_3$were analysed using the same approach. The chemical shift difference

was non-linear least-squares fitted using Eq. (1), considering a fast exchange equilibrium $\Delta\delta_{obs} = \Delta\delta_{\max} x_{AB}$ (1), in which $x_{AB} = \frac{[AB]}{[A]_T}$, and [AB] is given by $[AB] = \frac{([K_d] + [A]_T + [B]_T) - \sqrt{([K_d] + [A]_T + [B]_T)^2 - 4 \cdot [A]_T [B]_T}}{2}$. The K_d and the $\Delta\delta_{\max}$ were obtained by simultaneously non-linear least squares fitting the chemical shift difference using equation 1.

II.3.4 Molecular docking simulations

The atomic coordinates of *D. gigas* rubredoxin and cytochrome c_3 were obtained from the Brookhaven Protein Data Bank (PDB files 1RDG and 1WAD, respectively). These coordinates were used as input files for the docking algorithm BiGGER (publicly available from http://www.cqfb.fct.unl.pt/bioin/chemera/), which performs a complete and systematic search (grid-like, in which the protein volume is divided into 1 $Å^3$ cubes, which are ranked as "surface" or "core" cubes) of the rotational space of one protein relative to the other and creates a series of putative docking geometries based on the complementarity of the molecular surfaces. This complementarity enables partial side-chain overlap (i.e., some overlapping of "core" cubes) to account for their flexibility (soft-docking). The top 5000 docked solutions are then evaluated and ranked using several additional criteria (electrostatic energy, solvation energy, and aminoacid pairwise affinity), which constitute a ''Global Score". In the present case, a restrained docking approach was applied, in which the distance between cytochrome c_3 heme IV's $M2^1$ and $M18^1$ methyls and the surface of rubredoxin was kept at the maximum distance of 4 Å. The top 5000 docked solutions were then evaluated and ranked using several additional criteria (electrostatic energy, solvation energy, and aminoacid pairwise affinity), which constitute a ''Global Score". The top 300 electrostatic energy minimization-ranked solutions, were further analyzed and ranked according to the minimum distance between the iron of rubredoxin's center and cytochrome c_3 heme IV's $M2^1$ or $M18^1$ methyls. The top 150 solutions were evaluated individually calculating the ($d_{Fe\text{-}M18}/d_{Fe\text{-}M2}$) ratio, which we expected to be ~1.3 according to the

experimental data (see below for further details). The 3 top models that fitted this criterium were analysed using the PROTORP (Protein–Protein Interaction Analysis) website (www.bioinformatics.sussex.ac.uk), in order to analyze the complex interface: determination of the number of possible salt bridges and hydrogen bonds, the properties of the interface (percentage of polar and non-polar residues), and the number of residues that comprise the binding surface.

II.4 Results and Discussion

II.4.1 Complex formation studied by ^{1}H NMR: the paramagnetic effect

Cytochrome c_3 presents itself as an interesting target to study the interaction with proteins containing rubredoxin-like metal centers. The ^{1}H NMR spectrum of the oxidized *D. gigas* cytochrome c_3 (Fig. II.2, spectrum (i) and Fig. II.3, spectrum (i)), presents several well-resolved resonances assigned to the heme methyl groups' protons (11 of the maximum expected 16), which are shifted to the low-field region due to the paramagnetic effect of the oxidized heme iron. The addition of Fe-rubredoxin to cytochrome c_3 (Fig. II.3, spectra ii) to iv)) affects the heme methyl resonances of cytochrome c_3 in two different ways which becomes clearer upon analysis of the difference spectrum between [Fe- rubredoxin]/[cytochrome c_3] molar ratio of 3 and 0 (Fig. II.2, (v)): while five heme methyl resonances belonging to all heme groups experience significant shifts: M2^1 of heme I, $\Delta\delta$ = 0.12 ppm, M7^1 of heme II, $\Delta\delta$ = 0.09 ppm), M2^1 of heme III, $\Delta\delta$ = 0.13 ppm, M12^1 of heme III, $\Delta\delta = 0.18$ ppm and M2^1 of heme IV, $\Delta\delta$ = 0.21 ppm (Table II.1).

However, only two heme methyl resonances from heme IV exhibit line broadening: M18^1 and more strikingly, M2^1 (all heme nomenclatures are given according to the IUPAC recommendations [22]). The chemical shift difference for those heme methyl resonances during the titration was normalized and is presented in Fig. II.5A. It is clear that all the heme methyl resonances exhibit an identical behavior in the course of the titration, regardless of the heme group they belong to (*vide infra*).

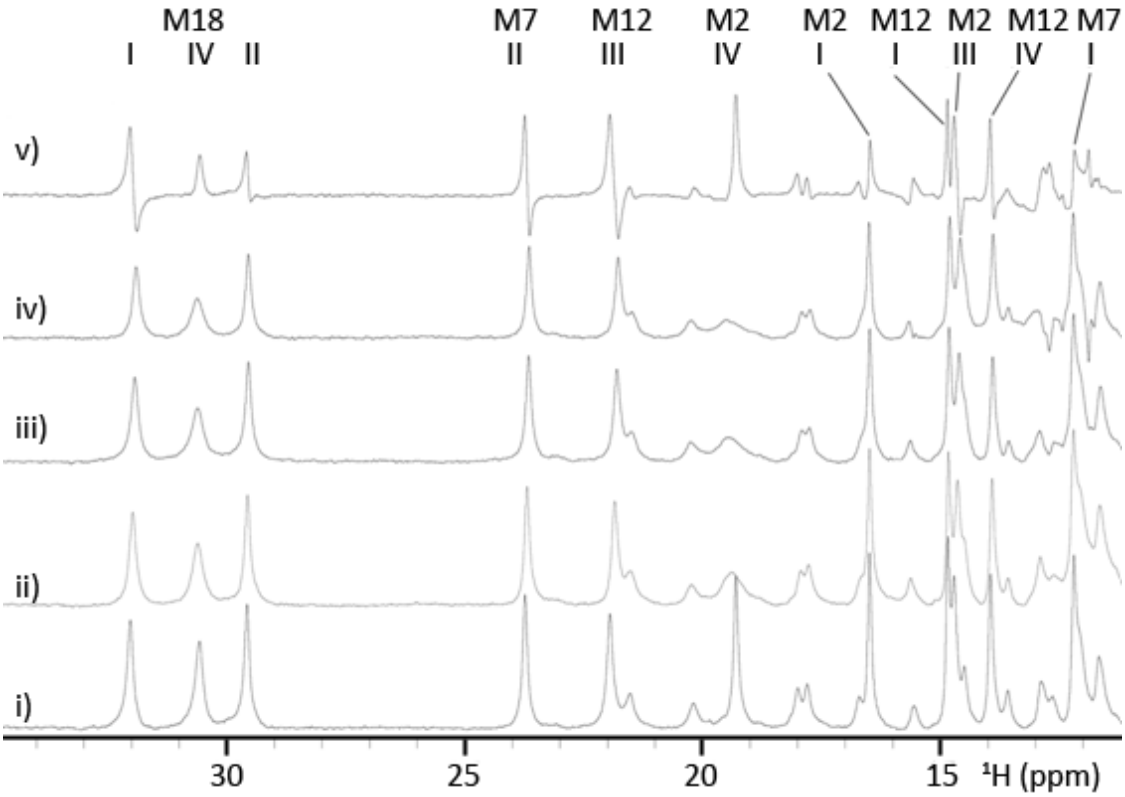

Figure II.3 – ^{1}H NMR titration of oxidized *D. gigas* cytochrome c_3 with Fe-rubredoxin. The spectra are zoomed in to show the low-field region (34 – 11 ppm) containing the cytochrome heme methyl resonances labelled according to the IUPAC recommendations. The spectra was acquired at pH 8.0, 298 K and I = 1.3 mM, as described in Materials and Methods. The protein samples were (i) R=0, 750 μM cytochrome c_3, (ii) R=0.5, (iii), R=1.0, (iv) R=3.0. Spectrum v) is the difference spectra between [rubredoxin]/[cytochrome c_3] ratios of 3.0 and 0.

This may arise from small conformational changes in the vicinity of the binding surface upon formation of the complex that are then transferred to the rest of the cytochrome c_3 molecule, and are reflected in the chemical environment around the other hemes [23]. As mentioned before, the half-height linewidth of heme IV's M2^{1} methyl resonance increases from 44 to 240 Hz, as the ^{1}HNMR titration with Fe-rubredoxin progresses (Fig. II.5B).

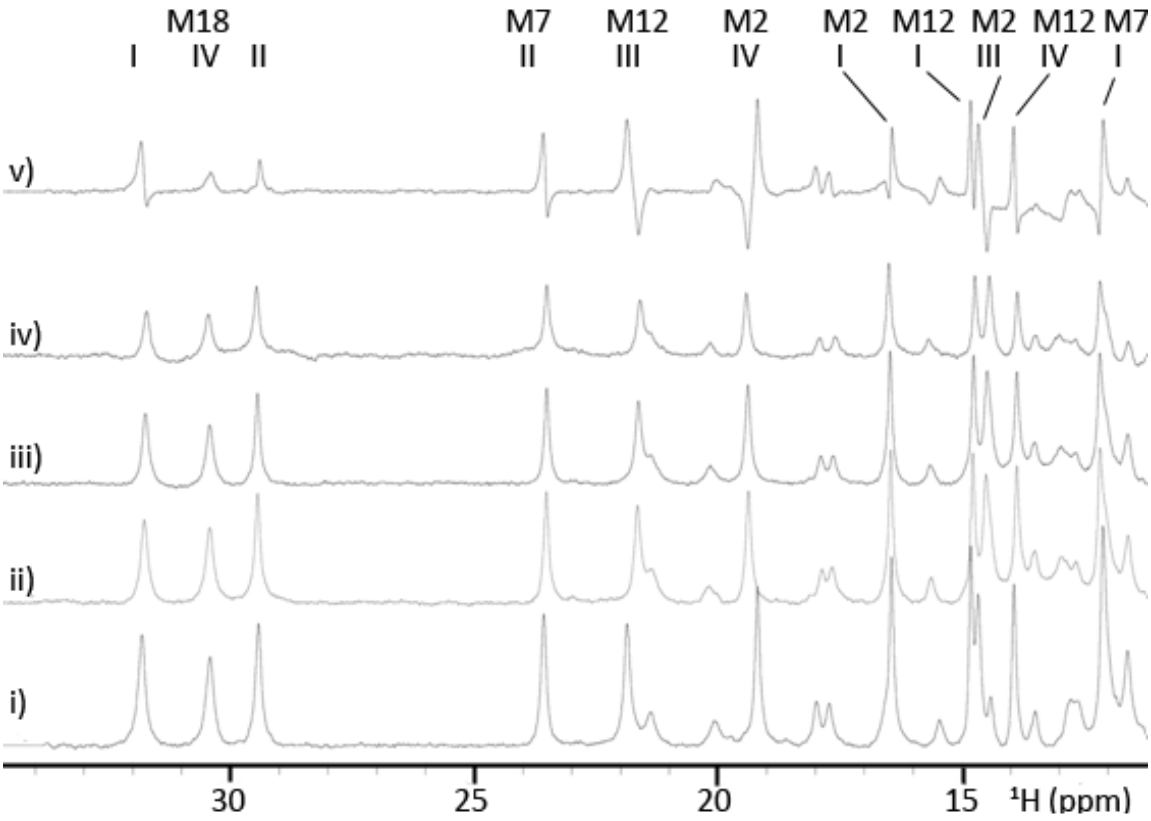

Figure II.4 – ^{1}H NMR titration of oxidized *D. gigas* cytochrome c_3 with Zn-rubredoxin. The same conditions of Figure II.3 apply.

Regarding heme IV's M18 methyl resonance, there is an increase in the half-height linewidth from 73 to 113 Hz (Fig. II.5B), while the other heme methyl resonances experience an average line broadening of 5 ± 1 Hz. The plot of the half-height linewidth of these resonances during the titration has a similar behavior to the one of the normalized chemical shift difference of the heme methyl resonances shown in Fig. II.5A. This specific line width broadening could be attributed to the presence of a high-spin paramagnetic iron, such as the rubredoxin center, in the vicinity of these heme methyl protons. Moreover, the comparison of the increase in the half-height linewidth of those two heme IV's methyl resonances would indicate that the distance between the paramagnetic center, the rubredoxin Fe ion, and cytochrome c_3 heme IV's M2 methyl is shorter than the one to cytochrome c_3 heme IV's M18 methyl (*vide infra*).

Table II.1 – Chemical shift variation of assigned heme methyl resonances upon addition of 3 equivalents of either Fe- or Zn-rubredoxin per cytochrome c_3

		Chemical Shift Variation (ppm)	
		Fe	**Zn**
Heme I	M2	-0,12	-0,12
	M7	-0,02	-0,01
	M12	-0,04	-0,04
	M18	-0,01	-0,01
Heme II	M7	-0,09	-0,09
	M18	-0,04	-0,04
Heme III	M2	-0,13	-0,13
	M12	-0,18	-0,18
Heme IV	M2	0,21	0,2
	M12	-0,06	-0,06
	M18	-0,06	-0,06

In order to confirm this hypothesis, cytochrome c_3 was titrated with Zn-rubredoxin, which is diamagnetic, and the results are presented in Fig. II.3 (spectra ii) to iv). The chemical shift difference observed for the heme methyl resonances of cytochrome c_3 in this titration is identical to the ones mentioned above for the titration with Fe-rubredoxin (Table II.1). The difference spectrum (Fig. II.4, (v)) exhibits a clear down-field shift and a small line broadening for heme IV methyl resonance M2, 5 ± 1 Hz, and a similar value is observed for the line broadening of heme IV methyl resonance M18.

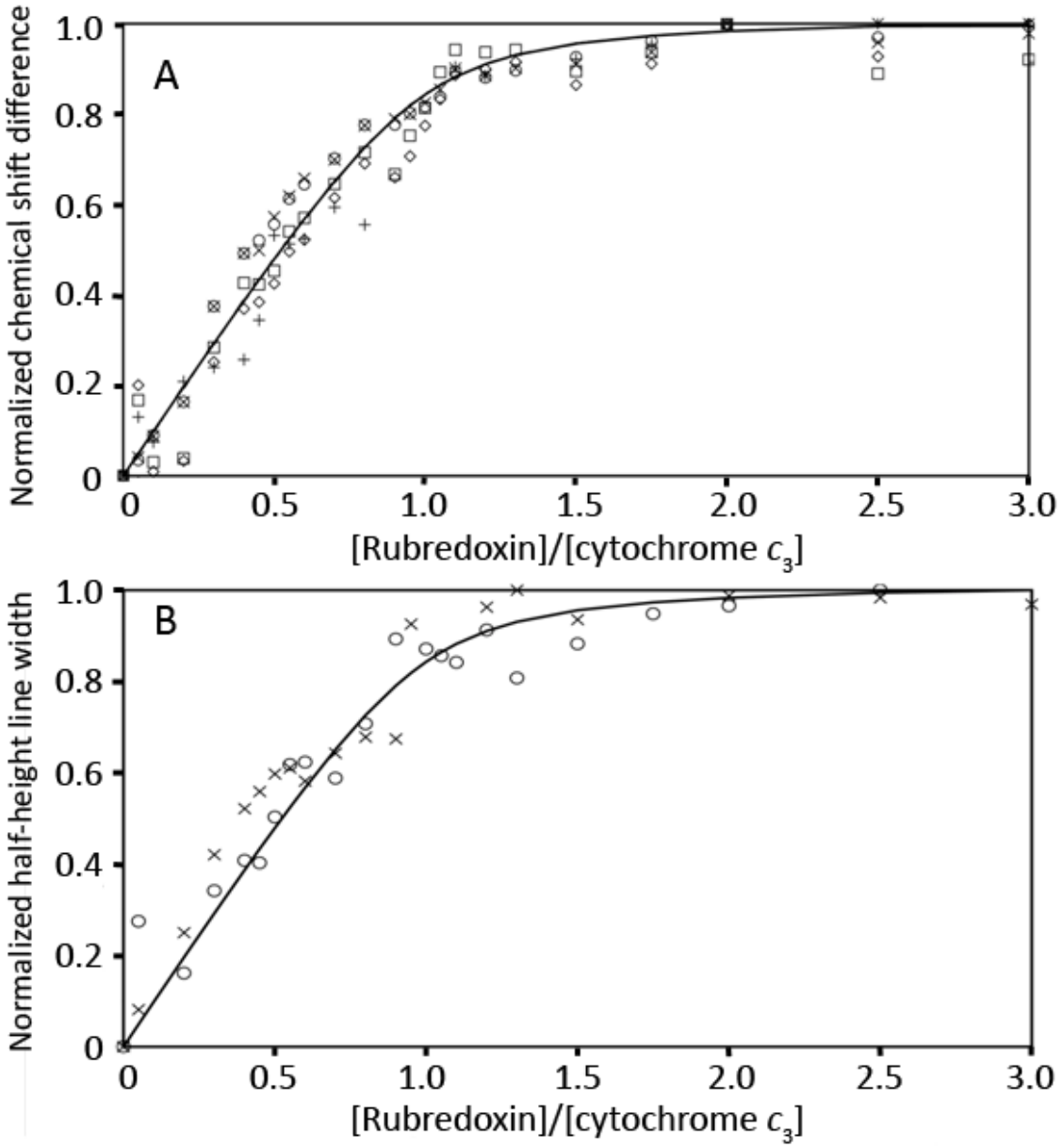

Figure II.5 – A) Normalized chemical shift variation of *D. gigas* cytochrome c_3 heme methyl resonances: heme I $M2^1$ (◊), heme II $M7^1$ (□), heme III $M2^1$ (O), heme III $M12^1$ (×) and heme IV $M2^1$ (+), with increasing molar ratios of Zn- or Fe-rubredoxin. B) Normalized half-height line width variation of *D. gigas* cytochrome c_3 heme IV methyl resonances $M18^1$ (O) and $M2^1$ (×) during the titration with D. gigas Fe-rubredoxin. The fitting curves in both panels were simulated for a single binding site with a K_d of 25 ± 2 μM, as described in Section II.3.2.

The same line broadening was determined for of all other cytochrome c_3 heme methyl resonances during this titration, which is consistent with the values measured for the Fe-rubredoxin titration (except the ones from heme IV mentioned earlier).

This small increase can be explained by the increase in tumbling time caused by the concomitant increase in molecular weight due to complex formation. Therefore, since both proteins used in this study were fully oxidized, the linewidth broadening cannot be ascribed to electron transfer reactions [24], and thus is attributed to the binding of a paramagnetic protein in the vicinity of those heme methyl resonances. In fact, only the half-height linewidth of heme IV's M2 and M18 methyl resonances decrease by a factor of 1.4 upon addition of sodium ascorbate to the sample at the end of the titration with Fe-rubredoxin (data not shown). This can be explained by the fact that the reduction of Fe-rubredoxin changes its spin from 5/2 to 2, and the paramagnetic contribution to the linewidth is expected to decrease by a factor of 1.46, according to the Solomon–Bloembergen equation [25, 26] (see also Chapter III), which is in agreement with the experimental result. The Solomon-Bloembergen equations state that the relaxation effects brought upon by paramagnetic species depend not only on the reciprocal of the sixth power between a nucleus and the paramagnetic species, but also on the number of unpaired electrons [S(S+1)].

Moreover, as the specific line broadening is due to the presence of a paramagnetic ion in close proximity to cytochrome c_3 heme IV's M2 and M18 methyls, it is possible to infer from the ratio between the line broadening of those resonances (196/40 = 4.9) that the ratio between $(d_{Fe\text{-}M2}/d_{Fe\text{-}M18})^6$ should have a similar value (Note: $(d_{Fe\text{-}M2}/d_{Fe\text{-}M18})^6 = (4.9)^{1/6} = 1.3$). This experimental constraint will be taken into account in the analysis of the model structure of the complex.

II.4.2 Determination of the binding constant between cytochrome c_3 and rubredoxin

The chemical shift variation observed for some of the heme methyl resonances shows that the complex is in fast exchange in the NMR time scale (Fig. II.2 and II.3), and increases with the molar ratio of [rubredoxin]/[cytochrome c_3] up to 1, indicating that the stoichiometry of the complex is 1:1 when either Zn-rubredoxin or Fe-rubredoxin is added (Fig. II.4A). Therefore, fitting all data sets to a 1:1 equilibrium as described in Section II.2.3.4, a K_d of 25 ± 2 μM for the binding of rubredoxin to cytochrome c_3 was estimated. The half-height line width of cytochrome c_3 heme IV's M18 and M2 methyl resonances was also fitted using that equation, and an identical value for the K_d was estimated, 25 ± 2 μM (Fig. II.5B). The estimated value for the K_d for this complex is of the same order of magnitude as those estimated for other electron transfer complexes involving heme proteins at low ionic strengths [10, 27, 28]. However, it is important to mention that the K_d estimated by the NMR titration is not an accurate value but simply the upper limit due to the high protein concentration used in these experiments.

Nevertheless, this intermediate value for the K_d confers a transient character to the complex, which is needed to enable a high-turnover, and a controlled flow of electrons [29, 30]. Indeed, a similar K_d was obtained for model electron transfer complexes involving cytochrome c_3 from other species from the *Desulfovibrio* genus [31], and the one of cytochrome c_3 with ferredoxin I from *Desulfomicrobium norvegicum* [32]. In the present work, as well as in other electron transfer complexes involving cytochrome c_3 [23, 31-33], five of the eleven observed heme methyl resonances shifted upon addition of either Zn- or Fe-rubredoxin, but only two of these resonances experience line broadening due to the paramagnetic effect. These belong to heme IV, which is the one with a prominent positively charged patch around it (Fig. II.6 E and F); heme IV is also the heme group with the highest redox potential. The observation that chemical shift differences are not limited to the interacting heme group may be due to a secondary effect caused by small changes in the backbone upon rubredoxin binding [23].

II.4.3 2D NMR titration of Zn-rubredoxin with cytochrome c_3

The *D. gigas* rubredoxin residues involved in the binding surface with *D. gigas* cytochrome c_3 were identified in a heteronuclear 2D NMR titration (Fig. II.6A), by following the changes in the ^{1}H–^{15}N HSQC spectra of ^{15}N-labelled Zn-rubredoxin upon addition of unlabelled cytochrome c_3. The complex is in fast exchange in the NMR time scale (Fig. II.3 and II.4) and the binding shifts ($\Delta\delta_{avg}$) were determined as described in Section II.3. The analysis of the binding chemical shifts shows that there are 18 residues in the surface of rubredoxin that are affected due to the binding of cytochrome c_3 (Fig. II.6A and II.7). These residues can be divided into two classes: the ones which the amide proton has a 0.05 > $\Delta\delta_{avg}$ > 0.025 ppm (11 residues) and the ones which amide proton has a $\Delta\delta_{avg}$ > 0.05 ppm (seven residues). These residues are located at the surface near the iron center of rubredoxin (Fig. II.7B), and some are involved in the interface of the complex while others might be experiencing a secondary effect due to binding, as explained above.

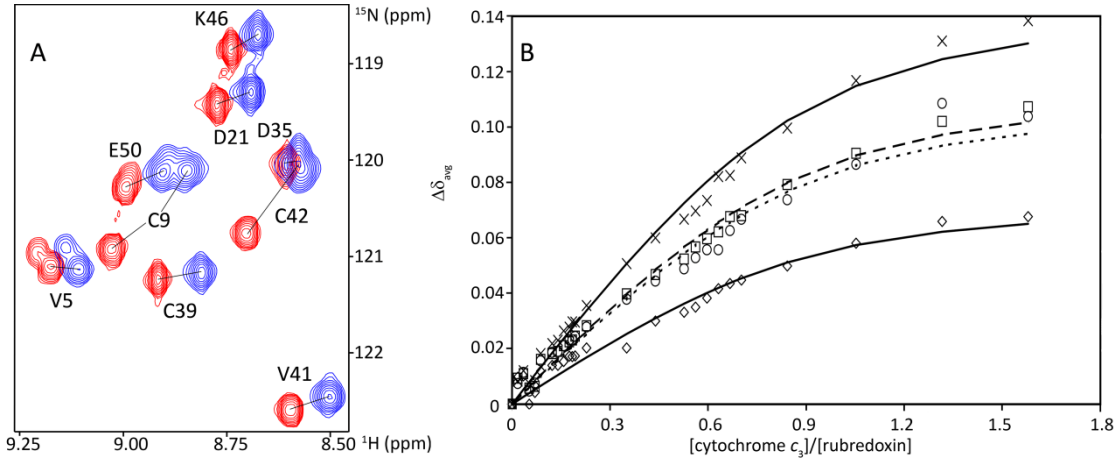

Figure II.6 - (A) Partial view of the [^{1}H, ^{15}N] HSQC spectrum of 550 µM Zn-rubredoxin acquired in a Bruker AvanceIII 600 MHz spectrometer equipped with a cryoprobe, at 298 K in 10 mM Tris–HCl pH 7.6, in the absence of cytochrome c_3 (red lines) and in [cytochrome c_3]/[rubredoxin] = 1.5 (blue lines). (B) Chemical shift variation of some *D. gigas* rubredoxin amide resonances with increasing molar ratios of *D. gigas* cytochrome c3: V8 (◊), C9 (×), C42 (O) and S45 (◊). The fitting curve was simulated for a single binding site with a K_d of 25 ± 2 µM, as described in Section II.3.3.4.

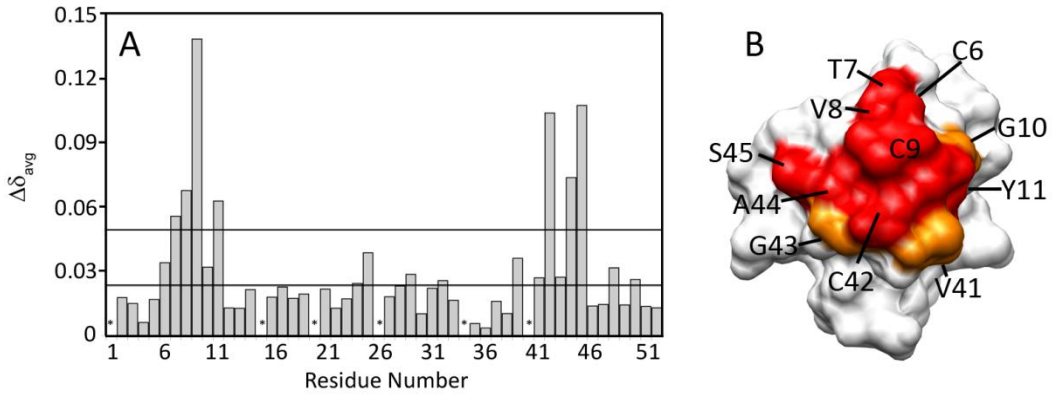

Figure II.7 - (A) Chemical shift change of the cytochrome c3-rubredoxin complex, determined by heteronuclear 2D NMR titration at 298 K in 10 mM Tris–HCl buffer, pH 7.6, as described in Section 2. (B) Mapping of the interacting surface of rubredoxin with cytochrome c_3. The residues are coloured according to their $\Delta\delta_{avg}$: in white are residues with $\Delta\delta_{avg}$ < 0.025, in orange are residues with 0.025 < $\Delta\delta_{avg}$ < 0.050 ppm and in red residues with $\Delta\delta_{avg}$ > 0.050 ppm.

A K_d estimation based on the shifts of selected resonances near rubredoxin metal center (Fig II.6B) yielded similar results to the ^{1}H NMR titration, as expected (K_d = 25 ± 2 μM).

II.4.4 Model structure of cytochrome c_3 – rubredoxin complex

A model structure for the complex between rubredoxin and cytochrome c_3 was obtained using a soft docking algorithm called BiGGER [34] and the deposited coordinates of both proteins, as described in Section II.3.4. A restraint docking approach was applied, in which the distance between cytochrome c_3 heme IV's M2 and M18 methyl groups and the surface of rubredoxin was kept at a maximum distance of 4 Å. The solutions obtained in this restrained docking were ranked according to the electrostatic energy minimization, since these two proteins present a large charge asymmetry (Fig. II.8 panels B, C, E and F). The 300 top electrostatic- ranked solutions are depicted in Fig. II.7A, showing a clear preference for the region surrounding heme IV. The distance of rubredoxin iron atom and cytochrome c_3 heme IV's M2 and M18 methyls was determined for these model structures (Fig. II.8 B).

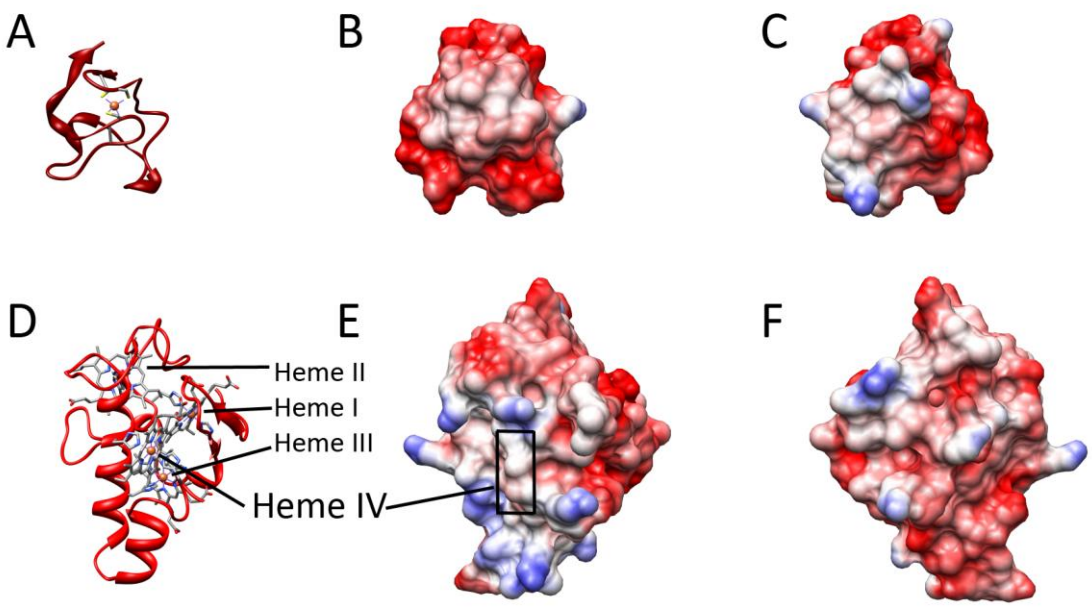

Figure II.8 - Structure of *D. gigas* rubredoxin (A–C) and *D. gigas* cytochrome c_3 (D–F). Rubredoxin is depicted as backbone coloured in dark red, with the iron ion displayed as an orange sphere and facing the reader (Panel A). Rubredoxin is displayed with its surface coloured by electrostatic potential in the same orientation as in A (Panel B), or after a 180º rotation in the vertical axis (Panel C). Cytochrome c_3 is depicted as backbone coloured in red, with heme IV coloured blue and other hemes coloured grey (Panel D), and with its surface coloured by electrostatic potential in the same orientation as in D (Panel E) or after a 180º rotation in the vertical axis (Panel F). The electrostatic surface was calculated and displayed in terms of Gasteiger charges, where blue represents positive charges and red negative charges. Figures were prepared with UCSF Chimera [35], using 1RDG.pdb (Panels A–C) and 1WAD.pdb (Panels D–F).

The model structures that were further analysed in terms of surface residues were the ones with a $(d_{Fe\text{-}M2}/d_{Fe\text{-}M18})^6$close to 1.3 (as explained above), which would correspond to the model structure that better fitted the ^{1}H NMR titration data.

In the top structure model shown in Fig. II.8C, the distance between the iron ion of rubredoxin and the heme IV methyl M2, M18, M12 and M7 is of 3.4, 4.5, 13.1 and 11.7 Å, respectively, which is consistent with the ^{1}H NMR titration data, in which it was only observed a broadening in the first two heme methyl resonances (Fig. II.3), attributed to the enhanced relaxation caused by the proximity of the high-spin iron of rubredoxin

center. The binding surface of this model encounter complex is composed mainly by charged (36%) and non-polar (36%) residues. The rubredoxin interface in this complex is composed by the residues T7, V8, C9, Y11, P40, V41 and C42 (Fig II.9D, red), which is consistent with the surface mapping obtained from the 2D NMR titration (Fig. II.6B). In this model there is also one hydrogen bond (between the peptide bond of rubredoxin's C42 and cytochrome c_3's K60), the accessible surface area is around 570 Å and the gap volume index of around 3.2 Å. As mentioned, these two proteins present an asymmetric electrostatic surface. Rubredoxin surface is negatively charged near the metal center (Fig. II.8A and B). On the other hand, cytochrome c_3 has a positively-charged lysine patch surrounding a hydrophobic surface where heme IV protrudes the surface (Fig. II.8D and E), which may be instrumental in bringing rubredoxin into close proximity to the heme crevice. The existence of negatively charged residues (D59 and D62) forming intramolecular salt bridges with some of these lysine sidechains (K60 and K70, for instance), should be instrumental in order to avoid strong binding that would prevent the fast dissociation of the complex, a feature common to other electron transfer proteins [36, 37]. As described above, in both proteins these charge patches surround a hydrophobic region that would be important for an efficient electron transfer [36, 37]. In conclusion, the interface of this non-physiological complex shares properties with other competent physiological complexes, such as a small interface area, a high percentage of the interface composed by non-polar residues (36%), which provides a suitable environment for electron transfer, and the presence of one hydrogen bond that might help in the formation of the transient complex, driving the partners to the optimum orientation for electron transfer.

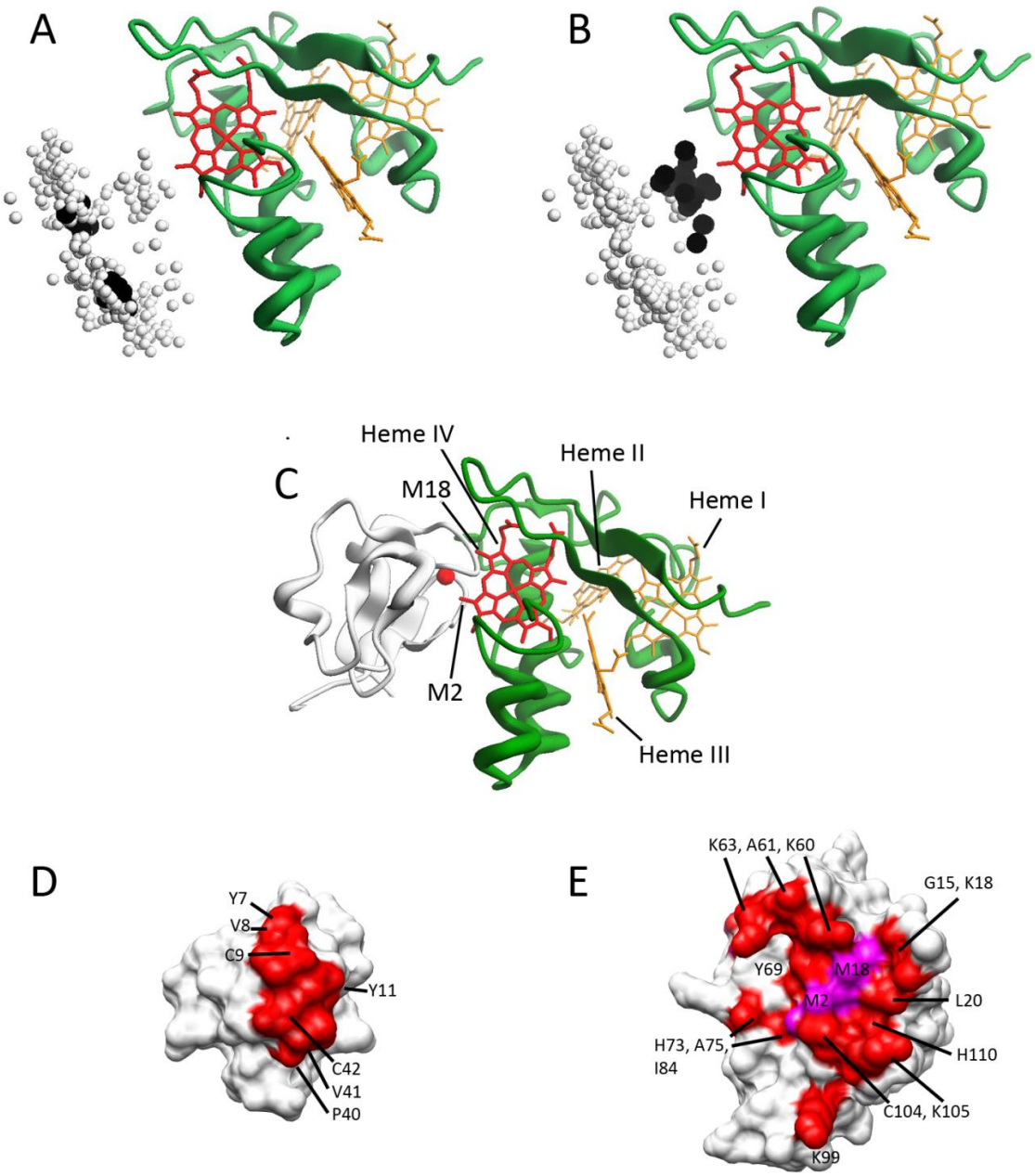

Figure II.9 - A) 300 top model complexes ranked by the Electrostatic energy minimization score of the restrained docking of cytochrome c_3 with rubredoxin. B) Same as in A and showing the top 20 best solutions that have the shorter distance between rubredoxin iron and cytochrome c_3 heme IV methyl M2 or M18 (as described in Section II.2). In Panel A and B the iron of rubredoxin of each putative model complex is represented as a grey-coloured sphere while the top 20 solutions are represented as larger, black-coloured spheres. Panel C shows the top model structure of this complex. In Panel A–C, *D. gigas* cytochrome c_3 is displayed in the same orientation with green backbone and with heme IV coloured red and the others coloured orange. In Panel C, rubredoxin is represented with a grey backbone with the iron as a red-

coloured sphere. Panels D and E represent the residues involved in the interface in the *D. gigas* rubredoxin (panel D)-cytochrome c_3 (panel E) model complex. The involved residues are coloured red and labeled accordingly. These residues were identified using the PROTORP server. Panels A, B and C were prepared using Chemera, BiGGER's companion molecular graphics software, and panels D and E were prepared using UCSF Chimera [35].

II.5 Conclusions

In the present work, it was shown that rubredoxin can be used as an effective paramagnetic relaxation probe for NMR spectroscopy-based studies. The distinctive properties of its Fe center can be exploited to study protein–protein interactions, and even the application of simple experiments as ^{1}HNMR titration can provide valuable information to characterize the interaction (stoichiometry and magnitude of the binding constant) when the redox partner is also a paramagnetic protein. In addition, 2D heteronuclear NMR experiments were used to identify the rubredoxin surface that interacts with cytochrome c_3. The information attained in the NMR experiments can be combined with a molecular docking algorithm to obtain a model structure of the complex. In the present case study, it is observed that rubredoxin binds preferentially near cytochrome c_3 heme IV with a 1:1 stoichiometry, as inferred from the specific linewidth broadenings of the resonances of the two most exposed heme IV methyl groups, caused specifically by the paramagnetism of the Fe center. In addition, rubredoxin's binding surface is negatively charged and includes two exposed cysteinyl ligands of the iron–sulfur center, as determined in the heteronuclear 2D NMR experiments. Furthermore, based on chemical shift differences and line broadenings, it was possible to estimate an apparent K_d of 25 ± 2 μM, consistent with the formation of a protein complex. These experimental data were used to analyze and filter the *in silico* molecular docking simulation using the BiGGER algorithm, which predicts an interaction of electrostatic nature, with rubredoxin binding near cytochrome c_3 heme IV. Therefore, it is proposed that this methodology can be applied to the characterization of complexes formed between rubredoxin and its known electron transfer partners, superoxide reductase, rubredoxin oxygen-oxidoreductase and NADPH:rubredoxin oxidoreductase. Moreover, in the case of electron transfer complexes in which one of the partners is an iron–sulfur protein with similar properties as rubredoxin, this small redox protein can be used as its substitute especially when the heterologous expression or purification becomes too cumbersome for that protein. In conclusion, the plasticity of rubredoxin isolated from *D. gigas*, or from other bacterial sources, makes rubredoxin the protein of choice to be used in several studies,

such as theoretical solid state NMR [38], or the characterization of specific structural elements that influence the rate of hydrogen exchange rates of protein backbone amides [39], and in the present work, as a paramagnetic probe to study protein–protein complexes.

Chapter III – Gd(III) chelates as protein interaction probes

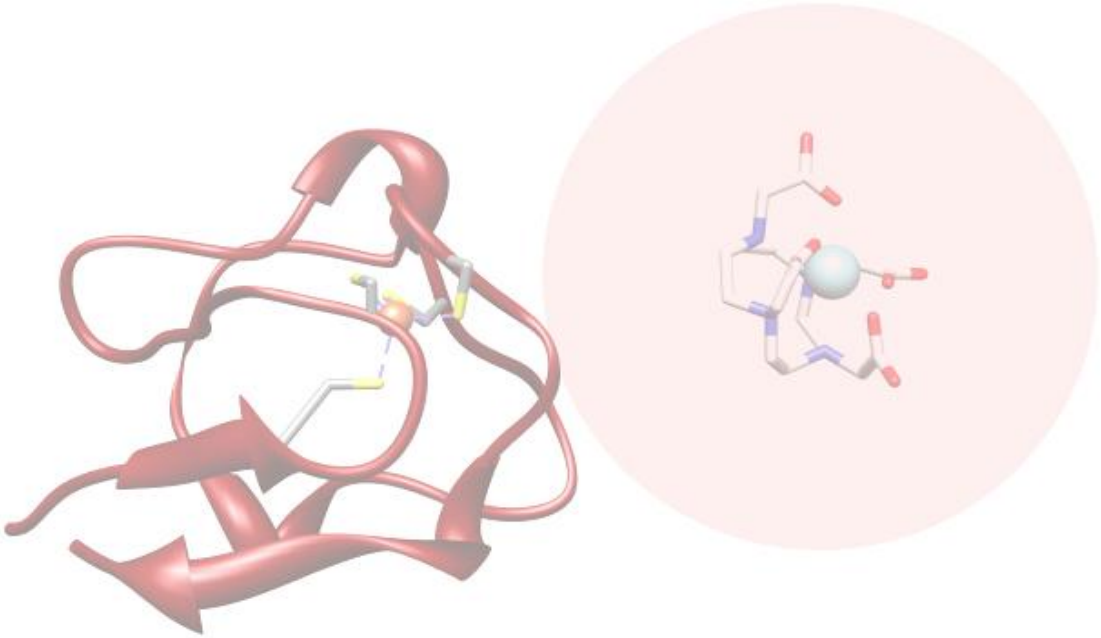

Index

III.1 Abstract

In this chapter two cyclen-derived Gd probes, DOTAM (positively charged) and DOTP (negatively charged) were assessed as paramagnetic relaxation enhancement-inducing probes for characterization of protein-protein interactions. Two proteins, *D. gigas* rubredoxin and *D. gigas* cytochrome c_3 were used as model partners. In a ^{1}H NMR titration it was shown that Gd-DOTP binds to cytochrome c_3 near heme IV, causing pronounced PREs, characterized by linewidth broadenings of its methyl resonances at ratios as low as 0.05. A K_d of 30 μM was calculated based on heme methyl line width broadenings and chemical shift perturbation, in an equilibrium with a stoichiometry of 1 cytc_3 : 1 Gd-DOTP. The other probe, Gd-DOTAM, also caused PREs on a well-defined patch near the metal center of rubredoxin (specially residues A38-A44 which broaden beyond detection). This effect was partially reversed for some resonances (T7-C9, Y11-Y13, D21, G23, D36, W37 and S45-A48) when cytochrome c_3 was added to this system. Both probes were successful in causing PREs at large distances from the binding site, thus showing to be good, reversible probes for protein complex characterization.

III.2 Introduction - Gd(III) chelates as protein interaction probes

Lanthanides have recently been the object of magnetic resonance-based studies, both in terms of fundamental research and of clinical-based approaches. The 14 elements that constitute the lanthanide family possess atomic radii comparable to alkali and earth alkali metals (≈0.8-1.3 Å), and, though chemically similar, their trivalent ions exhibit a wide range of tunable magnetic characteristics due to the varying number of unpaired electrons and anisotropy [1]. In the magnetic resonance field, one point of interest lies in the wide variety of diamagnetic and paramagnetic states of their trivalent ions.

Paramagnetism arises from unpaired electrons. In the case of trivalent lanthanide ions, these unpaired electrons lie in chemically unreactive 4*f* orbitals, which are also shielded from the ligand fields by the outer-lying 5*s* and 5*p* orbitals [2]. The majority of lanthanide ions is anisotropic in terms of electronic distribution in their *f* orbitals, and thus they present lower-lying spin energy levels, promoting large anisotropies in the magnetic susceptibility tensor (χ). This tensor describes the changes in properties of the nuclei magnetic momenta in terms of magnitude and directionality relative to the orientation to an applied magnetic field. As such, several lanthanides (with the exception of Gd, see below) are capable of causing pronounced lanthanide induced shifts (LIS), which can be of contact, dipolar or Curie-spin in origin [3].

Some of these lanthanides have very large J values [Dy(III) and Et (III) = 15/2, Ho(III) = 8, for instance], and in these cases the strong anisotropy leads to a very fast relaxation of the electron momentum [4] (Please note that the total angular momentum number, *J*, is used instead of *S* to account for spin-orbit coupling which is usually not negligible for lanthanides. *J* results from the sum of the intrinsic spin momentum and the orbital angular momentum, i.e., $J = S + L$). Concomitantly, a number of lanthanide-containing complexes put to use the increased pseudocontact shifts (PCS) with negligible Fermi contact shifts to good use (Curie-spin relaxation mechanisms only occur in non-negligible magnitudes for very high magnetic fields for some lanthanides), in both MRI and paramagnetic NMR [5, 6]. Since PCS depend on $1/r^3$ (Eq. 1), with r representing the

distance between the paramagnetic center and the affected nucleus, it is possible to observe PCS on nuclei at distances up to 40 Å (in the case of Dy(III)).

Paramagnetic relaxation enhancements (PREs) exhibit a $1/r^6$ dependence and are readily represented by the Solomon-Bloembergen equations (Eqs. 2 and 3)

$$\Delta\delta_{pcs} = \frac{1}{12\pi r^3}\left(\Delta\chi_{ax}\,[3\cos 2\theta - 1 + \frac{3}{2}\Delta\chi_{rh}\,\sin 2\theta\cos 2\varphi\right)\ (eq.1)$$

$$\frac{1}{T_{1,dip}} = \frac{2}{15}\left(\frac{\mu_0}{4\pi}\right)^2 \frac{\gamma_I^2 g_e^2\,\mu_B^2 J(J+1)}{r^6}\left(\frac{3\tau_{c1}}{1+\omega_I^2\tau_{c1}^2} + \frac{7\tau_{c2}}{1+\omega_S^2\tau_{c2}^2}\right) \text{ (eq. 2)}$$

$$\frac{1}{T_{2,dip}} = \frac{1}{15}\left(\frac{\mu_0}{4\pi}\right)^2 \frac{\gamma_I^2 g_e^2\,\mu_B^2 J(J+1)}{r^6}\left(4\tau_c + \frac{3\tau_{c1}}{1+\omega_I^2\tau_{c1}^2} + \frac{13\tau_{c2}}{1+\omega_S^2\tau_{c2}^2}\right) \text{ (eq. 3)}$$

where μ_0 is the magnetic permeability of vacuum, μ_{eff} is the effective magnetic moment, r is the distance between nuclei , $\Delta\chi_{ax}$ and $\Delta\chi_{rh}$ are the axial and rhombic components of the magnetic susceptibility tensor, θ and φ are the spherical coordinates of the nuclei, and τ_c is the total correlation time, which is given by (eq. 4):

$$\frac{1}{\tau_{ci}} = \frac{1}{T_{ie}} + \frac{1}{\tau_M} + \frac{1}{\tau_R} \text{ (eq. 4).}$$

where τ_R is the rotational tumbling time of the complex, τ_M is the chemical exchange correlation time and T_{ie} are the longitudinal and transverse electronic relaxation times. As can be inferred from the above equations, relaxation times decrease sharply with increasing distance from the lanthanide ion. However, at short distances, its effects can be quite dramatic - up to 40% of the Larmor frequency for a proton at 5 Å from the paramagnetic source [7].

The major disadvantage in using PCS as paramagnetic restraints is the difficulty in deconvoluting the information that arises from the anisotropy of the magnetic susceptibility tensor. Aside from PCS, processes such as contact shifts (rare for lanthanides that do not bind covalently to the probed species), Curie-spin relaxation

(CSR) and cross-correlation effects (CCR) can also affect the observed shifts brought upon by a paramagnetic species [8], thus making difficult, in a first approach, to correctly map the position of the Ln probe on the target protein.

The use of PCS and PREs in protein structure determination and dynamics has been reviewed recently [9].

The various paramagnetic effects of lanthanide ions are summarized in Fig. III.1.

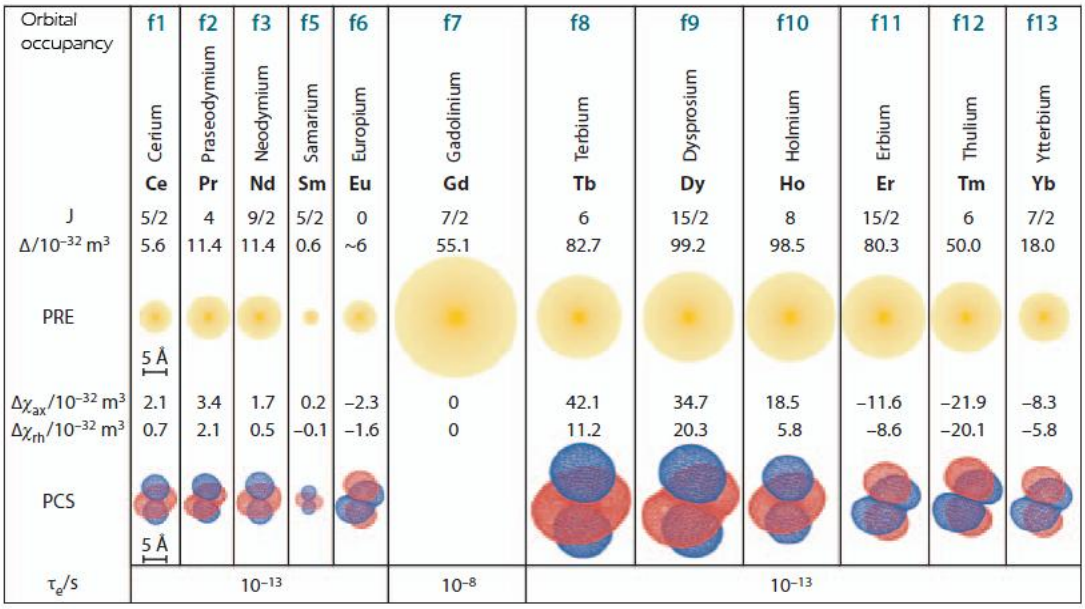

Figure III.1 - Paramagnetic properties of trivalent lanthanide ions. The radii of the yellow spheres indicate the distance from the metal ion where the ^{1}H NMR signals of a protein with a rotational correlation time of 15 ns would be broadened by 80 Hz on an 800 MHz NMR spectrometer due to paramagnetic relaxation enhancement (PRE). The isotropic χ tensors were calculated according to ref. [10], for a temperature of 25ºC. Representative isosurfaces for pseudocontact shifts (PCSs) of □>5 ppm are plotted for Δχ tensors reported for calbindin D_{9k} [11]. Electronic relaxation times expected at 18.8 T are indicated at the bottom. Image from ref. [8].

In the present work, we have chosen Gd(III) chelates for an assessment of their role as PRE-inducing probes. Gd, more than any other lanthanide, has the ability to increase relaxivity of protons (Fig. III.1) due to an isotropic environment of its seven unpaired electrons (J = 7/2). Its electrons have a long relaxation time (usually five or six orders of

magnitude slower when compared to other paramagnetic lanthanides at high magnetic fields), which induce a strong relaxation enhancement of nearby resonating nuclei. This in turn leads to dramatic line width broadenings, but, unlike other metals of the lanthanide series, Gd(III) does not generate any significant PCS, Residual Dipolar Couplings (RDCs) or CCRs. This characteristic is fundamental for accurate distance-dependent measurements [12]. Furthermore, Gd(III) compounds often serve as primers for paramagnetism-based NMR structure calculation experiments by enabling the determination of the metal relative position to the macromolecule under study, which facilitates the analysis of the spectral aspects induced by magnetic susceptibility anisotropy of other lanthanides [11, 13].

However, this lanthanide ion possesses an atomic radius of 0.99 Å in an octa-coordinated state [$Gd(H_2O)_8^{3+}$], very similar to that of Ca^{2+}, and thus can compete with this alkali earth metal by binding to biological molecules *in vivo* – generally with increased affinity, which in turn leads to increased cellular toxicity due to the disruption of calcium ion-dependent processes [14]. Furthermore, soluble Gd^{3+} undergoes rapid hydrolysis, forming the insoluble species $Gd(OH)_3$ [15].

For these reasons, the probes used in human MRI that contain Gd have been designed and tested to become kinetically and thermodynamically stable. Usually, a polydentate organic ligand, such as DTPA or DOTA, with very basic amino or carboxylate groups, can displace most of the water molecules of the *aqua* Gd(III) ion. These Gd(III)-based contrast agents are used to add physiological information about the (abnormal) presence of water-based fluids in organs or changes in relaxation rates [16, 17].

While some macrocyclic-derived Gd probes have been designed to bear substituents that enable them to react specifically with certain proteins or tissues (carbohydrate substituents to react with tissue-specific lectins, for instance [18]), they have also been used in standard biomolecular NMR, bringing to fruition the advantages of the paramagnetic effects they possess [19-21]. One approach of tagging a protein with a lanthanide probe usually consists in expressing fusion proteins with an attached calcium-binding protein, such as calmodulin, in which the calcium ion is replaced by a lanthanide, or a metal-binding peptide to the N-terminal or C-terminal sequence of the

protein under study [22, 23]. This method, however, leads to an increase in molecular weight and number of resonances in the NMR spectra, which may defeat in some cases the purpose of creating the fusion protein.

Lanthanide-binding linkers, such as DTPA (diethylene triamine pentaacetic acid) have also been used in protein structure determination. These consist in small peptides bound to lanthanide chelators, which in turn can bind to one or two cysteine residues via methanesulfothioate groups [22, 24]. However, the formation of diastereoisomers can lead to different orientations of the magnetic susceptibility tensor, originating a large number of additional NMR signals that can overlap and render their analysis much more difficult [25]. In addition, site-directed mutagenesis must also be applied to generate mutants with cysteine residues in positions deemed appropriate to conjugate with the probe, which can alter protein stability and structure. As such, an ideal lanthanide probe would be one that, not only is very stable in chemical and kinetic terms, but also one that does not require modifications of protein structure in order for its effects to be observed. Lately, co-solute paramagnetic moieties without enantiomers have been used for several applications, such as weak self-association determination, visualization of encounter complexes and transient protein-protein interactions (reviewed in [12]). This approach does not need the generation of protein mutants to covalently bind paramagnetic tags, and does not alter protein stability and/or structure. Studies of the non-covalent binding of small charged cationic and anionic paramagnetic chelates to protein surfaces constitute a powerful tool to study protein surface recognition by NMR.

The fundamental molecular process of recognition of a protein surface by another one is largely dependent on long range electrostatic interactions, making the partner proteins approach each other, but its selectivity is mainly driven by very specific short range hydrophobic effects [26, 27]. The potential energy surfaces of the interacting proteins depend on the polarity, size, shape and flexibility of their surfaces, which are determined by the geometric distribution of their cationic and anionic surface residues, which may be concentrated in charged patches [28]. Hydrophobic patches may also be found in those surfaces.

In this chapter, the aim is to assess the use of two DOTA-derived Gd chelates with opposite charge as paramagnetic relaxation-inducing probes (Fig. III.2). One consists of Gd-DOTAM (Gd (III)-1,4,7,10-tetraazacyclododecane-1,4,7,10-tetraacetamide, Fig. III.2), in which the acetate ligands are substituted by acetamide, thus neutralizing the charge of DOTA carboxilate groups and bringing the complex charge to positive values (+3). The other consists of Gd-DOTP (Gd(III)-(1,4,7,10-tetraazacyclododecane-1,4,7,10-tetrakis(methylenephosphonate, Fig. III.2), in which four methylenephosphonate moieties, with two ionizable OH groups, are bound to the cyclen ring nitrogens, thus bringing the total charge of the chelate down to -5. Both are coordinated by a single water molecule at the working pH (7.6). DOTAM has a (distorted) capped square anti-prism geometry, while DOTP generally adopts a twisted square anti-prismatic structure [29]. While both species are present in solution as racemic mixtures of two enantiomers, the interconversion is fast in the NMR time-scale and therefore, only one set of averaged signals is observed in the NMR experiments.

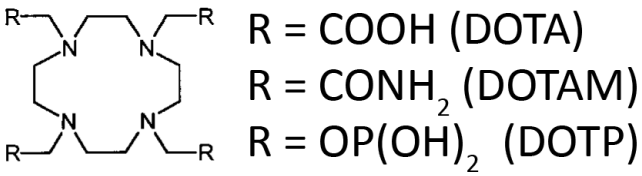

Fig. III.2 – General structure of a (tetrakis)-N-substituted cyclen molecule, with the most common substituents and acronyms listed.

The choice of formal charge of the Gd chelates (-5 and +3 for Gd-DOTP and Gd-DOTAM, respectively) reflects an attempt to increase specificity in binding to proteins. Weakly charged chelates, such as DOTA or DTPA (which are neutral or have charge = -1) revealed to be weak, non-specific binders that can thus induce a large range of small, averaged paramagnetic effects.

DOTP had been studied as a potential bone-targeting MRI and radiotherapy probe [30], as well as a pH and temperature sensor *in vivo* [31]. Both these probes should be

able to bind reversibly to proteins with an affinity in the same range as that of electron-transfer complexes (see Chapters II and IV). Therefore, we have chosen to test these probes in the study of the complex characterized in Chapter II: *D. gigas* rubredoxin and cytochrome c_3. As mentioned before, these proteins can be used as models for other FeS center or heme proteins, and present characteristics complementary to each another. While rubredoxin is essentially acidic at physiological pH (pI 4) with a hydrophobic patch in the vicinity of the metal center, the environment around the four heme groups of cytochrome c_3 can vary between negatively charged and positively charged, thus creating a range of different conditions to which the lanthanide probes might bind (Fig. III.3).

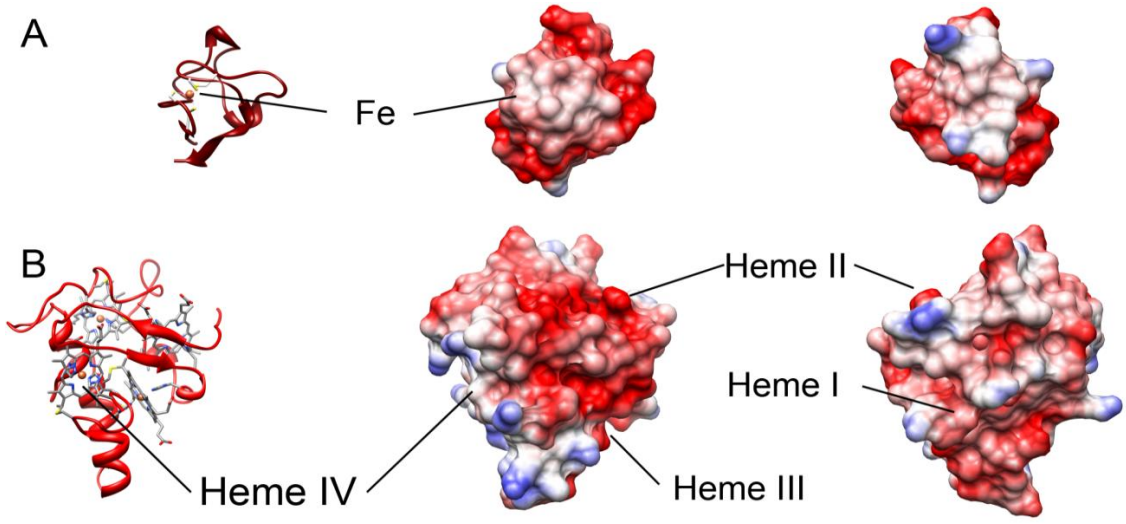

Figure III.3 – A) Left: Ribbon representation of *D. gigas* rubredoxin (PDB file 1RDG). Middle, right: Coulombic surface coloring of rubredoxin at 298 K, the right-hand side representing a 180 degree vertical axis rotation of the surface to its left. B) Left: Ribbon representation of *D. gigas* cytochrome c_3. Middle: Coulombic surface coloring at 298 K of cytochrome c_3 in the same orientation of the left hand-side panel. Right: 180 degree vertical axis rotation of the cytochrome c_3 surface to its left, to highlight the electrostatic environment around other heme groups. Blue: positively charged residues (most intense = +10 kcal mol^{-1}.e). Red: Negatively charged residues (most intense = -10 kcal mol^{-1}.e). White: Neutral residues. Images created with UCSF Chimera [32]. Coulombic charges calculated using the Amber force field ff99SB package for the aminoacid residues [33].

III.3 Materials and Methods

III.3.1 Protein isolation

D. gigas Zn substituted ^{15}N-rubredoxin and *D. gigas* cytochrome c_3 were isolated as previously described in Chapter II [34].

III.3.2 Preparation of Gd(III) probes

The macrocyclic ligands DOTAM and H_8DOTP and their Gd^{3+} complexes were synthesized according to published procedures [35-38] (these compounds were a kind gift from Prof. Carlos Geraldes' group at Universidade de Coimbra, Portugal).

III.3.3 ^{1}H NMR Experiments

Aliquots of either probe were added to a 150 μM solution of cytochrome c_3 in 10 mM Tris-HCl pH 7.6, and 10% D_2O. Spectra were acquired at 298 K in a Bruker AvanceIII 600 MHz spectrometer equipped with a TCI cryoprobe and a variable temperature control unit, and were analyzed using TOPSPIN 2.0 (Bruker). Water suppression was achieved by 180°-selective excitation-sculpting gradient pulses, using pulse sequence zgesgp. 256 transients were collected for each experiment in a 60 ppm spectral window with 16k sampling rate.

III.3.3 2D NMR Experiments

Aliquots of the same solutions described in section III.3.2 of either Gd-DOTAM or Gd-DOTP were added to a 75 μM solution of ^{15}N-Zn-rubredoxin in 10 mM Tris-HCl pH 7.6, and 10% D_2O until a ratio [Gd probe]/[rubredoxin] of 0.5 (Gd-DOTP) or 1.0 (Gd-DOTAM). After the Gd-DOTAM-rubredoxin titration reached a 1:4 ratio, aliquots of cytochrome c_3 were added until a final ratio of 1:4:4. Spectra were acquired at 298 K in a Bruker AvanceIII 600 MHz spectrometer equipped with a TCI cryoprobe, with pulse sequence Hsqcetfpf3gpsi2. Six transients were acquired for each step, with 2048 point sampling in the direct dimension (16 ppm spectral width) and 256 increments in the indirect dimension. Data was analyzed using TOPSPIN 2.0 and CARA 1.8.4 [39].

III.4 Results and Discussion

Lanthanide probes have been garnering for the past two decades the status of efficient relaxation agents in the field of human MRI. Recently, attention has turned to applications in the protein biochemistry field to characterize protein complexes or as a constraint source for three-dimensional structure calculation. This chapter aims to describe the effects and potential applications in protein complex characterization of two oppositely-charged Gd probes (Gd-DOTAM and Gd-DOTP), using two well characterized protein targets, rubredoxin and cytochrome c_3 (Chapter II).

III.4.1. Cytochrome c_3, a negatively charged protein with 4 heme groups

Cytochrome c_3 from *D. gigas*, which at the working pH exhibits amino acid residue patches either positively charged (mostly around heme IV, but also near heme III) or negatively charged (hemes I and II) (Fig. III.4) can be considered as a suitable protein model to assess the feasibility of using Gd-DOTAM or Gd-DOTP as protein interaction probes.

i) The negatively charged PRE probe Gd-DOTP

For these studies, Gd-DOTP was added to cytochrome c_3 and ^{1}H NMR spectroscopy was used to determine the PREs observed upon its binding. Analysis of the spectra in Fig. III.5 shows that there is a dramatic enhancement of line width broadening inheme IV methyl M2 resonance of cytochrome c_3, and to a lesser extent, of heme IV methyl M18 resonance, even at low ratios of lanthanide complex to protein. A similar effect on the line width of these two methyls had been observed in the interaction between cytochrome c_3 and Fe-rubredoxin (Chapter II). All other heme methyls remain virtually unchanged in terms of line broadening, though some start to exhibit small shifts (with heme III's M2 being the most striking example).

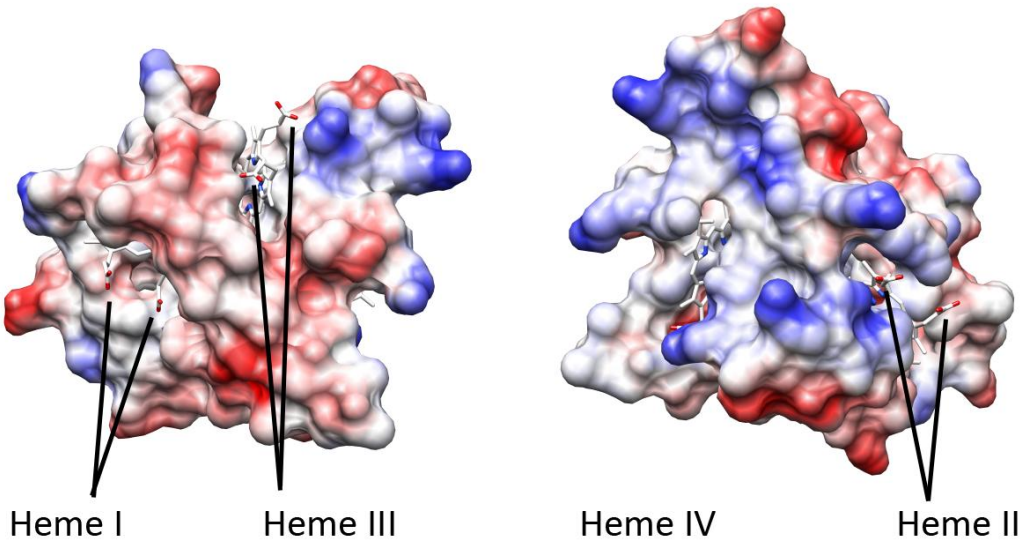

Figure III.4 – Electrostatic potential near the four different heme groups of *D. gigas* cytochrome c_3. Hemes I and III are surrounded mainly by negatively charged (red color) or neutral (white color) residues. On the other hand, hemes II and IV are surrounded by positively charged residues (blue color). Notice that heme IV does not have its propionate groups directly exposed to the solvent, unlike the remaining hemes. Images created with UCSF Chimera. Charges were calculated using the Force Field ff99SB package for the aminoacid residues [33].

The patch of positively charged lysines in the vicinity of heme IV enhances the probability of DOTP binding [19], which causes severe line width broadening of heme methyl resonances belonging to heme IV. The most solvent-exposed methyl groups (M2 and M18) appear to suffer a more pronounced effect than the other assigned methyl resonance of heme IV (M12), which is buried in the protein core. This effect becomes more pronounced as the titration progresses. Indeed, the most solvent exposed heme IV's methyl resonances become broadened beyond detection, while M12 experiences both linewidth broadening and chemical shift (Table IV.1).

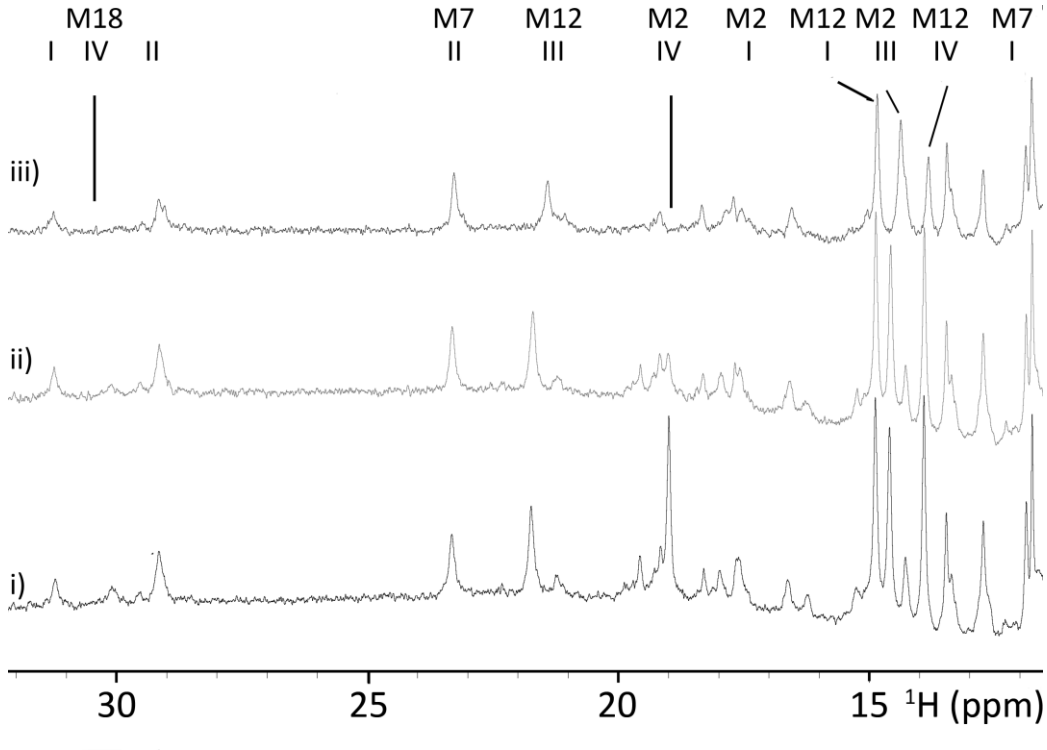

Figure III.5 – ^{1}H NMR spectra of the titration of Gd-DOTP to 150 μM cytochrome c_3. i) Cytochrome c_3; ii) cytochrome c_3 in the presence of 0.10 equivalents of Gd-DOTP; iii) cytochrome c_3 in the presence of 2.0 equivalents of Gd-DOTP. Spectra were acquired at 298 K in a Bruker Avance III 600 MHz spectrometer.

Several other methyls resonances belonging to other heme groups, but with special emphasis on heme III, also experience chemical shifts without significant broadening (Table IV.1 presents a comparison between the Gd-DOTP and Fe-rubredoxin titrations with cytochrome c_3). This might be due, as postulated before in Chapter II [34, 40], to small conformational rearrangements of the cytochrome molecule upon ligand binding, thus altering the chemical environment of the other heme groups. The lack of broadening excludes direct binding of the paramagnetic probe in the vicinity of the other heme groups. Moreover, the presence of Gd implies that these chemical shifts cannot be due to long-range pseudocontact shifts [2, 41].

Table III.1 – Comparison between the induced chemical shifts on cytochrome c_3 resonances induced by Fe-rubredoxin and Gd-DOTP.

		Chemical Shift Difference (ppm)	
		Fe-rubredoxin	**Gd-DOTP**
Heme I	M2	-0,12	-0,10
	M7	-0,02	-0,02
	M12	-0,04	-0,05
	M18	-0,01	-0,02
Heme II	M7	-0,09	-0,06
	M18	-0,04	-0,01
Heme III	M2	-0,13	-0,32
	M12	-0,18	-0,47
Heme IV	M2	0,21	---
	M12	-0,06	-0,12
	M18	-0,06	---

This, in turn, allows us to estimate a value for the dissociation constant, K_d (Fig. III.6). The estimated value of 20 μM is within the range for electrostatic-driven transient complexes [26, 42]. The fitting was performed assuming a binding model in which 1 Gd-DOTP binds to 2 cytochrome c_3.

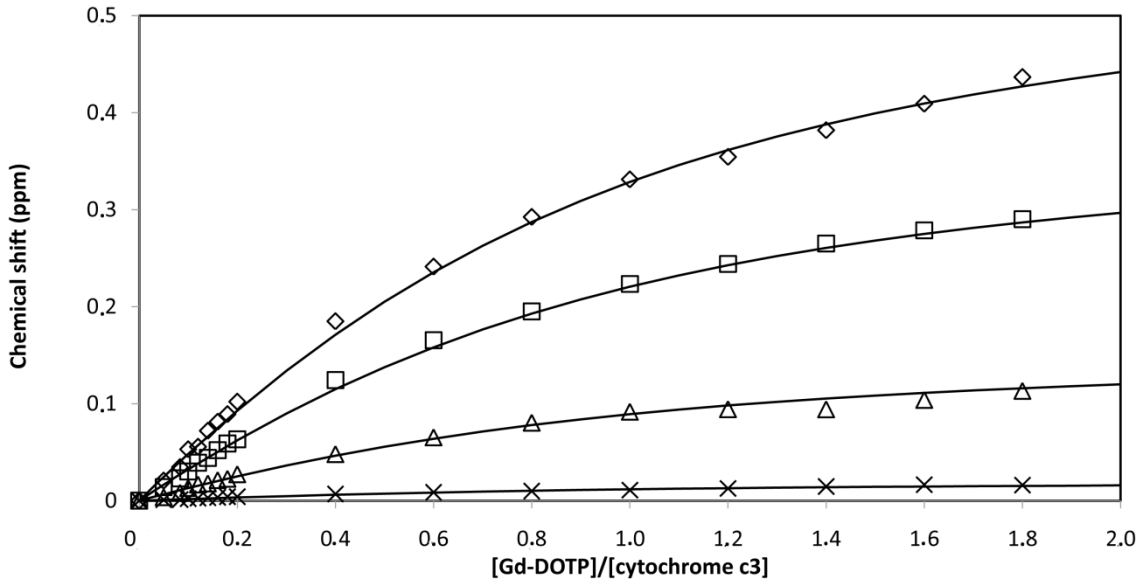

Figure III.6 - Chemical shift analysis of selected methyl resonances on the Gd-DOTP-cytochrome c_3 titration. ◊: Heme III M12; □: Heme III M2; Δ: Heme IV M12; X: Heme I M7. An average value of 20 μM was calculated for the K_d using Microsoft Excel and the formula described in Chapter II. In this case, for a best fit in the initial part of the titration, it was predicted that 0.5 Gd-DOTP molecules can bind one molecule of cytochrome c_3.

ii) The positively charged PRE probe, Gd-DOTAM

The addition of the positively charged probe, Gd-DOTAM, to cytochrome c_3, did not yielded significant effects on cytochrome c_3 heme methyl resonances (Fig. III.7): neither linewidth broadenings, nor chemical shifts due to conformational changes from probe binding appear in ^{1}H NMR titration spectra.

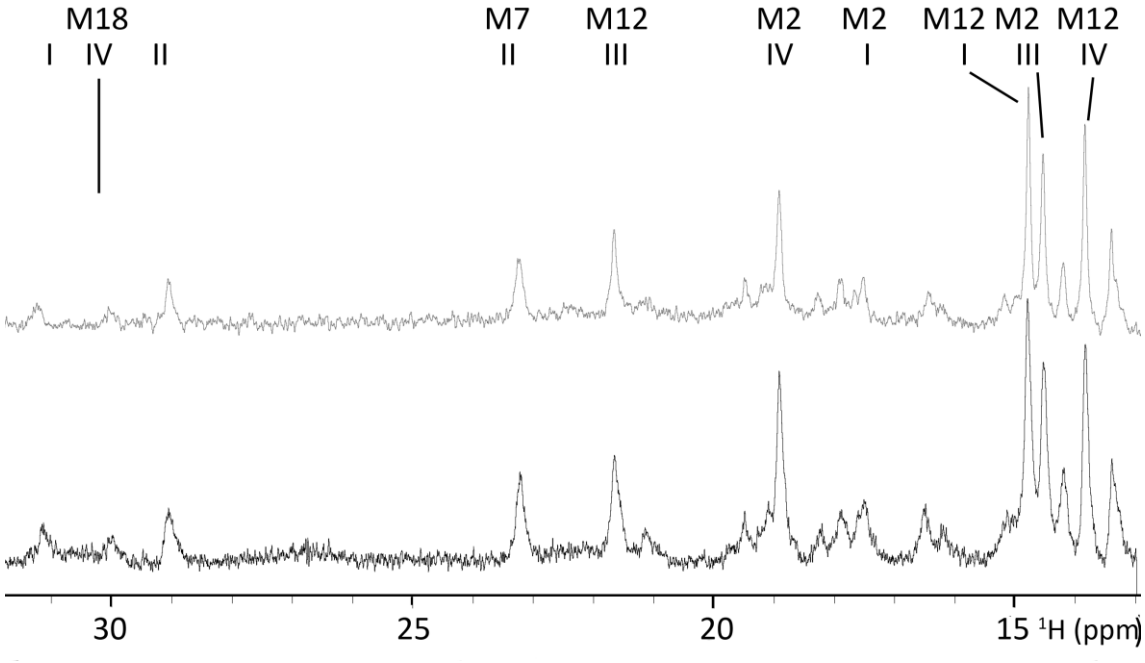

Figure III.7 – ^{1}H NMR titration of 150 μM cytochrome c_3 with Gd-DOTAM, at pH 7.6. Bottom (black line): cytochrome c_3 alone; top (grey line): cytochrome c_3 in the presence of 1.0 equivalents of Gd-DOTAM. Spectra were acquired at 298 K in a Bruker Avance III 600 MHz spectrometer.

Therefore, we conclude that there is no interaction between Gd-DOTAM and cytochrome c_3. This can be explained considering that the expected electrostatic

attractions exerted by the negatively-charged exposed propionate sidechains of the heme groups, other than heme IV, are being attenuated by unfavorable interactions with other positively-charged patches in their vicinity or steric hindrance imposed on the somewhat bulky chelate.

III.4.2 ^{15}N-Zn-rubredoxin, an acidic target protein

The effects of the two Gd probes on a small Fe-protein, rubredoxin, were also examined. Figure III.8 and III.9shows a relevant area of a [^{1}H, ^{15}N] HSQC spectrum of *Desulfovibrio gigas* ^{15}N-Zn-rubredoxin, with a significant part of the residues that belong to or are in the vicinity of the active center.

ii) The negatively charged PRE probe, Gd-DOTP

The addition of Gd-DOTP up to 2.0 equivalents induced no significant changes in either chemical shifts or linewidths of rubredoxin's resonances (Fig. III.8). This was expected due to the fact that this protein, at the working pH, is mainly negatively charged with a hydrophobic patch near the metal center. The results show that electrostatic repulsions with the negatively charged DOTP-coordinated Gd(III) ion avoid any significant interaction (Fig. III.8).

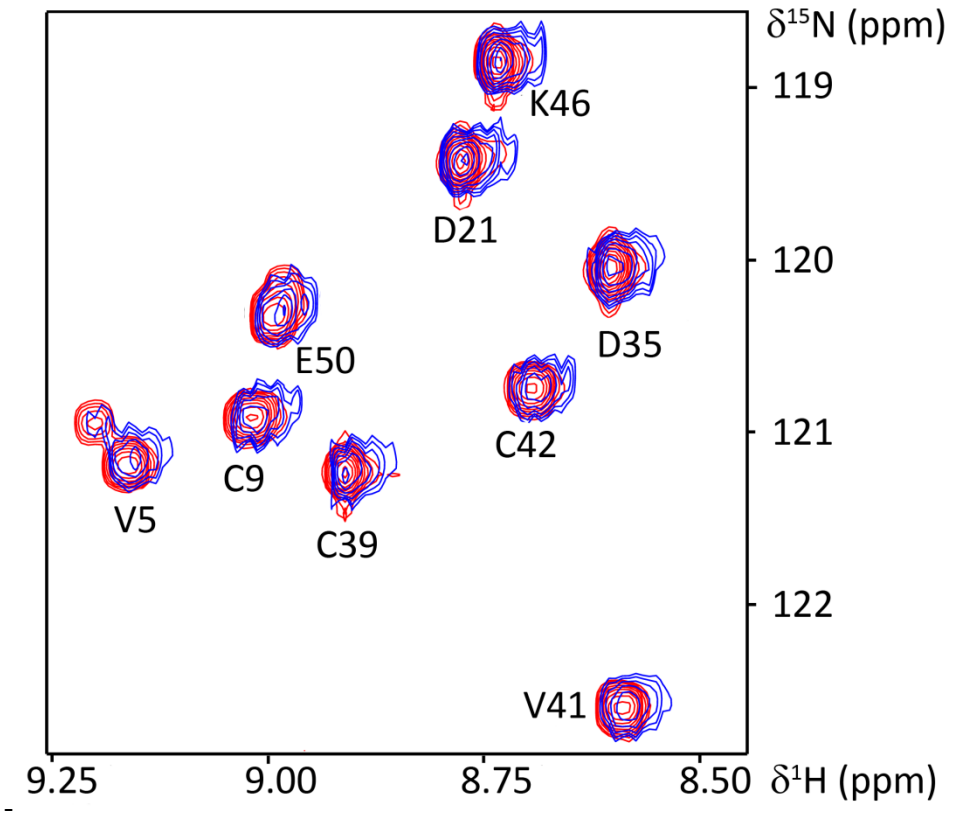

Figure III.8 – [^{1}H, ^{15}N] HSQC spectra of the titration of Gd-DOTP (negatively charged) with ^{15}N-Zn-rubredoxin. Legend: 75 μM rubredoxin (red); 200 μM Gd-DOTP and 50 μM rubredoxin (blue). Spectra were acquired in a Bruker Avance III 600 MHz spectrometer with a TCI cryoprobe.

ii) The positively charged PRE probe, Gd-DOTAM

Contrary to what was observed with Gd-DOTP, the interaction with Gd-DOTAM, resulted in significant spectral changes (Fig. III.9). It becomes clear from spectra analysis that the resonances near rubredoxin metal center become broadened, some beyond detection (Fig. III.9 illustrates some of these cases [C39, V41, C42], which will be analyzed in more detail subsequently). No significant chemical shifts are detected in this interaction.

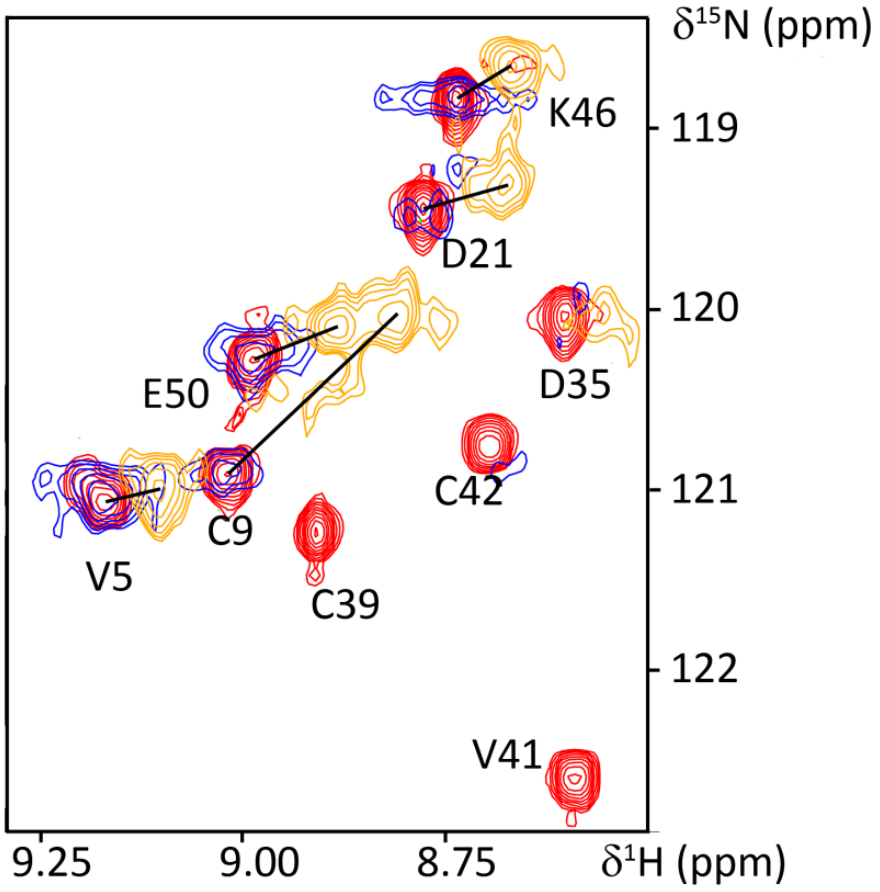

Figure III.9 – [^{1}H, ^{15}N] HSQC spectra of the titration between *D. gigas* ^{15}N-Zn-rubredoxin and Gd-DOTAM (positively charged). Legend: 75 μM rubredoxin (red); 200 μM Gd-DOTAM and 50 μM rubredoxin (blue); 125μM Gd-DOTAM, 31 μM rubredoxin and 125 μM cytochrome c_3 (orange). Spectra were acquired in a Bruker Avance III 600 MHz spectrometer with a TCI cryoprobe.

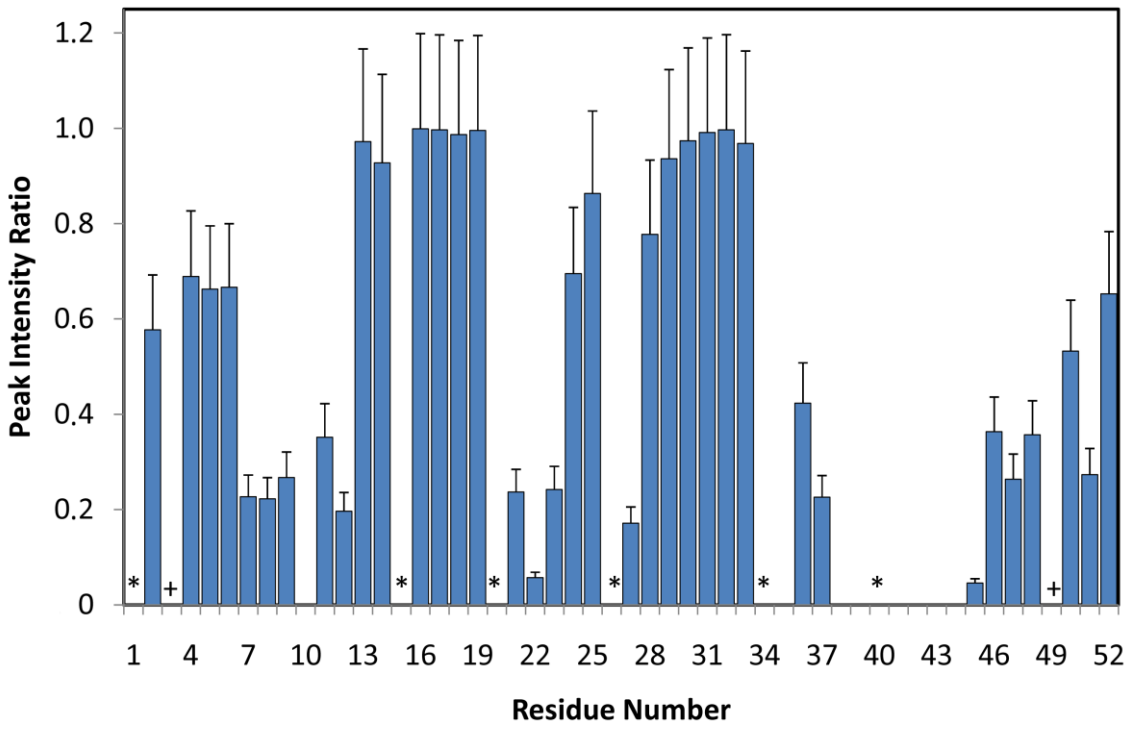

Figure III.10 – Peak intensity ratio of rubredoxin resonances, calculated by dividing the intensity of each resonance at the end of the titration by the peak intensity of rubredoxin alone. The bars indicate a comparison between free rubredoxin and 1:4 rubredoxin:Gd-DOTAM complex. Asterisks indicate proline residues and the first methionine residue. (+) - Resonances 3 and 49 are partly overlapped in all spectra, and cannot be deconvoluted. The intensities were corrected for dilution. Error bars were determined based on the signal to noise ratio.

The quantitative analysis in Figure III.10 shows that the most affected resonances by Gd-DOTAM are in the vicinity of rubredoxin metal center, as all residues between A38 and A44, as well as G10, are broadened beyond detection. Furthermore, residues in the immediate vicinity of these broadened resonances also suffer dramatic changes in peak intensity, with a decrease in 30% of its intensity: T7, V8, C9, Y11, E12, Y13, S45, K46, D47, and residues D21, S22 and G23 (Fig. III.10 and III.11).

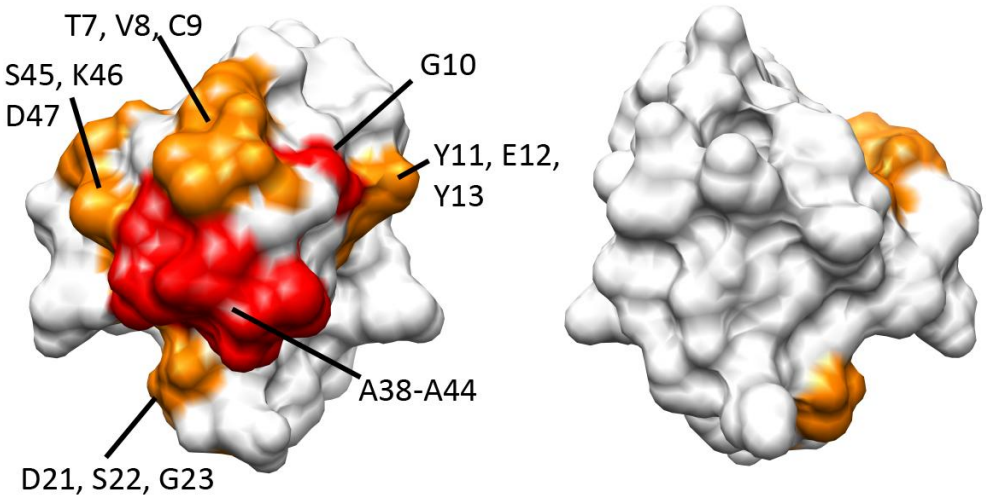

Figure III.11 – Mapping of the most broadened resonances on the surface of *D. gigas* rubredoxin by Gd-DOTAM. Red: residues which NH resonances were broadened beyond detection. Orange: residues which NH resonances were broadened to more than 30% of the original intensity. The surface on the right hand side represents a 180° vertical axis rotation of the surface on the left-hand side.

The decrease in intensity with increasing amounts of Gd-DOTAM is due to the fast electronic relaxation brought upon by the seven unpaired electrons of Gd, which can be felt at distances up to 15 Å [13]. Moreover, as expected for such an isotropic electronic environment, Gd-DOTAM does not induce any significant shifts on rubredoxin resonances, only line width broadenings, as observed by other authors [13].

The main aim of this work was to determine whether these Gd chelates could be used as relaxations probes to map and characterize the surface of protein complexes. In this case, the model complex was the one studied in Chapter II, rubredoxin – cytochrome c_3. Having this in mind, cytochrome c_3 was added to a solution containing Zn-rubredoxin : 4 Gd-DOTAM. The spectrum in Fig, III.9 (orange spectrum) shows that there are some resonances that become more intense and shifted from its initial position (Fig. III.9, compare orange with blue spectra).

Knowing that the relaxation effect is dependent on both the distance and concentration of the probe, and is characterized by line width broadenings that lead to a decrease in intensity of affected resonances, any probe displacement brought upon by cytochrome c_3 binding to rubredoxin at the same site or the shielding of those resonances due to the binding of hemic protein will be detected by the recovery of peak intensity (Figure III.12).

Therefore, the intensity ratio of rubredoxin resonances was analyzed and compared for these three cases: i) rubredoxin : 4 Gd-DOTAM, ii) rubredoxin : 2 cytochrome c_3 and iii) rubredoxin : 4 Gd-DOTAM: 4 cytochrome c_3 (Figure III.12).

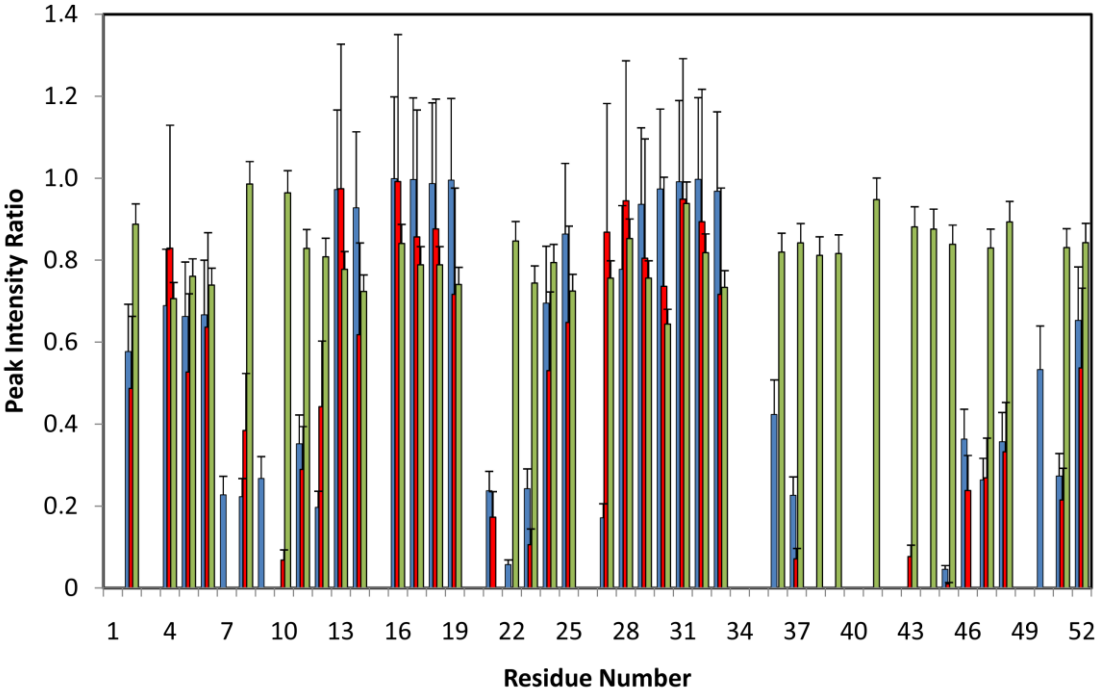

Figure III.12 – Peak intensity ratios, calculated in the same fashion of Fig. III.10. Legend: Blue columns – Rubredoxin : 4 Gd-DOTAM; Red columns – Rubredoxin:4 Gd-DOTAM: 4 cytochrome c_3; Green columns: Rubredoxin: 1.7 cytochrome c_3. All intensities have been corrected for dilution. Error bars were determined based on the signal to noise ratio.

In order to identify the resonances that are more affected the difference between the intensities of the resonances (rubredoxin:4 Gd-DOTAM:4 cytochrome c_3) and (rubredoxin:4 Gd-DOTAM) is displayed in Fig. III.13. This Figure indicates that

i) certain resonances become sharper (with increase intensity): C6, T7, V8, G10, Y11, E12, D21, G23, D36, W37, K46, D47 and A48;

ii) some just do not regain all the intensity that was lost due to the line width broadening imposed by Gd-DOTAM: S22, A38-S45;

iii) others show slight to moderate decreases in intensity (all other resonances).

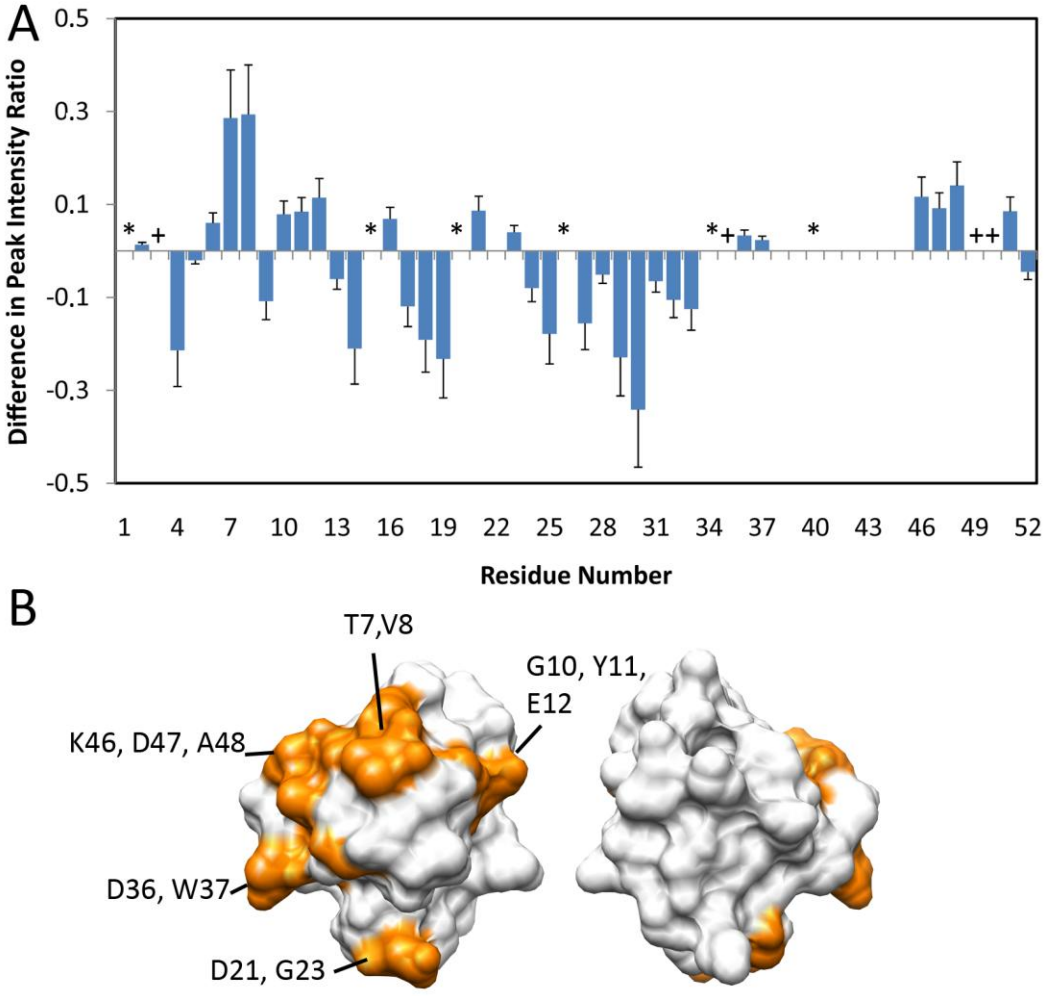

Figure III.13 A) – Difference in peak intensity ratio between rubredoxin: 4 Gd-DOTAM:8 cytochrome c_3 and rubredoxin: 4 Gd-DOTAM. B) Mapping on rubredoxin surface of residues which NH resonances increase intensity in the presence of 8 equivalents of cytochrome c_3. Asterisks indicate proline residues and the first methionine residue. Resonances 3 and 49, 9 and 50, and 35 and 42 are partly overlapped and cannot be deconvoluted (+).

The intensity recovery of some resonances near rubredoxin metal center could be attributed to the displacement of the paramagnetic Gd chelate due to the binding of cytochrome c_3 or to the shielding of these resonances from the effects of Gd chelate due to cytochrome c_3 binding, as proposed before.

Although the first hypothesis cannot be fully quantified, the analysis of Fig. III.14 shows that cytochrome c_3 is binding to rubredoxin near its metal center, occupying a similar surface as in the absence of Gd-DOTAM. Indeed, the chemical shift difference of the NH resonances that can be detected is of the same magnitude as reported before for rubredoxin-cytochrome c_3 complex (Fig. III.14, and Chapter II). The slight increases in chemical shift perturbation are probably due to the higher ratio of cytochrome used in this experiment (1:4 versus 1:1.7 in the titration between rubredoxin and cytochrome c_3 alone).

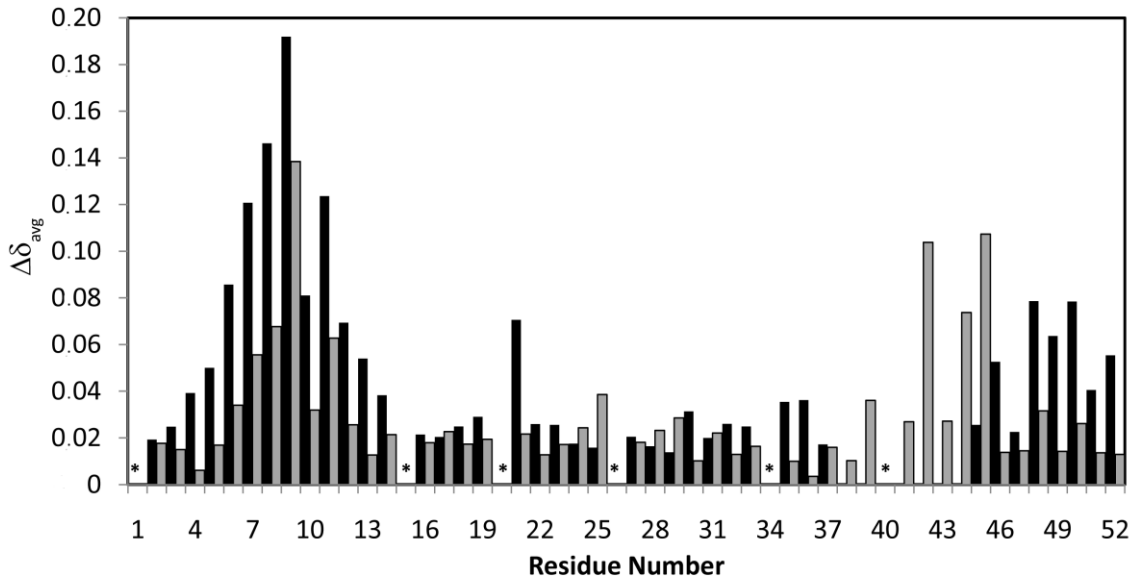

Figure III.14 – Garrett plot of the titration between cytochrome c_3 and rubredoxin (final ratio 1.7) (dark grey columns) and rubredoxin:4 Gd-DOTAM: 4 cytochrome c_3 (black columns).

As mentioned, some of the amide NH resonances do not recover intensity (A38 to A44), and were the ones which were more affected upon cytochrome c_3 (Fig. III.15). This fact can be explained considering that it might be possible that this probe is binding with slightly higher affinity to rubredoxin than cytochrome c_3, and also that its presence does not affect the binding of that cytochrome. Therefore, Gd-DOTAM and cytochrome c_3 could be binding simultaneously to rubredoxin.

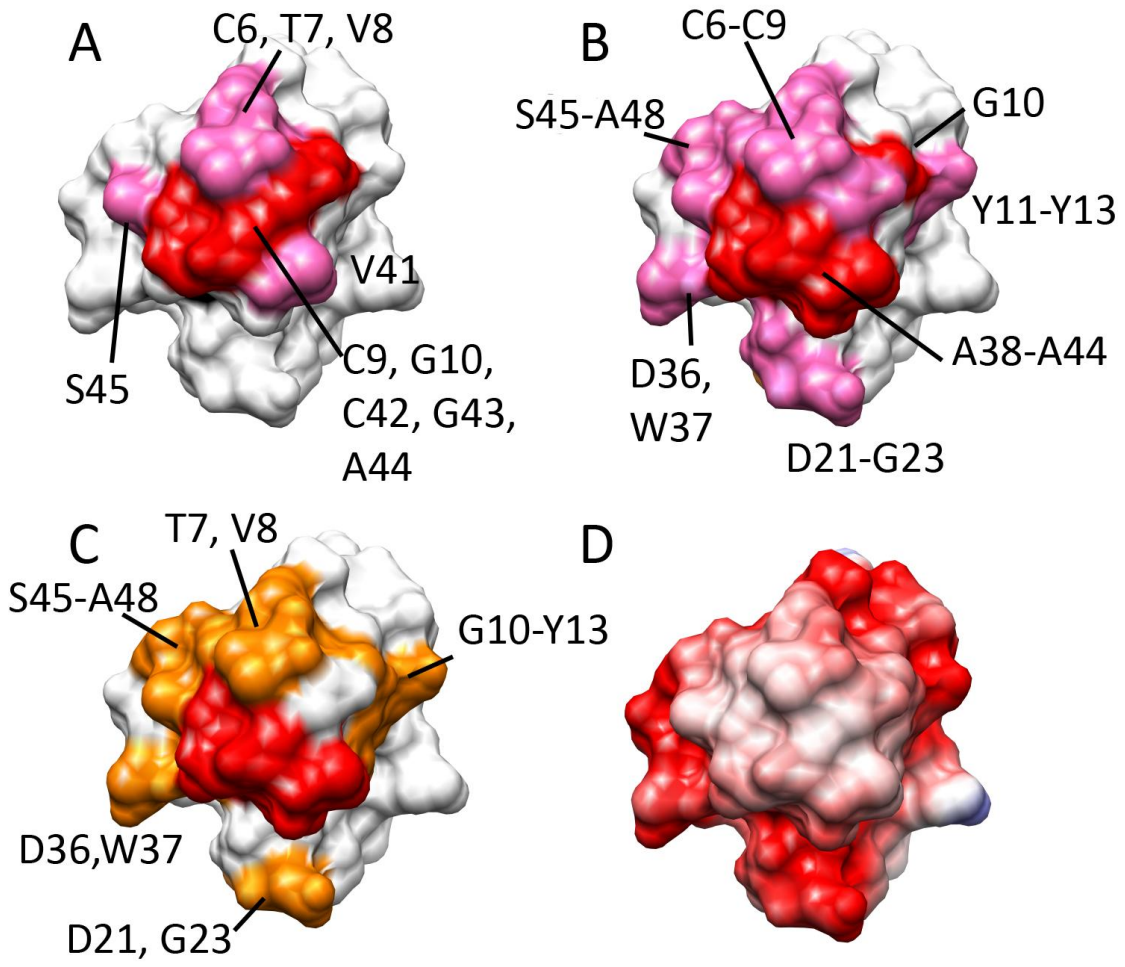

Figure III.15 – A) *D. gigas* Rubredoxin residues affected due to the binding of cytochrome c_3, in the absence of Gd-DOTAM (Chapter II, [34]). B) Mapping on rubredoxin surface of residues, whose NH resonances were most affected by the presence of Gd-DOTAM; red: NH broadened beyond detection; pink: NH broadened to below 30% of their initial intensity. ; C) B) Mapping on rubredoxin surface of residues which NH resonances increase intensity in the presence of 8 equivalents of cytochrome c_3 (orange color). Residues not detected are colored red. D) Coulombic surface of rubredoxin surface, calculated as described in Fig. III.3.

Indeed, analysis of heme methyl resonances shows a slight increase in linewidth broadenings of heme methyl resonances belonging to heme IV, upon binding to the rubredoxin-Gd-DOTAM complex (not shown), when compared to the methyl resonances of the other hemes. This can only be explained considering that heme IV methyl resonances are experiencing a paramagnetic effect due to the presence of the Gd chelate at a distance < 15 Å (since rubredoxin center has been substituted by Zn).

In order to better assess the binding mode of the Gd chelate to rubredoxin, as well as, the affinity of this interaction, more studies involving the determination of T2 relaxation times of rubredoxin amide resonances would have to be performed. This would provide a clearer picture of the change in dynamics upon addition of Gd-DOTAM.

III.5 Conclusions

1. [Gd-DOTP]$^{5-}$

As hypothesized the interaction between the negatively-charged lanthanide chelator with ^{15}N-Zn-rubredoxin is negligible. This was expected since rubredoxin is extremely acidic, at the experimental values of pH (7.6) and Gd-DOTP has also a negative net charge at this pH, thus electrostatic repulsions dominate and prevent the formation of any observable interaction.

However, the interaction with cytochrome c_3 results in severe line broadening of resonances belonging to heme IV at very early stages in the titration experiment (at ratio = 0.042, M2 and M18 resonances, which are the most exposed methyls, are barely distinguishable from the baseline); broadening still occurs in heme IV's other resonance (M12) in later stages. Chemical shifts of large magnitude occur mainly in the methyl groups of heme III in later stages of the titration, as had been seen also for the titration between cytochrome c_3 and Fe-rubredoxin (Chapter II). This might be due to conformational rearrangements, since Gd does not induce pseudo-contact shifts. A K_d was estimated based on four methyl group chemical shift difference progressions belonging to 3 different heme groups, with a value of 20 μM, which is in line with electrostatic-driven transient complexes. Thus, this probe can serve as a good cosolute reporter of interactions of heme proteins with positively-charged patches in its vicinity.

2. [Gd-DOTAM]$^{3+}$

For the positively charged, probe, the interaction with cytochrome c_3 is remarkably weak when compared to the chemical shift changes brought upon by Gd-DOTP. Moreover, no significant line width broadening occurs, which also reinforces the observation that there is no binding of Gd-loaded chelate to rubredoxin.

The interaction of Gd-DOTAM with ^{15}N-Zn-rubredoxin resulted in the broadening of selected resonances near the active center, in some cases to the point of no detection. Addition of cytochrome c_3 at a ratio of 1:8 shifted these changes partly: peak intensity

analysis revealed that cytochrome c_3 can partially displace Gd-DOTAM from binding to rubredoxin or shield some of its paramagnetic effects, since some of the most broadened resonances sharpen up upon cytochrome addition. Thus, these observations can aid in identifying the interaction surface between the hemic protein and rubredoxin.

The stronger magnetic moment of Gd is still being able to cause its PRE, even when a significant part has been substituted at the rubredoxin binding site by the cytochrome c_3. Concomitantly, the mode of interaction of the probe and cytochrome c_3 with rubredoxin should be slightly different, owing to the presence of hydrophobic patches in the surface of the proteins, which are notably absent in Gd-DOTAM. Calculation of a value for the K_d involving the most affected residues (in terms of line width broadening) is impossible to be completed due to lack of sufficient and reliable data points, requiring a more detailed analysis of T2 relaxation times of the involved residues.

In conclusion, the results obtained illustrate the use of Gd-DOTAM as a relaxation probe in the characterization of protein complexes.

Chapter IV – Superoxide reductase: different interaction modes with its two physiological electron donors.

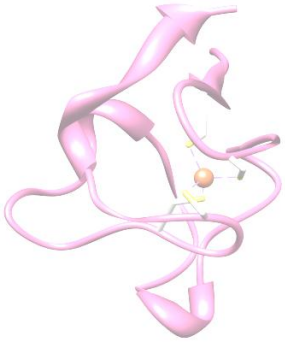

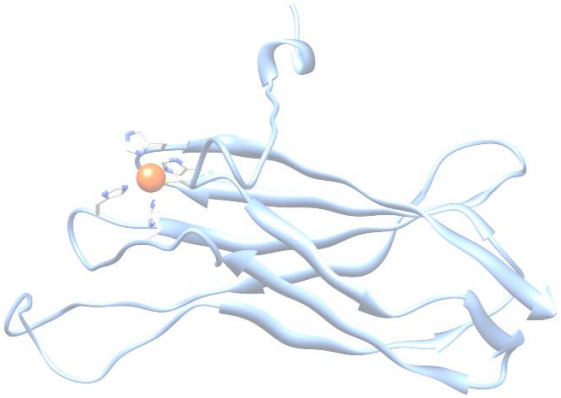

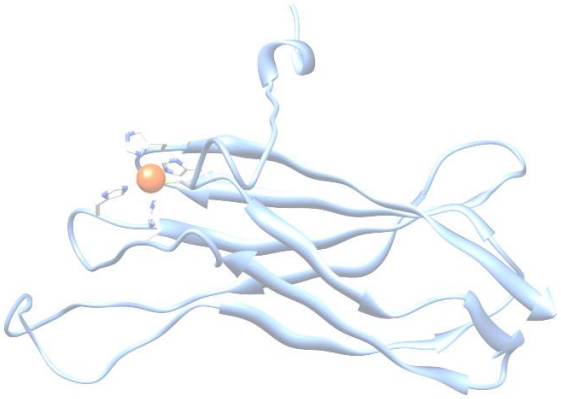

Chapter index

IV.1 Abstract

Anaerobic organisms have molecular systems to quickly detoxify reactive oxygen species when transiently exposed to oxygen. One of these systems is superoxide reductase, which is able to reduce $O_2^{\cdot -}$ to H_2O_2 without production of molecular oxygen. In *Desulfovibrio gigas,* this metalloenzyme is a Class II SOR, as it contains one Fe center coordinated to 4 histidinyl residues side chains and one cysteinyl sulphur. In order to complete the reaction, this enzyme requires an electron that is delivered either by rubredoxin or desulforedoxin. In this work, we have studied the interaction between *D. gigas* superoxide reductase and its electron donors using 2D NMR titrations and steady-state kinetic assays. The rubredoxin surface involved in the electron transfer complex with superoxide reductase comprises the solvent exposed hydrophobic residues in the vicinity of its metal center (C9, V10, C42, G43, A44), which are surrounded by a slightly acidic patch. The K_d for this interaction was estimated to be 3.0 ± 0.4 μM, at 50 mM ionic strength. An ionic strength dependence study on the activity was performed, showing maximum activity around 150 mM, with a k_{app} of 37 $\pm$ 12 min^{-1}. Although a complex between desulforedoxin and superoxide reductase could not be detected in a 2D NMR titration, possibly due to the very short half-life of the complex in the NMR time scale, this protein was shown to be able to transfer electrons to superoxide reductase, with a k_{app} = 31 $\pm$ 7 min^{-1} per monomer at an ionic strength of 50 mM. Kinetic assays and competition NMR experiments using Fe-desulforedoxin in the presence of Zn-rubredoxin, showed that these two electron donors must compete for the same site on the enzyme surface, with a calculated IC_{50} of 0.4 ± 0.2 μM and a K_d for the desulforedoxin-superoxide reductase complex of the same magnitude as the rubredoxin-superoxide reductase complex (2.5 μM).

IV.2 Introduction

As described in Chapter I, in order to deal with the toxic aspects of ROS, such as lipid oxidation, protein cleavage or DNA damage, among others, anaerobic organisms present biological systems that can detoxify these compounds that may become present when transiently exposed to aerobic environments. Some microorganisms from the *Desulfovibrio* genus are known to present both catalase and (SOD) [1] as a line of defense against ROS, and thus are able to survive for longer periods and actually produce ATP for a limited amount of time using O_2 as a terminal electron acceptor when transiently exposed to oxygen [2-4].

Prolonged exposure to oxygen, however, stops growth by inducing the degradation of metalloproteins involved in the respiratory pathway and down-regulating genes involved in energy metabolism [4]. As such, a disadvantage arises from the fact that dismutation of superoxide generates O_2, which is far from ideal for organisms with limited capabilities to deal with such a species.

To better cope with the transient presence of ROS, these organisms present a different system: superoxide reductase. This enzyme catalyzes the reduction of superoxide anion ($O_2^{\cdot-}$) to H_2O_2, using two protons and one electron per superoxide anion, and presents a clear advantage for these organisms relative to SODs, as it avoids the formation of O_2. Therefore, SOR, which is expressed constitutively in large amounts, contributes for the survival of these bacteria when exposed to mild or transient aerobic conditions [5, 6].

The Class II SOR from *D. gigas* is a 29 kDa homodimeric cytoplasmic metalloenzyme, also known as neelaredoxin [7]. It can directly reduce the radical anion superoxide to water using two electrons and two protons (as described in the Introduction). While the protons are readily available from the surroundings and from a nearby lysine sidechain-coordinated water molecule (section I.9.4), the electrons needed to re-reduce the Fe center for another catalytic cycle must come from an electron donor.

Several studies have been performed in order to identify the redox partners of SOR. In the case of *D. gigas*, it was proposed that both rubredoxin and desulforedoxin are competent electron donors to SOR [8]. Rubredoxin is a small (~6 kDa), monomeric, non-heme iron protein, that contains a tetrahedral FeS_4 metal center, that is very similar to the one of desulforedoxin and to center I of Class I SORs. This small protein is also capable of accepting

electrons from NADPH:rubredoxin oxidoreductase [9] and transferring them to the terminal oxidase of the oxygen detoxification pathway, rubredoxin:oxygen oxidoreductase, which enables *D. gigas* to produce ATP when transiently exposed to an aerobic environment [10, 11].

Desulforedoxin shares some characteristics with rubredoxin: it is a small (2 x 3.7 kDa), homodimeric, non-heme iron protein, containing a FeS_4 that differs from the one of rubredoxin in terms of the Fe coordinating sequence: while for rubredoxin the consensus sequence is ...C-$(X)_2$-C-G-$(X)_n$-C-$(X)_2$-C-G..., the one for desulforedoxin places the two C-terminal cysteine residues in adjacent positions, thus slightly distorting the tetrahedral geometry of its metal center [12, 13].

This chapter aims to characterize the electron transfer complex formed between the oxidized *D. gigas* SOR and Zn-substituted rubredoxin and desulforedoxin. One of the techniques employed was 2D NMR (HSQC) chemical shift perturbation mapping, as amide groups are sensitive probes for binding experiments: their chemical shift is highly dependent on hydrogen-bond formation or the polarity of its surroundings.

One problem might arise from the use of Fe-containing proteins in NMR experiments. High-spin Fe (S = 5/2 in the oxidized form, S = 2 in the reduced form), as described before in Chapter II, is a strong paramagnetic relaxation enhancer. The presence of 5 or 4 unpaired electrons, coupled to a strong anisotropy component of the magnetic susceptibility tensor, leads to strong PREs and PCSs in the resonances of the residues closest to the Fe centers. Indeed, ^{15}N-Fe-rubredoxin displays only a limited set of resonances when compared to its diamagnetic counterpart, ^{15}N-Zn-rubredoxin (Fig. II.2). The same effect is prevalent in desulforedoxin [14].

Zn-substituted forms of the proteins, which are diamagnetic, were used in order to avoid paramagnetic relaxation enhancements, that would hinder the detection of resonances near the metal center [14, 15]. Although these forms of the proteins are no longer competent to participate in electron transfer reactions, they have a similar structure to the native Fe-containing forms [14]. For a more detailed explanation of paramagnetic relaxation enhancements, please refer to section III.2 of this thesis.

Molecular docking simulations were also performed, using the BiGGER algorithm (Bimolecular Complex Generation with Global Evaluation and Ranking) [16], to complement this approach, and attain a structural model of the complexes.

A competition assay at the optimal ionic strength was performed using the Zn-substituted rubredoxin in the presence of desulforedoxin, to determine whether both partners can compete for the same site when transferring electrons to SOR.

IV.3 Materials and Methods

Unless otherwise stated, all reagents were of analytical grade or higher and purchased from Sigma-Aldrich, Fluka or Riedel-de-Häen.

IV.3.1 Protein Purification

IV.3.1.1 Purification of D. gigas rubredoxin and desulforedoxin

The purification procedures were performed at pH 7.6 (room temperature) and at 4°C using an ÄktaPrime Plus HPLC apparatus. The purification of Fe-rubredoxin and ^{15}N-Zn-substituted rubredoxin has been described in detail elsewhere [17]. An identical procedure was followed to obtain Fe-desulforedoxin and ^{15}N-Zn-substituted desulforedoxin. Protein concentration was determined using the published molar absorptivity coefficients [8] for Fe-rubredoxin, Fe-desulforedoxin and SOR, or the bicinchoninic acid method for the Zn proteins.

IV.3.1.2. Overexpression and purification of *D. gigas* superoxide reductase

Competent *E. coli* BL21(DE3) cells (Novagen, Madison, WI, USA) were transformed with the pDgNlrT7-7 plasmid encoding the gene for *D. gigas* SOR [18]. Cells were grown in Luria-Bertani medium at 37ºC with stirring until an OD_{600} ~0.8, at which overexpression of SOR was induced with 1 mM IPTG. Cells were further grown for 10-12 hours at room temperature, with reduced stirring to avoid the formation of foam.

Cells containing heterologously expressed SOR were harvested by centrifugation at 4100 *g* and resuspended in 10 mM Tris-HCl buffer at a 1 g/mL wet cell ratio. The cells were disrupted at 15000 psi using 30 mL French® Pressure cell press (Thermo Electron Corporation), and then ultracentrifuged at 138000 *g* for 60 minutes. The supernatant was then filtered and injected onto a DEAE-Sepharose Fast Flow anionic exchange resin (GE Biosciences), equilibrated with 10 mM Tris-HCl, pH 7.6. A linear gradient (0-500 mM NaCl) was applied and the SOR-containing fractions were concentrated in a Diaflo apparatus over an YM5 membrane (Millipore). This fraction was loaded onto a Superdex 75 column (GE Biosciences), equilibrated with 150 mM Tris-HCl buffer, pH 7.6, and fractions containing pure

SOR were combined. Throughout the purification procedure, the purity of the SOR fractions was assessed by SDS-PAGE.

IV.3.2 NMR Titrations

IV.3.2.1 Sample preparation

^{15}N-labeled protein samples and SOR had their buffer exchanged to 20 mM or 32 mM phosphate buffer pH 6.8 by injecting the concentrated samples onto a HiTrap™ Desalting column (GE Biosciences) previously equilibrated with the buffer. Samples were suitably concentrated using a Diaflo apparatus over a YM3 membrane (rubredoxin and desulforedoxin) or YM5 membrane (SOR). $^{2}H_2O$ was added up to a final concentration of 10% (V/V) to all samples. The final protein concentration was 0.4 mM of monomer for all protein samples used for the NMR experiments.

IV.3.2.2. 2D NMR Titrations

Aliquots of *D. gigas* SOR were added to a solution of ^{15}N-Zn-rubredoxin or ^{15}N-Zn-desulforedoxin until a ratio of [SOR]/[^{15}N-labeled protein] of 1.5. Spectra were acquired at 298 K on a Bruker Avance 800 MHz spectrometer equipped with a TXI Z-Grad cryo-probe, or in the case of the titrations with ^{15}N-Zn-desulforedoxin and the competition NMR experiment, on a Bruker Avance III Ultrashield 600 MHz spectrometer equipped with a CP TCI 600S3 H-C/N-D-05 Z cryo-probe. Due to the size of the complexes that are formed (ca. 41 kDa for rubredoxin-SOR, and 45 kDa for desulforedoxin-SOR), a [^{15}N, ^{1}H] TROSY-HSQC pulse program, optimized for protein assemblies larger than 30 kDa was used for data collection [19].

Spectra were processed using TOPSPIN 2.0 (Bruker) and analyzed with CARA 1.8.4 [20]. Changes in resonance positions, $\Delta\delta_{HN}$ (ppm), were calculated as a combination of the changes in the proton (ΔδH) and nitrogen (ΔδN) dimensions according to the following equation [21]: $\Delta\delta_{HN} = \sqrt{\frac{\left(\left[\frac{\Delta\delta N}{5}\right]^2 + [\Delta\delta H]^2\right)}{2}}$.

IV.3.3. Data analysis of binding.

The procedure employed in this work to determine the stoichiometry of binding and an apparent K_d has been described in Chapter II.

IV.3.4 Electron transfer kinetics studies

IV.3.4.1 Rate dependence on ionic strength

To establish the superoxide-mediated electron transfer rate dependence on ionic strength, kinetic studies were performed according to the previously described method [8], but changing the buffer system to 10 mM Tris-HCl pH 7.8. Kinetics absorbance spectra at either 494 nm or 504 nm for rubredoxin and desulforedoxin respectively, were collected on a Hewlett-Packard 8452-A diode-array spectrophotometer. Triplicate assays of the rates of electron transfer between SOR (100 nM of monomer concentration, oxidized with sodium hexachloroiridate) and either dithionite-reduced rubredoxin and desulforedoxin (10 μM of monomer, to be in saturating conditions) were acquired in the presence of xanthine/xanthine oxidase (500 mM and 0.060 U mL^{-1}, respectively), catalase (180 U to avoid end-product inhibition by H_2O_2) and EDTA (to avoid Fenton reactions by any free metals in solution) in 10 mM Tris-HCl pH 7.8. NaCl was added to obtain the following ionic strengths: 6.5, 31.5, 56.5, 106.5, 156.5, 206.5, 256.5, 306.5 and 506.5 mM. An auto-oxidation assay (i.e. without addition of enzyme) was also performed for each protein and taken into account when calculating superoxide-mediated electron-transfer rates, k_{app}. These values were calculated by fitting a line using the least-squares method to the initial part of the reoxidation curve, and plotted as a function of ionic strength based on the pseudo-first order equation: $v_0 = k_{app}[SOR]$, in which v_0 is the rate of re-oxidation of either rubredoxin or desulforedoxin, and being [SOR] constant in all the assays.

IV.3.4.2 Kinetic assays in the presence of Zn-Rubredoxin

In order to establish whether rubredoxin and desulforedoxin could compete for the same site when transferring electrons to SOR, a competition inhibition study was performed, in which aliquots of Zn-rubredoxin were added to a reaction vessel containing 10 μM Fe-desulforedoxin and 100 nM SOR at 56.5 mM ionic strength, up to a ratio of 10:1. The values of k_{app} were determined as previously described. A value for IC_{50} (half maximal inhibitory concentration) was estimated by non-linear regression using GraphPad Prism 5.0 (GraphPad Software, San Diego California USA, www.graphpad.com).

IV.3.5 Molecular docking studies

Docking algorithm BiGGER was used to establish possible geometries for the interaction between SOR and either rubredoxin or desulforedoxin.

By using the 3D structure of the interacting partners and searching the six dimensional space (rotation and translation in the 3 axes) of one protein (the probe) in relation to the other, that is considered fixed (the target), BiGGER ranks the possible calculated complexes according to several parameters, such as geometric complementarity, electrostatic energy minimization or accessible solvent area. The PDB files used in the molecular docking calculations were retrieved from the Protein Data Bank (www.rcsb.org/pdb) in the case of *D. gigas* rubredoxin (1RDG) and *D. gigas* desulforedoxin (1DXG). In the case of *D. gigas* SOR, a homology modelling-built PDB file was obtained using Swiss-Model [22], using the PDB file for *Thermotoga maritima* SOR, 2AMU, as a template, since these proteins share 54% sequence identity, the highest between *Desulfovibrio gigas* SOR and any class II SOR with a known structure deposited in the PDB (see below). As an empiric rule, 50% sequence identity results in an RMSD between template and homology structures of 1Å or less, hence *T. maritima* protein was considered suitable as a template. The docking algorithm assumed a pH of 7.0 for the calculations by default. Experimental results-driven restraints were used in the study of the rubredoxin-SOR complex, namely, the distance between the Fe ion of SOR and the HN couple of Cys9, Gly10, Cys42, Gly43 and Ala44 of rubredoxin. These restraints were obtained from the observation that the amide resonance of these residues display the

larger chemical shift differences or broaden beyond detection at latter stages in the 2D NMR titration (see Results). Since these effects are proportional to the reciprocal of the distance raised to the sixth power, the distance that was set for these restraints had a maximum of 7 Å, and the minimum contact area was set to 150 Å. In the case of desulforedoxin-SOR complex, the only restraint used was to set the distance between SOR Fe atom and one of desulforedoxin monomers to be smaller than 10 Å.

Putative complexes obtained by BiGGER were then ranked and evaluated in terms of additional criteria: electrostatic energy minimization, geometric complementarity, solvation energy and aminoacid side chain affinity. Selected top-ranked complexes that complied with the experimental data were further analyzed using PDBe PISA (Protein Interfaces, Surfaces and Assemblies) website, available at http://www.ebi.ac.uk/msd-srv/prot_int/pistart.html in order to characterize the interface of the structural model of the complexes: number of salt bridges and hydrogen bonds, properties of the interface (percentage of polar and non-polar residues, size), hydrophobicity and the gap volume index (as defined by Jones and Thornton [23]).

IV.4 Results and Discussion

IV.4.1 Electron transfer complex between rubredoxin and SOR

The ^{1}H-^{15}N HSQC spectrum of *D.gigas* Zn-rubredoxin, that had been previously assigned [24] (some of the residues were re-assigned during the present work by re-appreciation of some ^{1}H and ^{15}N resonance assignments, as well as the extension of the assignments to ^{13}C resonances), was used to identify the residues affected during a titration with *D. gigas* superoxide reductase. Figure IV.1 shows part of the ^{1}H-^{15}N TROSY-HSQC spectrum, which contains the HN amide resonances of the residues that are in the vicinity of the metal center of rubredoxin.

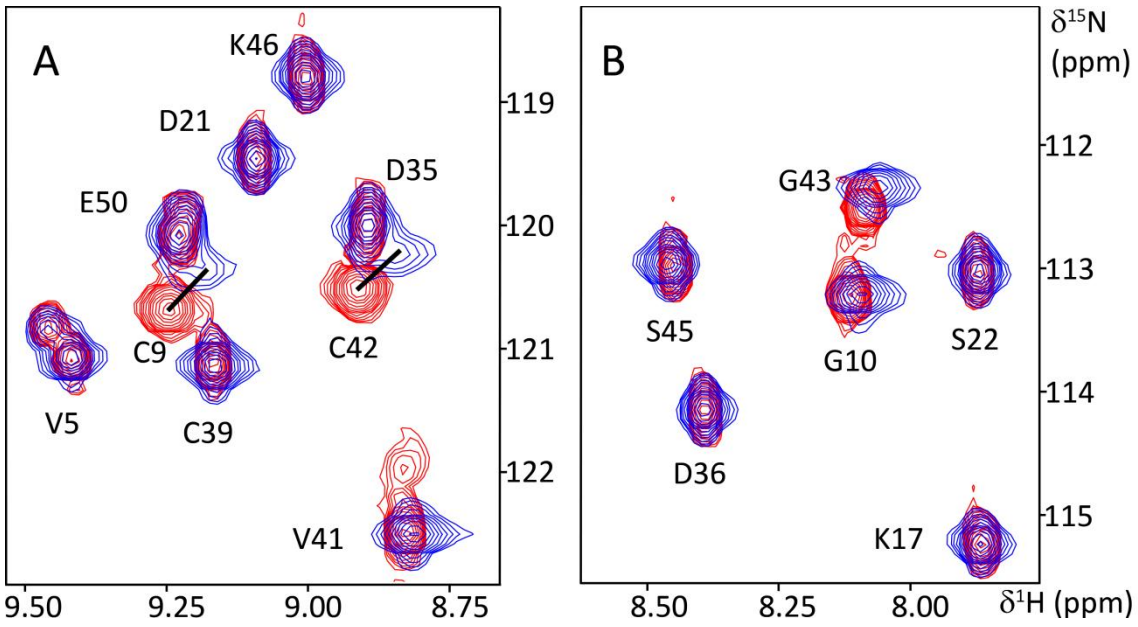

Figure IV.1 – Titration of Zn-rubredoxin (400 μM) with SOR monitored by [^{1}H, ^{15}N] TROSY-HSQC, in phosphate buffer pH 6.8 at 50 mM ionic strength. Spectra were acquired on a Bruker Avance800 spectrometer at 298 K. Red: ZnRd/SOR = 0; Blue: ZnRd/SOR = 1.0. Panels A and B represent insets of the full spectra, highlighting selected resonances that belong to or are in the vicinity of the metal center of rubredoxin.

Upon addition of *D. gigas* SOR to Zn-rubredoxin, the HN resonances of residues located near the metal center exhibited significant chemical shifts (Figure 1A and B). The magnitude of the shifts (Figure 2A) is consistent with the residues affected due to complex formation, as they are the most solvent exposed (Figure 2B). Moreover, the HN resonances of Cys9 and Cys42, became broadened almost to the point of no detection at a Zn-Rb:SOR ratio of 1.5 (not shown). The line broadening of these resonances can be attributed to a paramagnetic relaxation enhancement, and not to the slower tumbling of rubredoxin, due to complex formation, as this effect is specifically observed only on those resonances. This effect can be explained by the presence of the paramagnetic center of SOR (high spin Fe^{3+}, S = 5/2) in close proximity of these residues, as it is known that high-spin Fe^{3+} can induce PREs on proton resonances located at a 5 Å distance from the iron ion (on a 100 MHz spectrometer, line width broadenings at this distance range from 120 to 1200 Hz) [25].

The 2D NMR titration was performed at two ionic strengths, 32 mM and 50 mM, and no differences were observed in the chemical shift variation and residues affected due to the binding (Figure IV.1 and IV.2A and C). An apparent K_d of 3 μM was estimated for the Rd-SOR complex from the chemical shift difference data, at both ionic strengths (Figure IV.2B), and this data shows that the complex has a stoichiometry of 1:1.

A similar K_d has been estimated by NMR for a number of other ET complexes [26]. However, it is important to point out that the K_d estimated using a NMR titration is not an accurate value but simply the upper limit value due to the high protein concentration used in these experiments.

IV.4.1.1 Docking simulations

Docking simulations were performed using the docking algorithm BiGGER, a rigid (soft) docking algorithm that allows the use of experimentally-driven restraints, such as NMR upper-distance restraints.

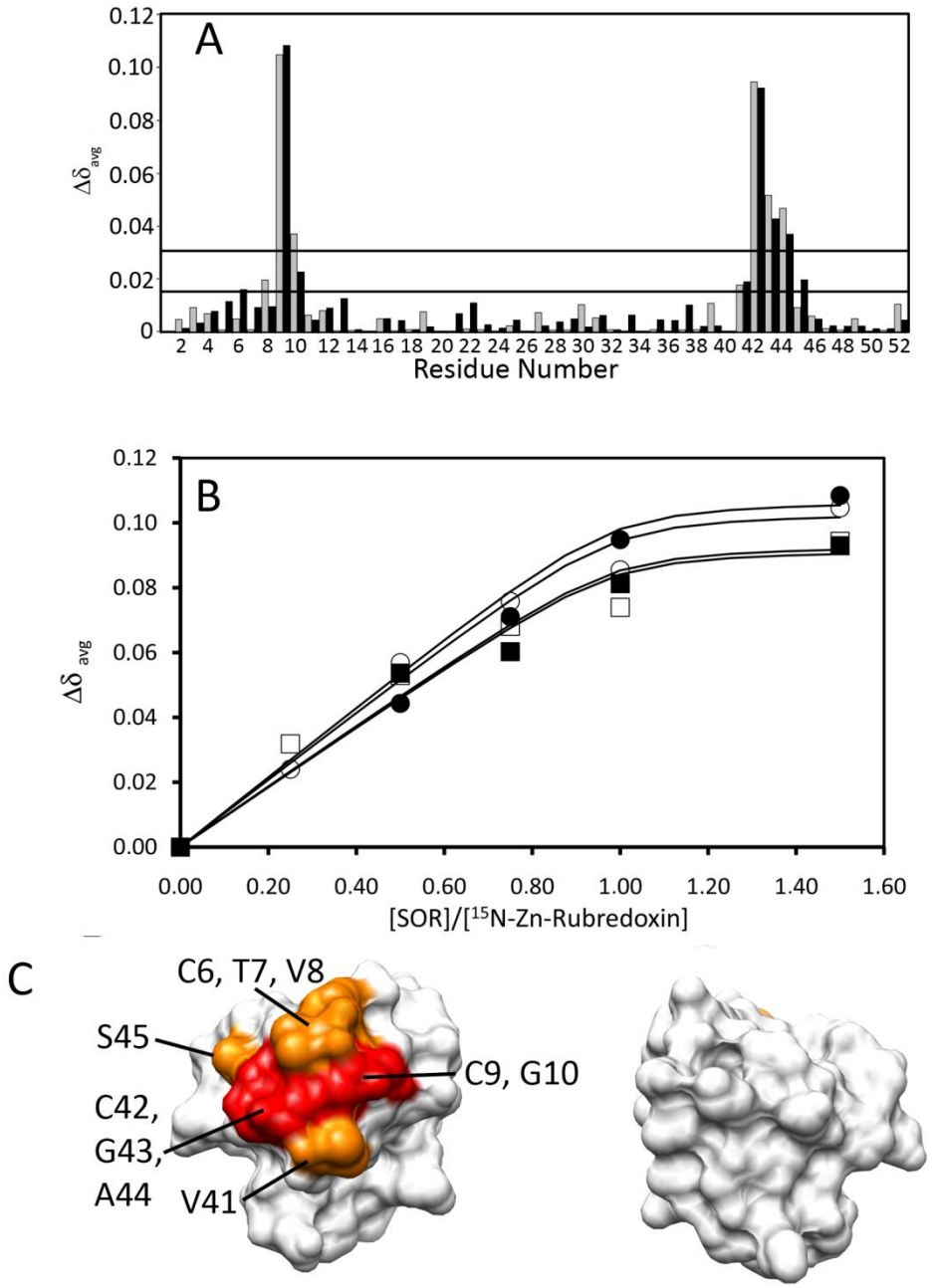

Figure IV.2 – A) Chemical shift variation of Zn-rubredoxin resonances upon SOR binding, at I = 32 mM (grey bars) and I = 50 mM (black bars), as described in Section IV.3. Asterisks correspond to methionine 1, and to the 5 proline residues. B) Estimation of the K_d for the binding of SOR to Zn-rubredoxin. The residues presenting the biggest chemical shift variation were used in this calculation, C9 (closed circles I=32mM, open circles I=50 mM) and C42 (closed squares I=32 mM, open squares I=50 mM). The data was fitted by adjusting the same K_d value to all data sets simultaneously and considering a 1:1 model. The K_d was estimated to be 3.0 ± 0.4 μM. C) Surface mapping of the most affected rubredoxin residues upon complex formation. The structure on the left represents a "head on" view of the metal center, while the structure on the right-hand side represents a 180º rotation on the vertical axis. Black: $\Delta\delta$ > 0.03 ppm. Grey: 0.03 ppm > $\Delta\delta$ > 0.015 ppm. White: 0.015 ppm > $\Delta\delta$. Molecular graphics images were produced using UCSF Chimera [27].

Therefore, a restrained-docking approach was used to predict a model structure of the complex between rubredoxin and SOR, using the experimental data derived from the NMR titration, which indicated that the NH groups of C9, G10, C42, G43 and A44 should not be located at a distance larger than 7 Å from the Fe ion of SOR.

The protein coordinates used in the docking calculations for rubredoxin was the one deposited in the Protein Data Bank, but in the case of *D. gigas* SOR a homology model was built. This methodology had to be used, as the structure of this enzyme has not yet been obtained either by X-ray crystallography or NMR spectroscopy. Indeed, crystals of *D. gigas* SOR were shown not to diffract at enough resolution for its structure to be determined (unpublished work of the collaborative project with the group of Prof. Maria João Romão).

Attempts to determine the solution structure by NMR spectroscopy were also made. However, this protein is a dimer which resulted in poor quality spectra that hampered the pursuance of structure determination by solution NMR (Fig. IV.3). Protein aggregation in tube was also a hypothesis not to be excluded when analyzing the obtained 2D NMR spectra.

Thus, a viable alternative to obtain a structure for the *D. gigas* protein was presented by means of homology modelling [22].

IV.4.1.1.1 Homology modelling of *D. gigas* SOR

Homology modelling is a useful technique to obtain a valid three-dimensional structure of a protein whose aminoacid sequence is known, but the structure, for a myriad of reasons, is not. Since sequence similarity usually confers homologous proteins structural similarity, one can easily construct a model for the protein of interest based on a suitable template. Thus, the first step in building a *D. gigas* SOR model consisted in finding a suitable template. The Protein Data Bank currently (as of September 2010) hosts the structures of three Class II SORs: isolated from *P. furiosus, P. horikoshii* and *T. maritima* (PDB files 1DQI, 2HVB and 2AMU, respectively). In common with the *D. gigas* protein, all have a Fe center coordinated by 4 histidine sidechain nitrogen atoms, and a cysteine sulphur.

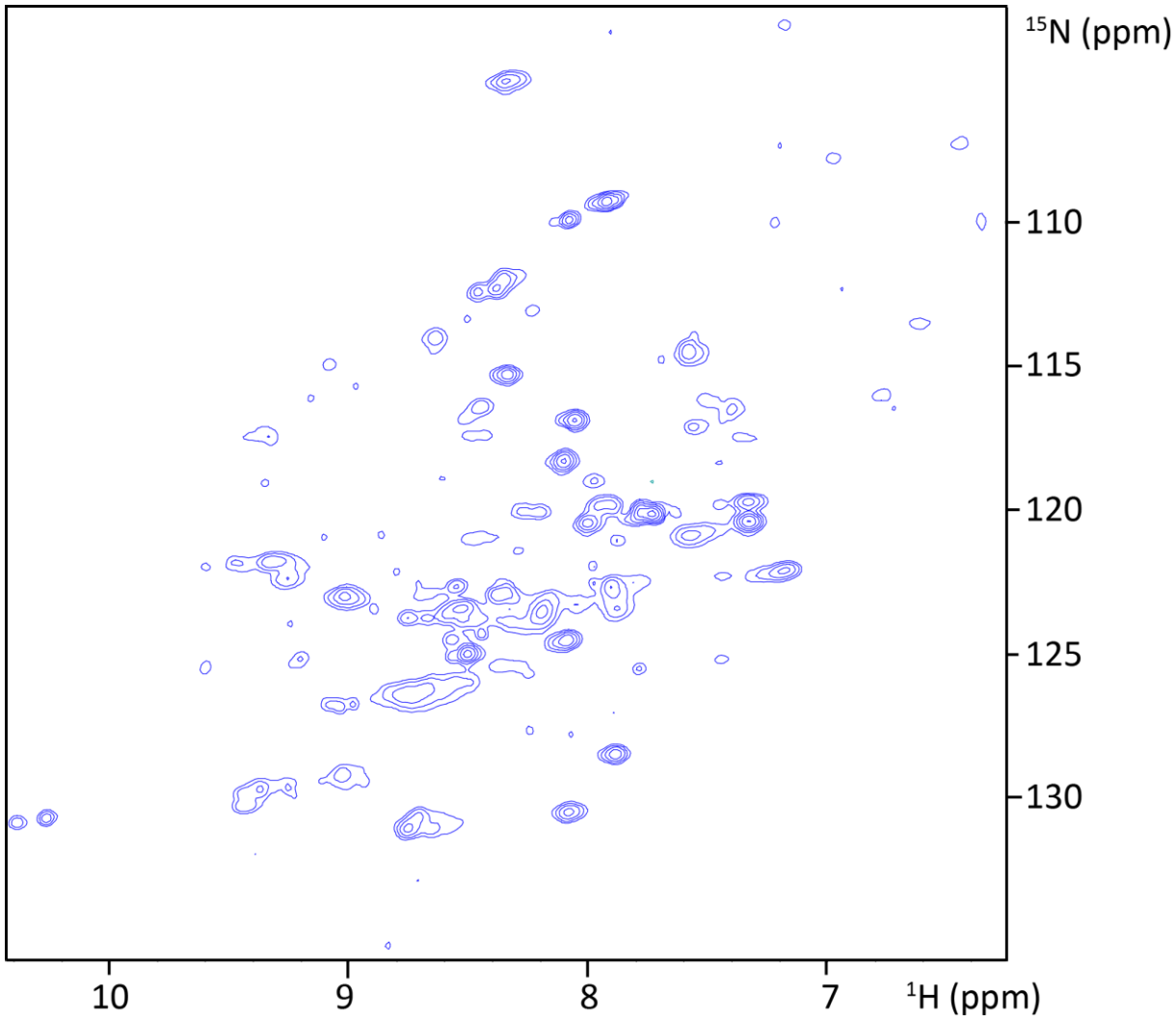

Figure IV.3 – Typical ^{1}H-^{15}N HSQC spectrum of *D. gigas* superoxide reductase in solution, at a concentration of 300 μM.

The overall fold of these proteins is similar: a small N-terminal helix turn is followed by eight beta-sheet strands and a few loops. The Root Mean Square Deviation (RMSD) between these three structures is 1.96 Å (Fig. IV.4)

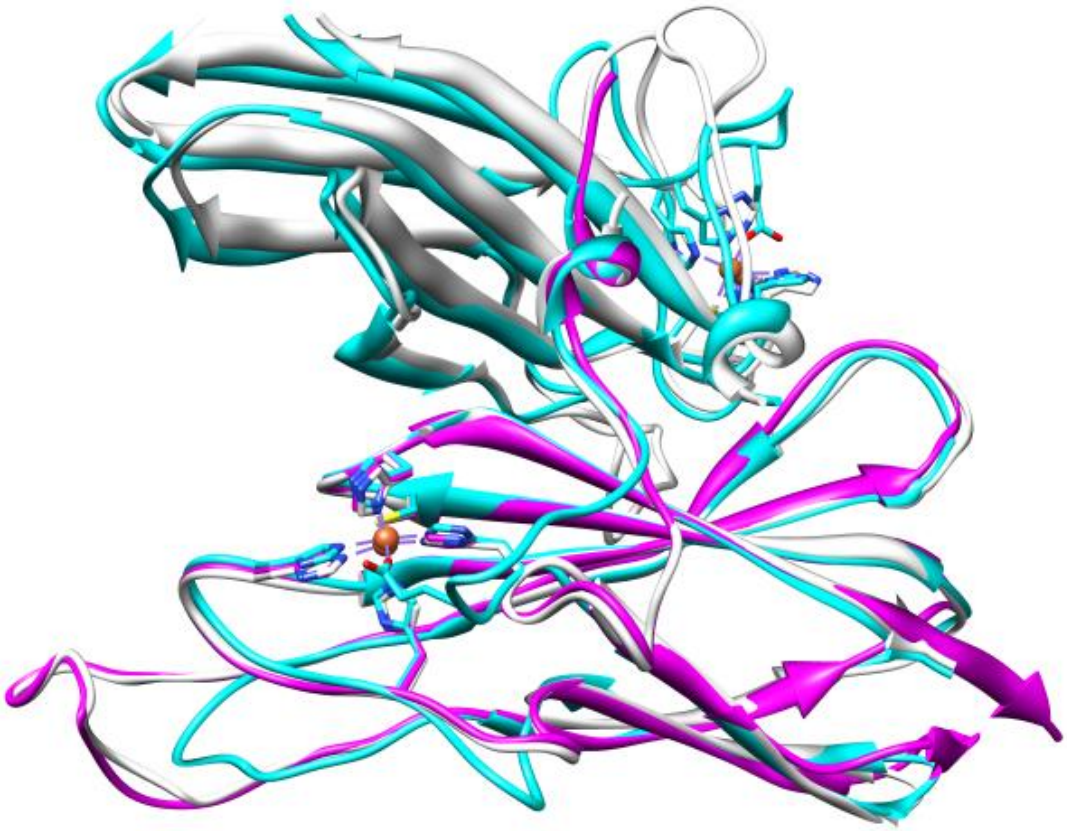

Figure IV.4 – Superimposition of the three available class II SOR structures, depicted as ribbons. Purple: *T. maritima*; Light blue: *P. horikoshii*. White: *P. furiosus*. The overall orientation of the beta-sheets and the metal-binding loops are kept. RMSD = 1.8 Å.

```
P.furiosus          ---------MISETIRSGDWKGEKHVPVIEYE---REGELVKVKVQVGKEIPHPNTTEHH 48
P.horikoshii        MHHKAKVIGMLKETIRSGDWKGEKHVPVIEYE---REGDLVKVEVSVGKEIPHPNTPEHH 57
D.gigas             --------MKMCDMFQTADWKTEKHVPAIECDDAVAADAFFPVTVSLGKEIAHPNTTEHH 52
T.maritima          --------MKLSDFIKTEDFKKEKHVPVIEAPEKVKKDEKVQIVVTVGKEIPHPNTTEHH 52
                             : : ::: *:* *****.**       .  . : * :****.****.***

P.furiosus          IRYIELYFLPEGENFVYQVGRVEFTAHGESVNGPNTSDVYTEPIAYFVLKTKKKGKLYAL 108
P.horikoshii        IAWIELYFHPEGGQFPILVGRVEFTNH---------SDPLTEPRAVFFFKTSKKGKLYAL 108
D.gigas             IRWIRCYFKPEGDKFSYEVGSFEFTAHGECAKGPNEGPVYTNHTVTFQLKIKTPGVLVAS 112
T.maritima          IRWIKVFFQPDGDPYVYEVGRYEFNAHGESVQGPNIGAVYTEPTVTTVVKLNRSGTIIAL 112
                    * :*. :* *:*  :   **  **. *         .   *:  .   .* .  * : *

P.furiosus          SYCNIHGLWEN--EVTLE- 124
P.horikoshii        SYCNIHGLWEN--EVQLE- 124
D.gigas             SFCNIHGLWESSKAVALK- 130
T.maritima          SYCNIHGLWESSQKITVEE 131
                    *:********.   : ::
```

Figure IV.5 – Sequence comparison between the class II SORs with published three-dimensional structure, and the *D. gigas* SOR. The conserved metal binding residues are highlighted by rectangles. Asterisks: Conserved residues. Dots: Semi-conserved residues (similar geometry and chemistry). Semi-colons: Semi-conserved residues (similar chemistry).

In order to choose the best possible template for the generation of the *D. gigas* SOR model structure, the sequence identity between all possible proteins was compared (Fig. IV.5). The results are summarized in Table IV.1.

Table IV.1 –Sequence identity and similarity percentages between *D. gigas* SOR and the remaining Class II SORs.

Class II SOR	Identity (%)	Similarity (%)
T.maritima	53.4	71
P. furiosus	51.5	61.5
P. horikoshii	42.4	51.8

As an empirical rule, it is considered that a 50% identity between two sequences will lead to a RMSD of the corresponding three-dimensional structures of ~1Å. Therefore, the most suitable candidate for a template is the one with the higher value of sequence identity and similarity – hence, the protein from *T. maritima* was chosen. A comparison between the *D. gigas* SOR model structure and the *T. maritima* was performed using PDBSUM [28]. Results are summarized in Fig. IV.6.

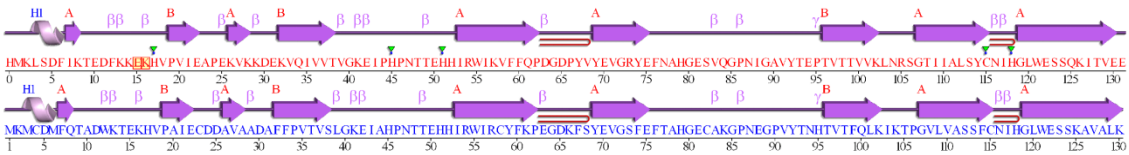

Figure IV.6 – PDBSUM analysis of the features of the three-dimensional folds of the SORs of *T. maritima* (top) and the *D. gigas* model (bottom). Purple arrows: beta sheets. Pink helix: alpha-helix motif. Hairpin: beta-hairpin motif. Green inverted triangles: active site residues.

Analysis of Figure IV.6 reveals that all the structural characteristics of the *T. maritima* protein are conserved in the obtained *D. gigas* model, thus in good agreement with what would be expected for sequences with a high degree of identity.

IV. 4.1.1.2 Molecular docking simulations using BiGGER

The electrostatic surface of the proteins involved in the docking experiments was analyzed using the AMBER force field approach (Fig. IV.7). This figure clearly shows that both iron-sulfur center ET proteins present a negatively charged patch near their active center (red color), whereas the area surrounding SOR's active site is mostly surrounded by positively charged or neutral residue sidechains.

WHISCY (What Information does Surface Conservation Yield) [29], an online software that predicts protein-protein interfaces based on residue conservation, was used to predict which *D. gigas* SOR surface residues have the highest probability to be involved in complex formation. For that, the aminoacid sequences of the Class II SORs with three-dimensional structure available (*P. furiosus, P. horikoshii, T. maritima*) were aligned with the *D. gigas* SOR sequence using ClustalW. The sequence alignment was then submitted to WHISCY, which predicted the most probable binding spots (Fig. IV.8).

WHISCY predicted that the most probable interaction area in *D. gigas* SOR consists of H51 and I117 (in red), and surrounding residues (in orange). H51 is one of the Fe-coordinating residues, while I117 is flanked by C115 and H118, two other residues present in the metal-binding motif.

The proteins under study exhibit the classical features for the formation of ET complexes: surface charge complementarity in the residues surrounding the metal centers to accelerate the formation of encounter complexes and pre-orientate the proteins in order to form an effective ET complex, reducing the dimensionality of diffusional search, and an uncharged patch around the metal centers that enables electrons to be efficiently transferred.

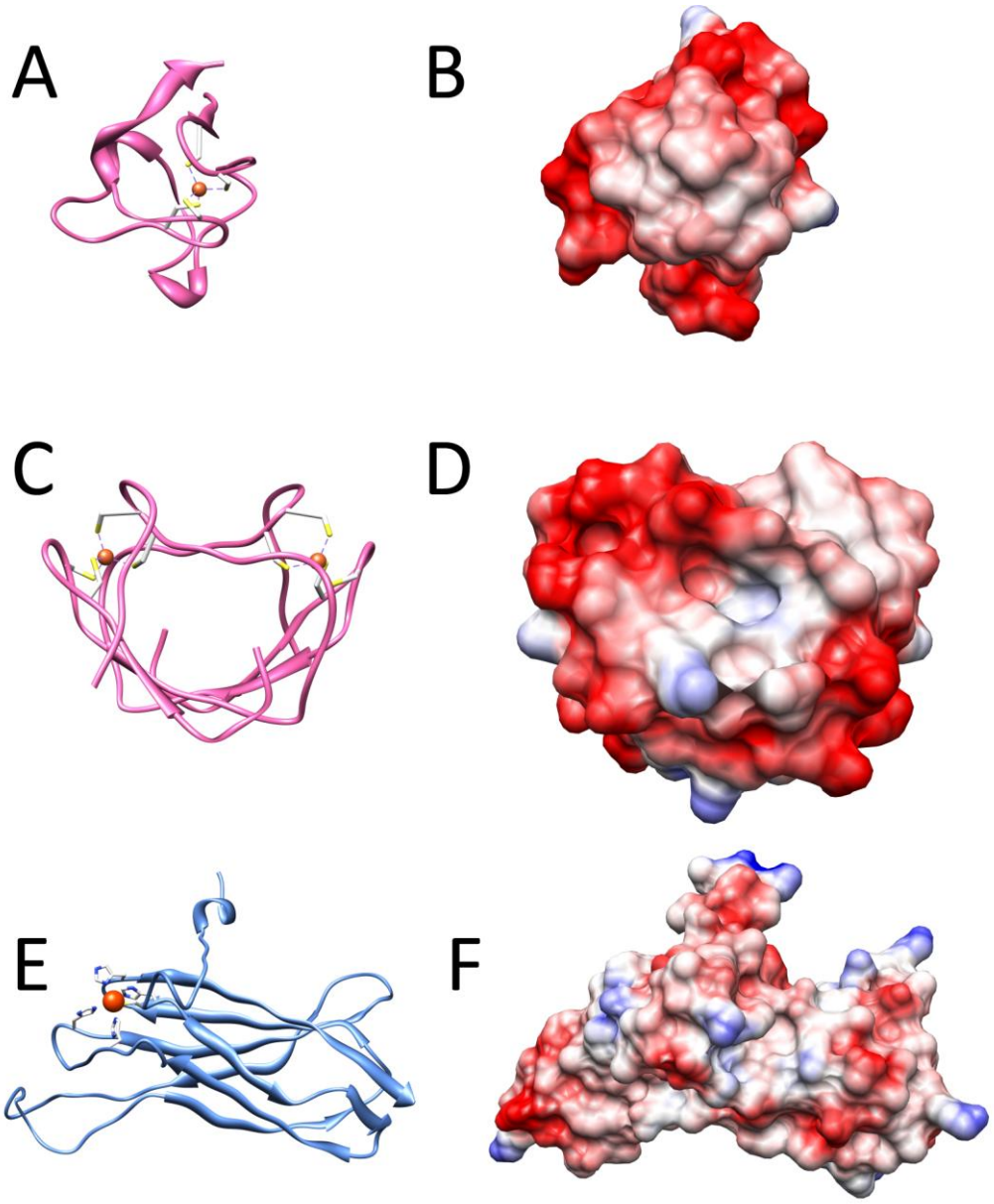

Figure IV.7 - 3D representations of: A, B) rubredoxin (PDB file 1RDG); C,D) desulforedoxin (PDB file 1DXG); and E,F) SOR model constructed by homology modeling from PDB file 2AMU using SwissProt. On the right hand-side column, the Coulombic charge surface of each protein is represented (red = negative charge, blue = positive charge, calculated with a ε = 4r and ± 10 kcal/mol thresholds. Charges were calculated using the AMBER force field ff99SB package for the aminoacid residues [30] integrated in UCSF Chimera.

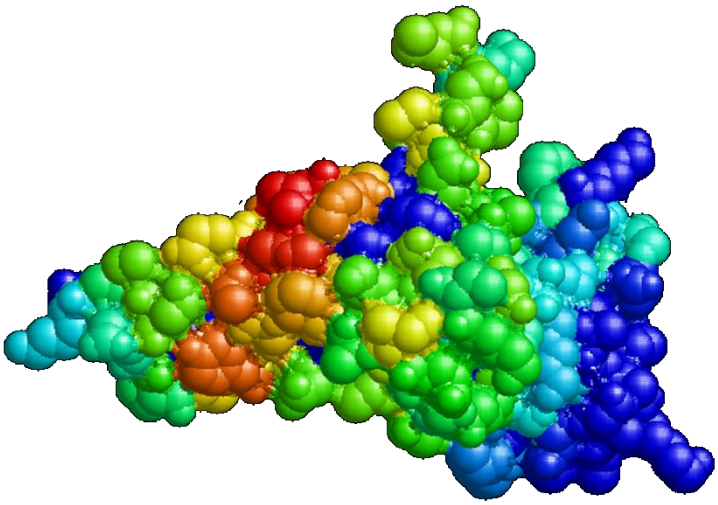

Figure IV.8 – WHISCY prediction of the most probable surface of interaction, based on sequence conservation. Red: most probable. Green, blue: least probable. Figure created with RasMol [31].

BiGGER was the algorithm used in the *in silico* docking calculations. No information about the mode of interaction or the binding sites of either protein is needed *a priori*, although BiGGER can easily accommodate experimental restraints such as those derived from 2D NMR experiments in its calculations. The software usually keeps the 5000-best ranked geometric complementarity solutions, which can be further analyzed in all the terms previously described [16, 32].

The results of the docking simulations between rubredoxin and the SOR model are graphically summarized in Fig. IV.9.

Attending to the fact that rubredoxin and SOR have surfaces with opposite charges (Figure IV.7), with rubredoxin being negative and SOR mainly uncharged with some positive charges around the catalytic center, and based on the results on ionic strength dependence from steady-state kinetics (*vide infra*), the docking solutions were ranked by the electrostatic score (Figure IV.9A).

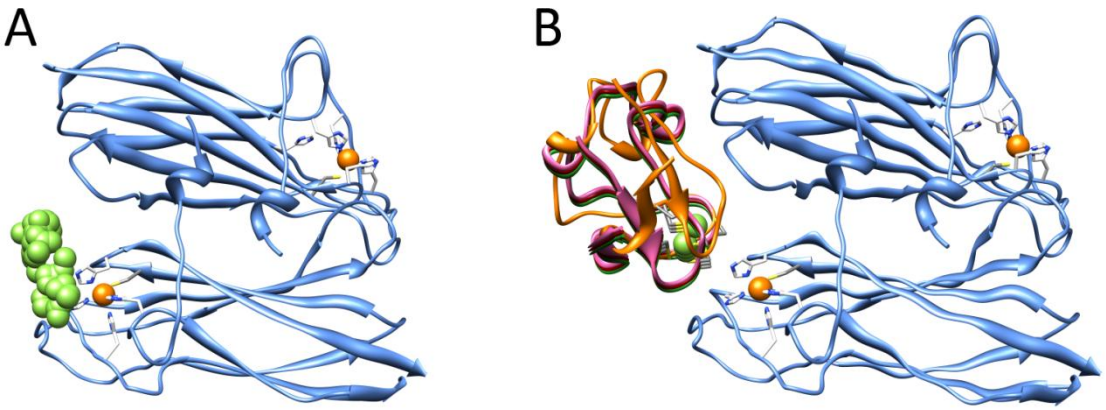

Figure IV.9 – A) Restrained-docking simulations for *D. gigas* rubredoxin – SOR complex. SOR's backbone is represented as a blue ribbon, and its Fe atom as an orange sphere. The top 100 solutions ranked by the electrostatic score are represented as light-green spheres centered on their Fe ion. B) Three best model structures of the electron transfer complex, with a minimum distance between the NH group of both C9 and C42 of rubredoxin to the Fe ion of SOR center. In these models rubredoxin is coloured blue, magenta and white, with Fe atoms depicted in orange. Images created with UCSF Chimera.

The restrained-docking calculations using BiGGER placed the redox centers of both proteins within a distance of 11 Å or less, based on experimental results, which is considered to be efficient for electron transfer [33]. These solutions were then analyzed in terms of the proportion between chemical shift differences observed experimentally and distance values in the model complexes. From the initial 100 solutions, the number was reduced to four (Figure IV.9B). These solutions were further analyzed using the PDBe PISA algorithm (as described in Materials and Methods).

The analysis of these complexes shows as expected that the most affected rubredoxin residues identified in the 2D NMR titration experiments are located in the interface of the complex (rubredoxin residues 9, 10, 42, 43, 44 and 45, Fig. IV.2), as expected.

These top complexes have a gap volume that is suitable for ET complexes (around 2100 $Å^3$ each), using a single patch from the surface of each partner, and all have a higher

percentage of polar residues in the interface than in the total of the protein surface (a general increase of 10-20% at the expense of charged residues) [34] . The accessible surface area is around 270 $Å^2$ with a gap volume index of 4.0 Å, which is consistent with the formation of a transient complex. Hydrogen bonds are not formed in these complexes, a feature that is to be expected from short-lived ET partners.

Steady-state kinetic assays were also performed to assess the dependence of the reaction rate on the ionic strength (between 6.5 and 506.5 mM), as described in Materials and Methods (Figure IV.10). In electron-transfer complexes, ionic strength plays a key role, since the encounter complex formation is dependent on the complementarity of charged surface patches near the metal centers of the interacting proteins.

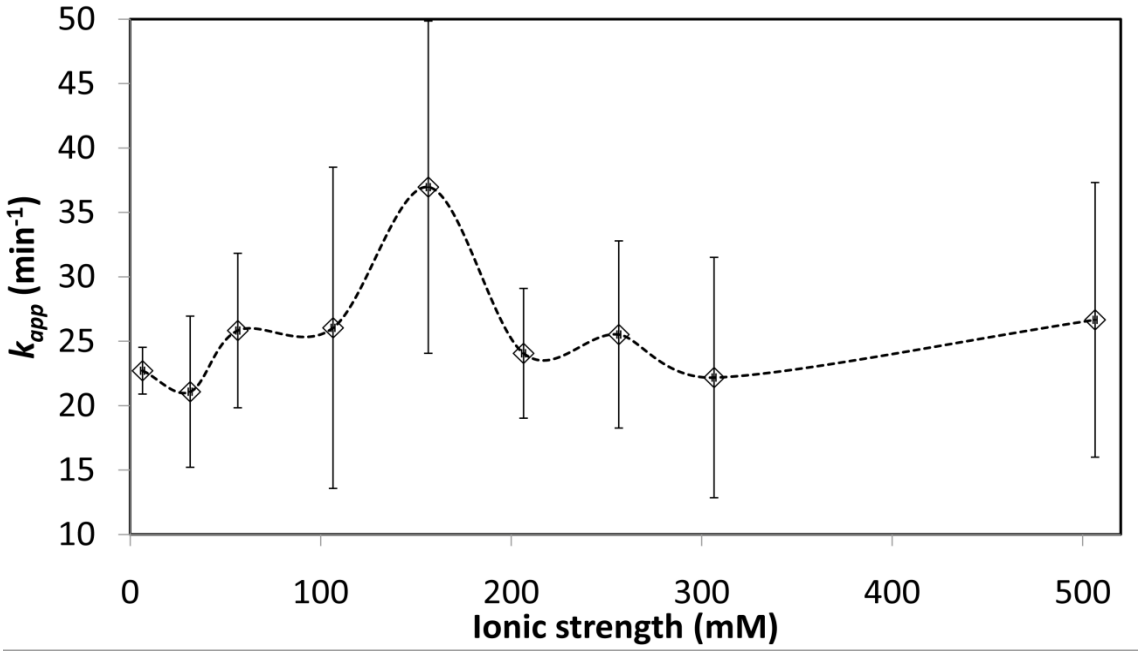

Figure IV.10 – Determination of the k_{app} values for the rate of superoxide-mediated rubredoxin oxidation at 494 nm, at different ionic strengths.

The ionic strength dependence of the rate of superoxide-mediated rubredoxin oxidation exhibits a bell-shaped curve, with a small increase between 100 and 200 mM, which can be explained taking into account the electrostatic character of the complex. A similar bell-shaped curve was observed for the reaction rate of another system involving rubredoxin, the

rubredoxin – rubredoxin:oxygen oxidoreductase [35], and in this case the maximum activity occurred at around 150 mM ionic strength, with a k_{app} value of 37 ± 12 min^{-1}.

This can be explained by the amount of ions present in the solvent being able to finely tune the electrostatic repulsions that may occur between rubredoxin and SOR by shielding through ionic interactions. Similarly, the lack of shielding at lower I values may lead to a tighter association of the complex, thus decreasing the value of k_{off}. When in excess, the nature of the complex ceases to be electrostatic in nature, thus decreasing affinity and, concomitantly, the electron transfer rate. The calculated value is in line with what was described in phosphate buffer in earlier work (31 min^{-1}) [8].

IV.4.2 Desulforedoxin as an electron donor to SOR

In Figure IV.11, selected regions of the assigned [^{15}N, ^{1}H] TROSY-HSQC spectrum of ^{15}N-Zn-desulforedoxin [14] are displayed, in the absence and in the presence of 1.5 equivalents of superoxide reductase.

Contrary to what was shown before for rubredoxin, none of desulforedoxin resonances experience large shifts or linewidth broadening (an average increase of 3 Hz was determined, independent of the localization of the residue in the protein structure) (Fig. IV.12).

The magnitude of the observed chemical shifts is substantially smaller when compared to the rubredoxin-SOR complex. Furthermore, the most affected residues in this titration are located in buried areas of the protein (hence the absence of dark grey-coloured residues in figure IV.11B).

Therefore, a defined complex between desulforedoxin and superoxide reductase was not observed by NMR, either at I = 32 mM or I = 50 mM. This can be explained considering that either

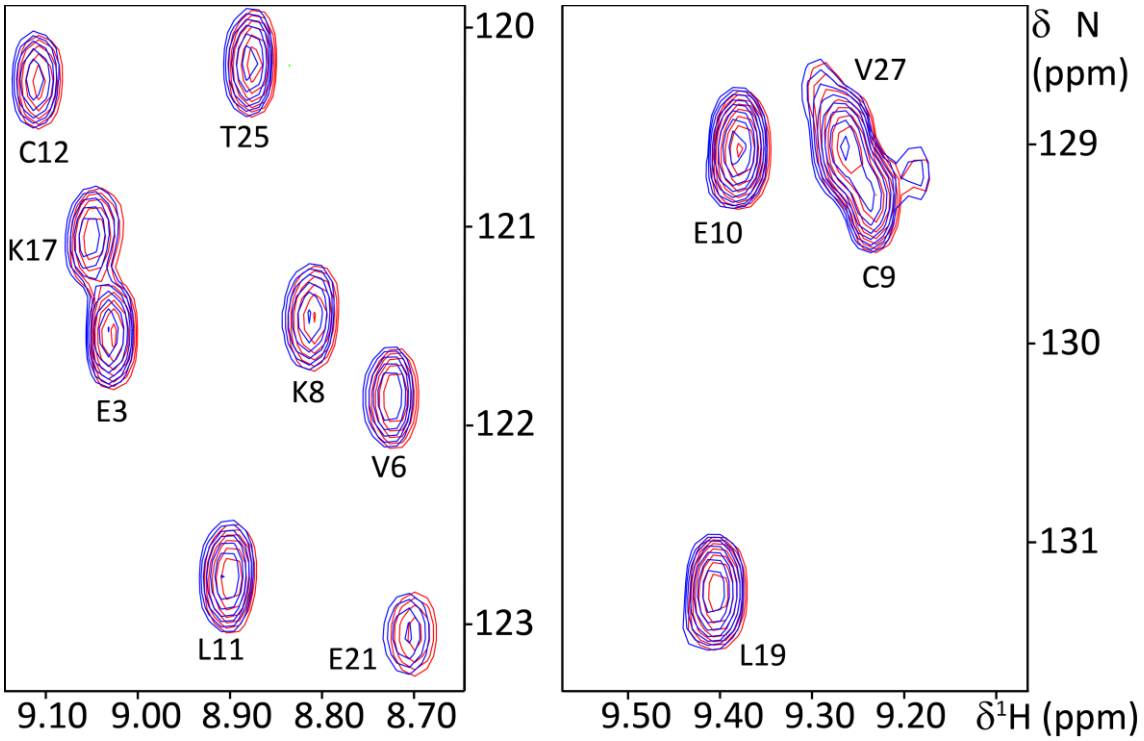

Figure IV.11 - [^{1}H, ^{15}N] TROSY-HSQC spectra of 400 μM Zn-desulforedoxin in the absence (red) and with 1.5 equivalents of superoxide reductase added. (blue). Spectra were acquired on a Bruker AvanceIII 600 spectrometer at 298 K, at an ionic strength of 50 mM.

(1) the encounter complex has an activation energy that is very similar to several productive ET complex(es) (thus bringing to the forefront the duality of the requirement for both fast electron transfer and high turnover rates), and thus we are observing an ensemble of possible orientations, which averages out the chemical shifts, or

(2) the complex has a large k_{off}, meaning that its lifetime is very small, and thus no chemical shift variation is observed in the NMR time scale.

(3) There can still be electron transfer between the two proteins without binding

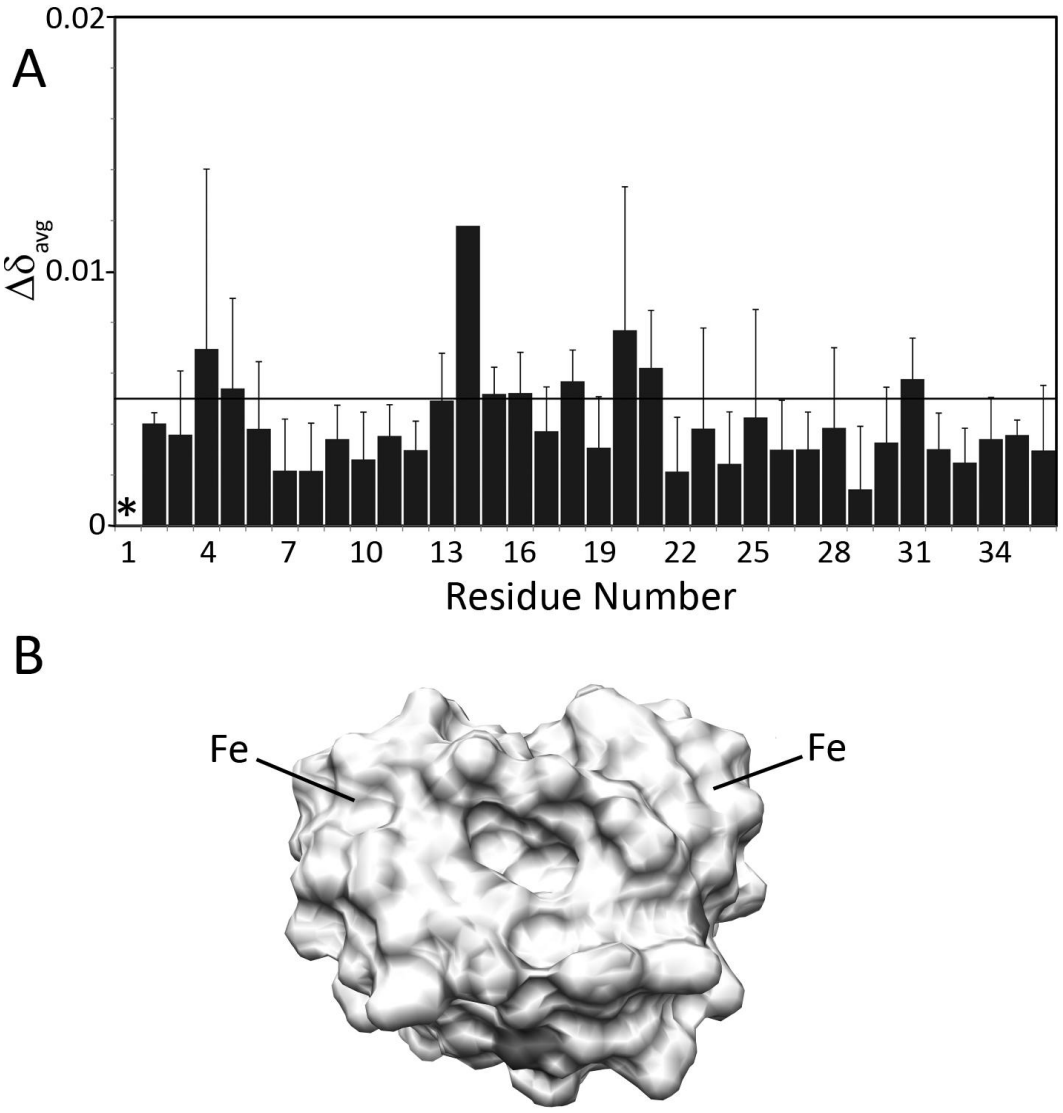

Figure IV.12 – A) Garrett plot of the titration between ^{15}N-Zn-desulforedoxin and SOR. B) Most affected residues (grey colour) above the threshold line of $\Delta\delta > 0.05$. Most are not visible due to being buried within the protein core.

Steady-state kinetic studies showed, as had also been shown previously [8], that desulforedoxin is indeed a competent electron donor to SOR.

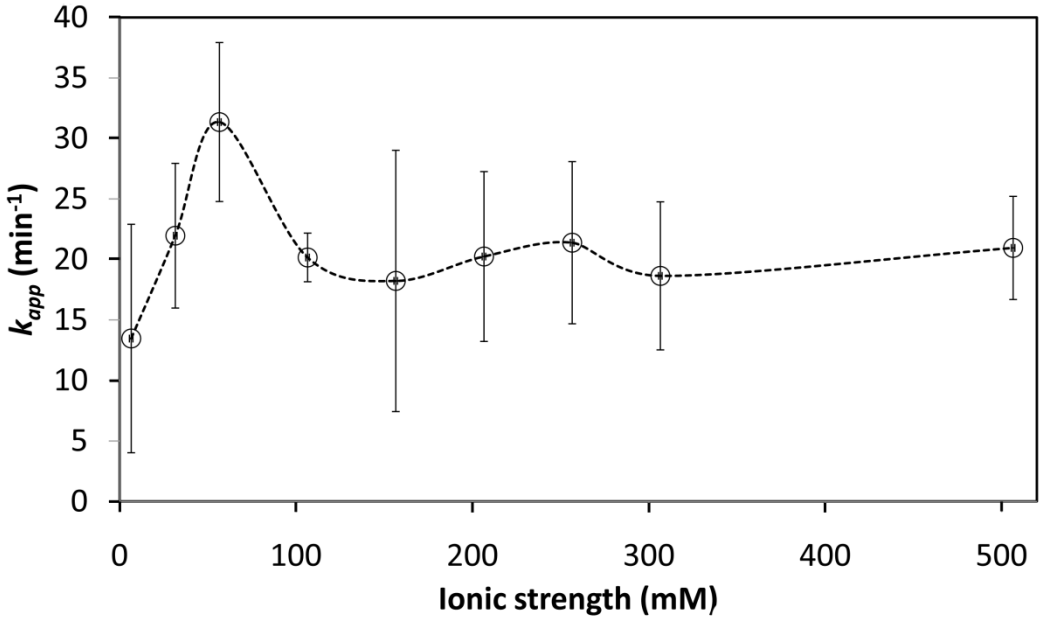

Figure IV.13 – Ionic strength dependence of the electron transfer rate between desulforedoxin and SOR. Values represent a median and the standard deviation.

Similarly to rubredoxin-SOR complex, the desulforedoxin-SOR complex also exhibits a bell-shaped ionic strength dependence. The reaction rate is of the same magnitude (31 ± 7 min^{-1} per monomer, Figure IV.13). Thus, the difference must reside in the overall affinity (k_{on} and k_{off}) of the complex, which hampers the detection by conventional 2D NMR methods. One way to overcome this situation could lie in the determination of the longitudinal and transversal relaxation rates of the amide groups of each individual aminoacid residue (R1 and R2, respectively). This type of experiments takes advantage of the fact that a target's conformational entropy changes upon binding of a ligand, reflecting itself in the relaxation rates of the affected resonances. Furthermore, use of PRE probes, such as the ones used in Chapter III could possibly overcome this limitation of standard HSQC experiments, by augmenting the relaxation effects near desulforedoxin's binding site that can be reversed upon SOR binding. These experiments could also aid in the estimation of the correlation time (τ_c), which, as a rule of thumb, increases 1 ns per 2 kDa increase, thus enabling the determination of the formation of a complex, and its relative ratio to unbound proteins.

IV.4.3 Competition assays

It would be expected that the addition of desulforedoxin to a 1:1 mixture of rubredoxin:SOR should reverse, at least partially, some of the spectral changes previously observed in 2D NMR spectra, if both protein compete for the same binding site. Likewise, in steady-state kinetics, addition of ET-incompetent Zn-rubredoxin to a catalytic mixture of desulforedoxin and SOR should lower the value of the observed ET rate (measured by the desulforedoxin re-oxidation rate).

Thus, to determine whether desulforedoxin binds to superoxide reductase in the same region as rubredoxin, a competition study by NMR and steady-state kinetics was performed (Figure IV.14 and Figure IV.15).

The titration of desulforedoxin into a solution of Zn-rubredoxin and superoxide reductase at a ratio of 1:1, was followed by 2D NMR until a ratio of 3 (Figure IV.14).

The chemical shift difference between the last point of the titration and the 1 equivalent complex rubredoxin-superoxide reductase shows that rubredoxin is being displaced upon desulforedoxin binding. Therefore, both electron transfer proteins bind at concurring sites at superoxide reductase surface. It is worthy pointing out that this titration was carried out in a 14.1 T (600 MHz) spectrometer using a TROSY-class HSQC pulse sequence, while the previous rubredoxin-SOR measurements were performed in a 18.8 T spectrometer, also using a TROSY-class HSQC pulse sequence.

In the 14.1 T titration, rubredoxin resonances broaden beyond detection, an occurrence that is marginally avoided in the 18.8 T spectra at similar [rubredoxin]/[SOR] ratios. This might be due to the design of the TROSY pulse sequences, which for amide pairs are optimal in the 900-1100 MHz (21.1 T – 25.8 T) range, with decreasing efficiency as the magnetic field lowers in magnitude [36, 37].

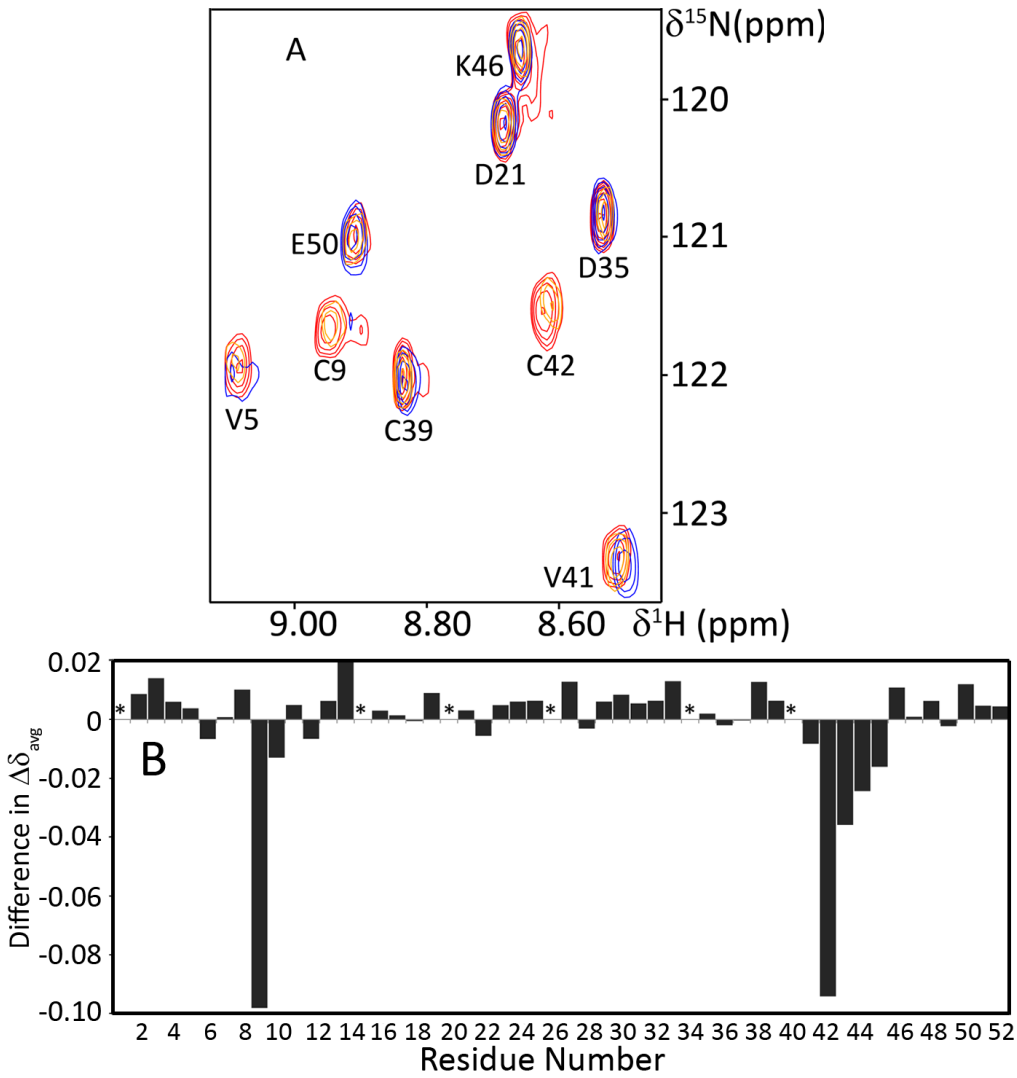

Figure IV.14 – A) 2D NMR competition assay between desulforedoxin and rubredoxin for binding to SOR. Red colour: Rubredoxin:Desulforedoxin:SOR = 1:0:0; Blue colour: Rubredoxin:Desulforedoxin:SOR = 1:0:1; Orange colour: Rubredoxin:Desulforedoxin:SOR = 1:3:1. Note that resonances C9 and C42, which broaden beyond detection upon SOR binding, become sharpened upon addition of excess desulforedoxin. B) Changes in the averaged chemical shift between 1:1 rubredoxin:superoxide reductase complex, and 1:1:3 rubredoxin:superoxide reductase:desulforedoxin.

The steady-state kinetic assays using desulforedoxin as an electron donor showed that it has a behavior modulated by the ionic strength, with a maximum at 50 mM. As such, steady-state kinetic competition studies were performed in the presence of Zn-rubredoxin, which is

redox inactive (Figure IV.15). These experiments show that there is a decrease in the rate of oxidation of Fe-desulforedoxin, indicating that rubredoxin must be competing with desulforedoxin for the same site at superoxide reductase surface, to produce competent complexes. A half-maximum inhibition constant was also calculated, with IC_{50} = 0.4 μM. Moreover, calculated k_{app} values are similar in range and behavior to rubredoxin, albeit with a maximum electron transfer rate at lower values of I (50 mM).

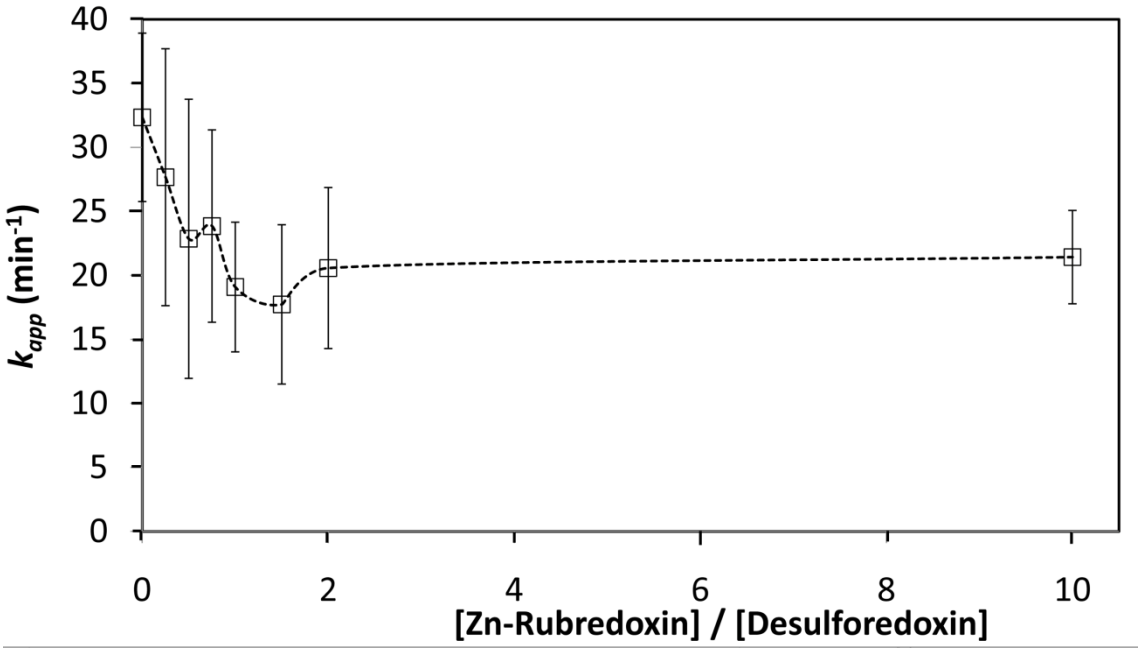

Figure IV.15 – Effect of the addition of increasing amounts of Zn-rubredoxin on the desulforedoxin reoxidation rate in the presence of superoxide and catalytic amounts of SOR, measured at 504 nm.

Although it was not possible to determine which desulforedoxin residues are involved in the complex with superoxide reductase, the competition experiments show that the binding region of superoxide reductase surface of both proteins must overlay.

Moreover, as desulforedoxin is a competent electron donor to SOR, the distance between the redox centers of these two proteins must be smaller than 10 Å. Therefore, BiGGER was used to obtain a model structure of desulforedoxin-superoxide reductase complex using that restraint (Fig. IV.16). The 100 most probable electrostatic energy minimization solutions of the docking between desulforedoxin and SOR, centered on the Fe atoms (green spheres).

The algorithm successfully predicted a localization of the most probable complexes within the interacting region calculated by WHISCY.

Also, similarly to rubredoxin, desulforedoxin binds near the positively-charged patch close to the Fe center of SOR. This configuration would favor a high-turnover, fast dissociation of the complexes [26].

However, while rubredoxin metal center is surrounded exclusively by polar and apolar amino acids (valine, threonine, glycine, tryptophan, alanine and tyrosine) that will favor the formation of a more stable electron transfer complex by hydrophobic interaction energy minimization, desulforedoxin metal center contains oppositely charged aminoacids near the metal center (lysine 8, glutamate 10 and glutamate 31) that will bring upon poorer stability while interacting with the hydrophobic region of SOR in the metal center vicinity.

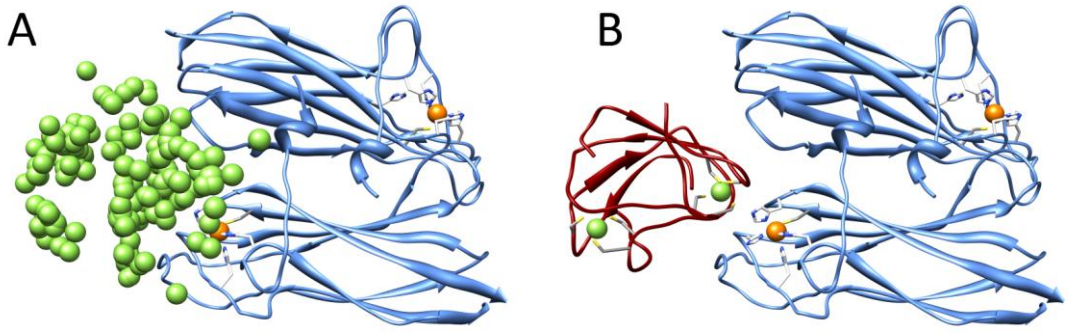

Figure IV.16 – A) Restrained-docking simulations for *D. gigas* desulforedoxin – SOR complex. SOR's backbone is represented in blue ribbon, and its Fe atom as an orange sphere. The top 100 solutions ranked by the Fe-Fe distance score are represented as light-green spheres centered on their Fe ion. B) Best model structure of the electron transfer complex, obtained by intersecting the top 200 electrostatic energy minimization solutions with the top 200 solutions in terms of Fe-Fe distance, with a minimum distance between the Fe atoms of both desulforedoxin (dark red ribbon) and SOR of 10 Å. Images created with UCSF Chimera.

In Fig. IV.17 the residues involved in the structure models obtained by BiGGER are highlighted. Indeed, the most affected desulforedoxin resonances on a 2D NMR titration are not located in the vicinity of the metal center. Reflecting that observation, the most

probable complexes calculated by BiGGER have very distinct orientations relative to SOR, and a considerably smaller interface area when compared to rubredoxin – a state known as dynamic docking [38-40].

It was still possible to estimate a value for the K_d based on the methodology described in refs. [41, 42], by fitting the observed chemical shift values of selected NH resonances in the competition NMR titration, using the previously calculated K_d value for the rubredoxin-SOR complex as one of the independent variables. The results are summarized in Fig. IV.18.

Based on the simulation of the NMR data, even though one could not observe any significant chemical shifts in a 2D NMR titration due to either the desulforedoxin-superoxide reductase complex being largely in the encounter complex state, or having a very large k_{off}, it was still possible to calculate a value for the K_d of this complex that is very similar to the one of rubredoxin-superoxide reductase complex. Thus, the magnitude of this value might explain the observed inhibition in steady-state kinetics experiments, as well as the displacement of rubredoxin in competitition NMR assays.

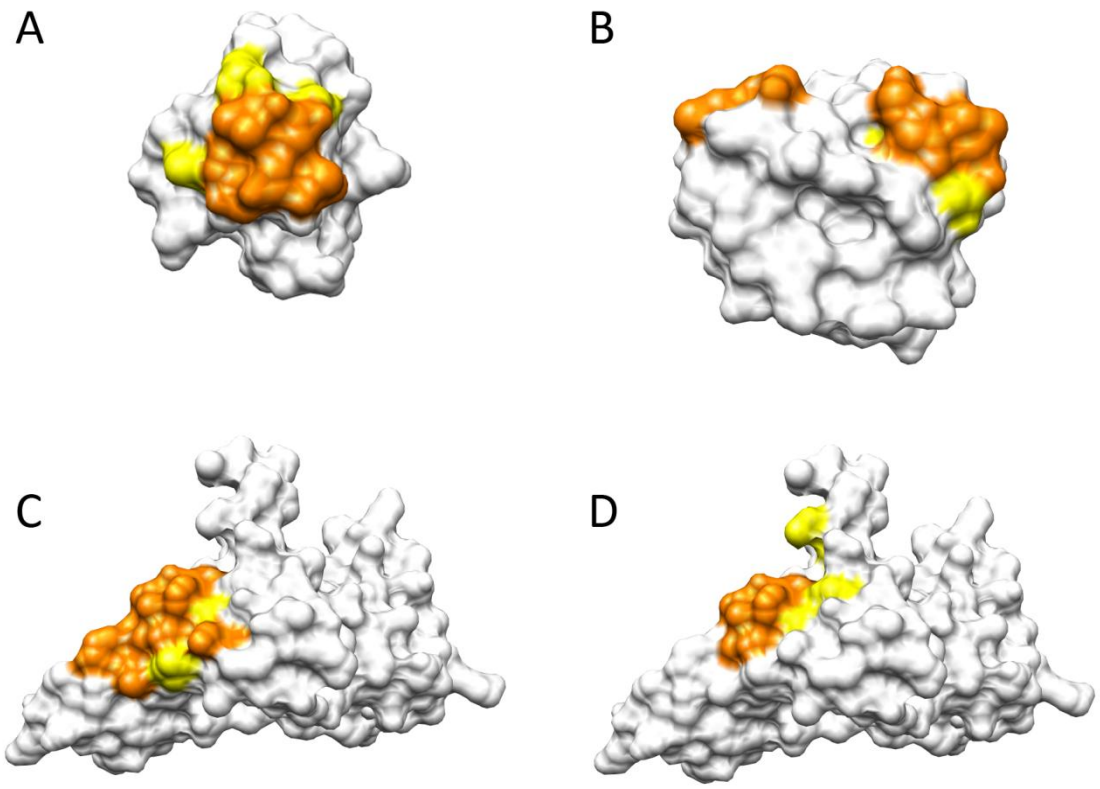

Figure IV.17 – Most probable residues involved in the complex interface. A) rubredoxin. B) desulforedoxin. C) Superoxide reductase upon interaction with rubredoxin; D) Superoxide reductase upon interaction with desulforedoxin. Orange colour: residues present in the complex interface in all the analyzed geometries. Yellow: residues present in the complex interface in part of the analyzed geometries.

However, one should always exert great care when comparing these values, as well as the IC_{50} value predicted earlier. NMR is a technique not sensitive enough to accurately predict K_d values under 10 μM [43]. Furthermore, the putative presence of encounter complexes might be masking the true value of the overall desulforedoxin-superoxide reductase complex K_d, as the presence of several equivalent species may contribute to a miscalculation of the dissociation constant [44].

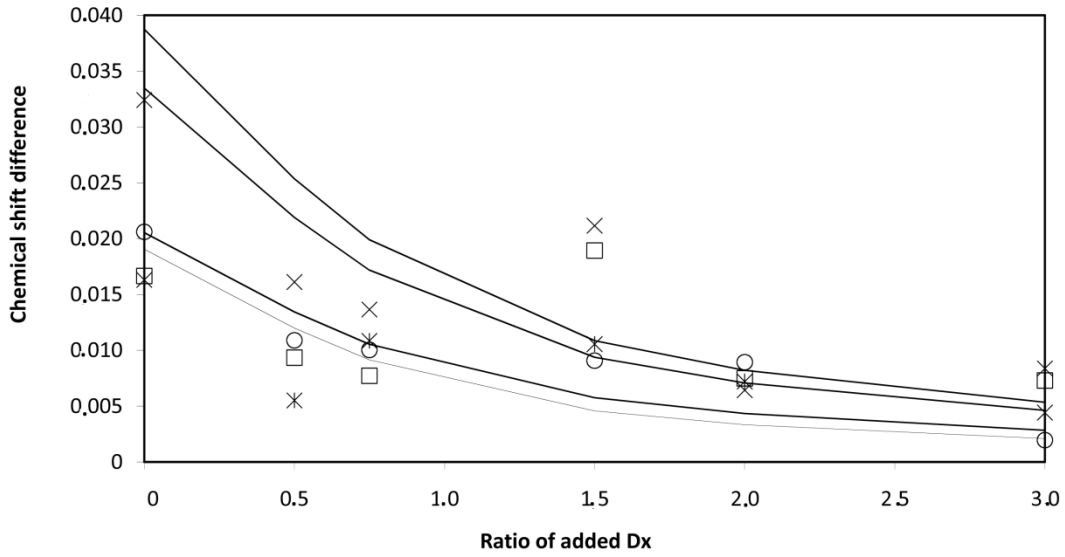

Figure IV.18 – Estimation of the K_d value for the desulforedoxin-superoxide reductase interaction, based on the decrease of chemical shift change magnitude of selected rubredoxin resonances near its active center. Legend: O = V8; □ = G10; × = G43; * = A44. The estimated value for the dissociation constant (2.5 μM) is of the same magnitude as the one of rubredoxin (3 μM).

IV.5 Conclusions

In the present work, it was shown that rubredoxin from *D. gigas* can form a defined transient complex with one of its physiological electron transfer partners, superoxide reductase. The high-spin paramagnetic Fe ion of its active center induces dipolar relaxation in selected residues of rubredoxin (C9 and C42), which causes severe half-height linewidth broadening. Chemical shift perturbation mapping upon complex formation allowed the determination of the interacting surface of rubredoxin, which was taken into account to perform molecular docking simulations using BiGGER.

The complex formed is electrostatic in nature, as shown by the dependence of reaction rate on ionic strength, reaching a maximum of 37 min^{-1} at about I = 150 mM. The K_d of the complex at 50 mM ionic strength and at 298 K was estimated to be 3 μM for a 1:1 complex.

Desulforedoxin was also shown to be a competent *in vitro* electron donor to superoxide reductase, with an estimated k_{app} of 31 min^{-1} per reaction center at 50 mM ionic strength. The complexes formed with SOR are also electrostatic in nature, and as proposed for rubredoxin, this might be due to the negatively charged patch around the Fe center that interacts with the positive patch near SOR's active site. However, the desulforedoxin surface could not be determined experimentally, as chemical shift perturbation mapping does not reveal any significant shifts or linewidth broadenings in any of the observed resonances. This might be due to a very large association/dissociation rate that does not enable following chemical shift perturbations, or due to the presence of encounter complexes that may have similar energies to the productive ET complex, thus rendering an ensemble of orientations with similar energy, indistinguishable by NMR in the conditions used. The presence of charged residues in the immediate vicinity of the desulforedoxin metal center (one lysine and one glutamate) might have a role in the apparent poorer definition of this ET complex.

The interchangeability role of these ET proteins enables them to interact in several different orientations with different redox partners [45].

Competition assays allowed for the estimation of a K_d value for the desulforedoxin-superoxide reductase complex very similar to the one of rubredoxin.

CHAPTER V – FINAL REMARKS

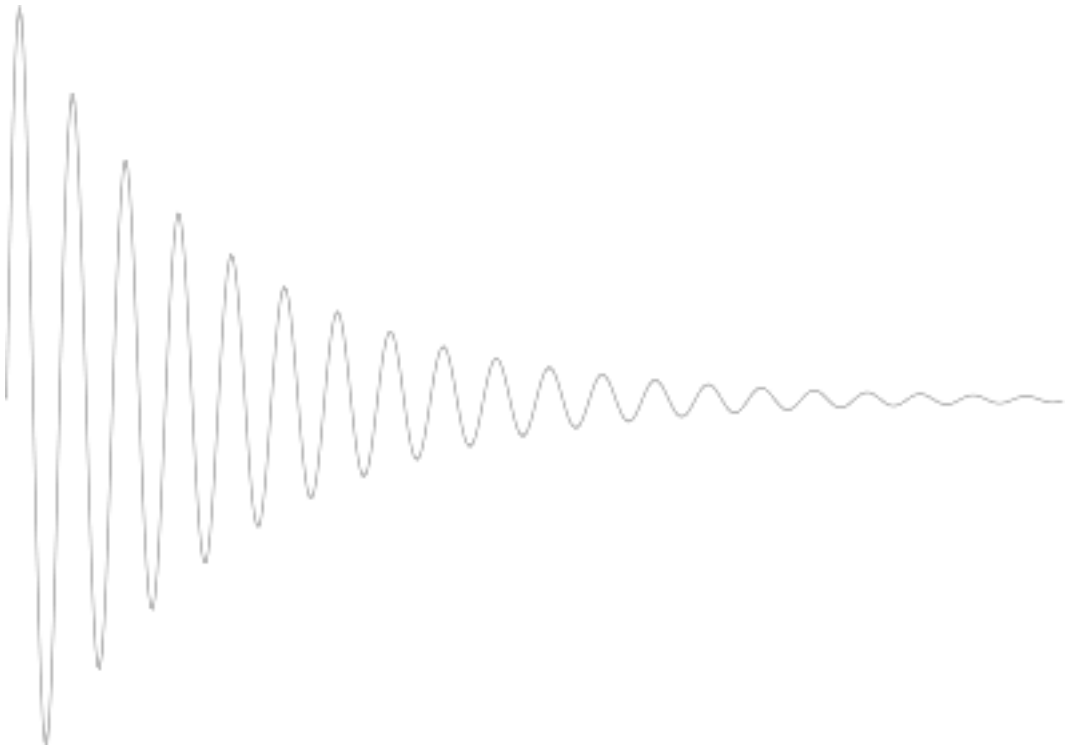

The work described in this thesis uses extensively NMR methods. NMR is nowadays considered the most versatile spectroscopic technique for the study of the structure/function and dynamics of biomolecules in solution, and it is a unique tool that can obtain information at atomic level in physiological conditions. The field of applications of biological NMR is wide both in extension and interests, and challenged by structural genomic projects, systems biology and, in particular, in the characterization of transient protein complexes. The technique offers a valuable approach in order to structurally understand protein-protein interactions that are required to occur in most significant biological processes.

Since these are transient protein complexes, one of the best ways to structurally characterize them combines *ab-initio* docking calculations and interaction site mapping using heteronuclear NMR experiments. Chemical shift perturbation (CSP) analysis also enabled the identification/mapping of the surface involved in the recognition interface using ^{1}H and ^{1}H-^{15}N HSQC experiments. Models of the complexes, generated using an *ab-initio* docking software called BiGGER, were filtered using experimental input (NMR mapping of the interacting site). Binding interfaces were examined through the application of paramagnetic NMR using paramagnetic relaxation enhancement inducing probes.

The work developed was focus on two main topics: to study ET transient protein complexes not amenable to direct structural resolution by crystallographic methods, and to establish the potential use of protein- and cyclen-derived paramagnetic probes as aides in the study of transient complexes. The versatility of paramagnetic effects was demonstrated in order to determine the geometry and affinity of transient complexes.

Relevant results were obtained on:

i) ET complex between rubredoxin and cytochrome c_3, a model-system (Chapter II);

ii) Use of lanthanide probes for mapping interacting protein surfaces (Chapter III);

iii) Physiological ET complexes between superoxide reductase and either rubredoxin or desulforedoxin (Chapter IV).

In the rubredoxin – cytochrome c_3 model system (Chapter II), the presence of a low-spin Fe ion (S = ½) in each of the four hemes perturbs the NMR resonances, shifting several heme resonances (in particular, heme methyl protons) to the 35-10 ppm region in ^{1}H NMR spectra, thus providing a good set of resonances that were used to evaluate possible binding modes of interacting partners.

Rubredoxin, that contains a high-spin FeS_4 center (S=5/2 in the oxidized state) and is negatively charged at physiological pH values, was shown to bind specifically near cytochrome c_3 heme IV, causing enhanced specific line broadenings (40 to 200 Hz increase) as well as chemical shift perturbations (0.1 to 0.2 ppm) in a typical ^{1}H NMR protein-protein titration experiment In addition, binding of rubredoxin in the vicinity of heme IV lead to allosteric effects on resonances from the other hemes, which caused relatively large chemical shift perturbations (0.2 ppm), without added line broadenings. An HSQC titration using ^{15}N-labeled rubredoxin revealed that the binding surface involves residues near its metal center (C9, G10, C42, G43, A44).

Fitting of a 1:1 binding model to the available experimental data (both chemical shift perturbations and linewidth broadenings) showed that the resulting complex has a K_d value consistent with that of other low affinity complexes (25 μM).

Lanthanide probes have been used before successfully in protein biochemistry as aids in the determination of protein structure (by adding paramagnetic constraints, such as PCS or RDCs), but their mode of action usually involves primary structure mutagenesis or some sort of chemical modification in order to covalently attach the Ln probes to the polypeptide chain. Here, it was reported the use of two cyclen-derived macrocyclic Gd-containing probes, $[Gd\text{-}DOTAM]^{3+}$ and $[Gd\text{-}DOTP]^{5-}$, in the assessment of protein-protein complex formation (chapter III). In fact, Gd^{3+}, with its seven isotropically-distributed unpaired electrons, is a very efficient nuclear spin relaxation enhancement species, with its PRE effects being observed at distances up to 15 Å from the Gd^{3+} ion.

When applied to the system described in chapter II, the complex between cytochrome c3 and rubredoxin, it was observed that Gd-DOTP binds near cytochrome c_3 heme IV, causing

strong relaxation effects on its methyl resonances even at low titers in a NMR titration experiment. The affinity of this complex is similar to that of rubredoxin (K_d = 20 μM). On the other hand, Gd-DOTP binds near rubredoxin metal center, as observed in a HSQC titration experiment, causing the broadening of several resonances near the metal center of the protein, some beyond the limit of detection. A competition assay involving ^{15}N-rubredoxin, cytochrome c_3 and Gd-DOTP allowed the correct determination of the cytochrome c_3 binding mode to rubredoxin by analyzing the resonance intensity recovery of rubredoxin cross-peaks upon addition of increasing amounts of cytochrome c_3.

Finally, the previously gathered knowledge was used to study the physiological electron transfer complexes between superoxide reductase and either rubredoxin or desulforedoxin (Chapter IV). Though superoxide reductase proved to be not an amenable protein under the standard NMR conditions for solution structure determination, it was still possible to prove the formation of productive electron transfer complexes. The complex formed between rubredoxin and superoxide reductase was well characterized by 2D NMR titrations, in which the high-spin (S= 5/2) Fe center of SOR caused large line width broadenings and chemical shift changes on a subset of rubredoxin resonances near the metal center (C9, C42 and directly adjacent residues). The estimated upper value limit for this complex's K_d is 3 μM. The same, however, could not be observed for desulforedoxin, possibly owing to the very fast dissociation time of the complex for the NMR time-scale.

Competition assays, using both 2D NMR titration and steady-state kinetics were instrumental in establishing the binding mode of desulforedoxin to superoxide reductase. Under the same conditions, both rubredoxin and desulforedoxin exhibited similar superoxide-mediated re-oxidation rates (k_{app} = 37 vs 31 min^{-1}, respectively). Excess Zn-rubredoxin can inhibit the re-oxidation rate of Fe-desulforedoxin (IC_{50} = 0.4 μM), while HSQC spectra showed that addition of desulforedoxin to a 1:1 mixture of rubredoxin and superoxide reductase lead to reversal of SOR-induced effects on rubredoxin, as desulforedoxin competed for binding at the same site. It was then possible to calculate a K_d value for the desulforedoxin-superoxide reductase complex based on the NMR competition assay, which, is similar to the one of rubredoxin (K_d = 2.5 μM).

These approaches were complemented with *in silico* protein-protein docking procedures. The algorithm that was used was BiGGER, which can incorporate experimentally-driven constraints in order to predict with increased levels of confidence the structures of the possible complexes that are formed (chapters II and IV).

In summary, this work successfully proposed the use of different kinds of probes (Fe protein- and cyclen-based) to assess the formation, stoichiometry and affinity of different transient complexes, which can be used in the future to study a myriad of possible protein-protein interactions or, in the case of Ln probes, to serve also as a source of constraints for protein structure determination.

CHAPTER VI – BIBLIOGRAPHY

VI. Bibliography

Chapter I

[1] E. Franzosa, B. Linghu, Y. Xia, Computational reconstruction of protein-protein interaction networks: algorithms and issues, Methods in molecular biology (Clifton, N.J 541 (2009) 89-100.

[2] S.P. Kanaan, C. Huang, S. Wuchty, D.Z. Chen, J.A. Izaguirre, Inferring protein-protein interactions from multiple protein domain combinations, Methods in molecular biology (Clifton, N.J 541 (2009) 43-59.

[3] W. Kelly, M. Stumpf, Protein-protein interactions: from global to local analyses, Current opinion in biotechnology 19 (2008) 396-403.

[4] T.M. Przytycka, M. Singh, D.K. Slonim, Toward the dynamic interactome: it's about time, Briefings in bioinformatics 11 (2009) 15-29.

[5] M. Vidal, A unifying view of 21st century systems biology, FEBS letters 583 (2009) 3891-3894.

[6] P.B. Crowley, M.A. Carrondo, The architecture of the binding site in redox protein complexes: implications for fast dissociation, Proteins 55 (2004) 603-612.

[7] M. Prudencio, M. Ubbink, Transient complexes of redox proteins: structural and dynamic details from NMR studies, J Mol Recognit 17 (2004) 524-539.

[8] M. Ubbink, The courtship of proteins: understanding the encounter complex, FEBS letters 583 (2009) 1060-1066.

[9] E.R. Zuiderweg, Mapping protein-protein interactions in solution by NMR spectroscopy, Biochemistry 41 (2002) 1-7.

[10] P.B. Crowley, M. Ubbink, Close encounters of the transient kind: protein interactions in the photosynthetic redox chain investigated by NMR spectroscopy, Accounts of chemical research 36 (2003) 723-730.

[11] A. McPherson, Introduction to protein crystallization, Methods (San Diego, Calif 34 (2004) 254-265.

[12] T. Ochi, V.M. Bolanos-Garcia, V. Stojanoff, A. Moreno, Perspectives on protein crystallisation, Progress in biophysics and molecular biology 101 (2009) 56-63.

[13] F.E. Jenney, Jr., M.F. Verhagen, X. Cui, M.W. Adams, Anaerobic microbes: oxygen detoxification without superoxide dismutase, Science (New York, N.Y 286 (1999) 306-309.

[14] G. Katona, P. Carpentier, V. Niviere, P. Amara, V. Adam, J. Ohana, N. Tsanov, D. Bourgeois, Raman-assisted crystallography reveals end-on peroxide intermediates in a nonheme iron enzyme, Science (New York, N.Y 316 (2007) 449-453.

[15] A. Naito, Structure elucidation of membrane-associated peptides and proteins in oriented bilayers by solid-state NMR spectroscopy, Solid state nuclear magnetic resonance 36 (2009) 67-76.

[16] A. McDermott, Structure and dynamics of membrane proteins by magic angle spinning solid-state NMR, Annual review of biophysics 38 (2009) 385-403.

[17] K. Pervushin, Impact of transverse relaxation optimized spectroscopy (TROSY) on NMR as a technique in structural biology, Quarterly reviews of biophysics 33 (2000) 161-197.

[18] K. Pervushin, The use of TROSY for detection and suppression of conformational exchange NMR line broadening in biological macromolecules, Journal of biomolecular NMR 20 (2001) 275-285.

[19] D. Susan-Resiga, T. Nowak, Monitoring active site alterations upon mutation of yeast pyruvate kinase using 205Tl+ NMR, The Journal of biological chemistry 278 (2003) 40943-40952.

[20] I.C. Felli, B. Brutscher, Recent advances in solution NMR: fast methods and heteronuclear direct detection, Chemphyschem 10 (2009) 1356-1368.

[21] S. Hiller, C. Wasmer, G. Wider, K. Wuthrich, Sequence-specific resonance assignment of soluble nonglobular proteins by 7D APSY-NMR spectroscopy, Journal of the American Chemical Society 129 (2007) 10823-10828.

[22] C. Dominguez, R. Boelens, A.M. Bonvin, HADDOCK: a protein-protein docking approach based on biochemical or biophysical information, Journal of the American Chemical Society 125 (2003) 1731-1737.

[23] A. Fahmy, G. Wagner, TreeDock: a tool for protein docking based on minimizing van der Waals energies, Journal of the American Chemical Society 124 (2002) 1241-1250.

[24] I.S. Moreira, P.A. Fernandes, M.J. Ramos, Protein-protein docking dealing with the unknown, Journal of computational chemistry (2009).

[25] I.S. Moreira, P.A. Fernandes, M.J. Ramos, Protein-protein docking dealing with the unknown, Journal of computational chemistry 31 (2010) 317-342.

[26] L. Krippahl, J.J. Moura, P.N. Palma, Modeling protein complexes with BiGGER, Proteins 52 (2003) 19-23.

[27] P.N. Palma, L. Krippahl, J.E. Wampler, J.J. Moura, BiGGER: a new (soft) docking algorithm for predicting protein interactions, Proteins 39 (2000) 372-384.

[28] R.E. Summons, L.L. Jahnke, J.M. Hope, G.A. Logan, 2-Methylhopanoids as biomarkers for cyanobacterial oxygenic photosynthesis, Nature 400 (1999) 554-557.

[29] A. Dolla, M. Fournier, Z. Dermoun, Oxygen defense in sulfate-reducing bacteria, Journal of biotechnology 126 (2006) 87-100.

[30] K. Keyer, J.A. Imlay, Superoxide accelerates DNA damage by elevating free-iron levels, Proceedings of the National Academy of Sciences of the United States of America 93 (1996) 13635-13640.

[31] E. Nagababu, J.M. Rifkind, Reaction of hydrogen peroxide with ferrylhemoglobin: superoxide production and heme degradation, Biochemistry 39 (2000) 12503-12511.

[32] C. Andreini, L. Banci, I. Bertini, S. Elmi, A. Rosato, Non-heme iron through the three domains of life, Proteins 67 (2007) 317-324.

[33] J.-M. Mouesca, B. Lamotte, Iron-Sulfur clusters and their electronic and magnetic properties, Coord. Chem. Rev. 178-180 (1998) 1573-1614.

[34] M. Archer, A.L. Carvalho, S. Teixeira, I. Moura, J.J. Moura, F. Rusnak, M.J. Romao, Structural studies by X-ray diffraction on metal substituted desulforedoxin, a rubredoxin-type protein, Protein Sci 8 (1999) 1536-1545.

[35] M. Archer, R. Huber, P. Tavares, I. Moura, J.J. Moura, M.A. Carrondo, L.C. Sieker, J. LeGall, M.J. Romao, Crystal structure of desulforedoxin from Desulfovibrio gigas determined at 1.8 A resolution: a novel non-heme iron protein structure, Journal of molecular biology 251 (1995) 690-702.

[36] F. Auchere, S.R. Pauleta, P. Tavares, I. Moura, J.J. Moura, Kinetics studies of the superoxide-mediated electron transfer reactions between rubredoxin-type proteins and superoxide reductases, J Biol Inorg Chem 11 (2006) 433-444.

[37] A.S. Pereira, P. Tavares, F. Folgosa, R.M. Almeida, I. Moura, J.J. Moura, Superoxide Reductases, European Journal of Inorganic Chemistry 2007 (2007) 2569-2581.

[38] E.D. Coulter, D.M. Kurtz, Jr., A role for rubredoxin in oxidative stress protection in Desulfovibrio vulgaris: catalytic electron transfer to rubrerythrin and two-iron superoxide reductase, Archives of biochemistry and biophysics 394 (2001) 76-86.

[39] A.J. Pierik, R.B. Wolbert, G.L. Portier, M.F. Verhagen, W.R. Hagen, Nigerythrin and rubrerythrin from Desulfovibrio vulgaris each contain two mononuclear iron centers and two dinuclear iron clusters, European journal of biochemistry / FEBS 212 (1993) 237-245.

[40] L. Chen, M.Y. Liu, J. LeGall, P. Fareleira, H. Santos, A.V. Xavier, Rubredoxin oxidase, a new flavo-hemo-protein, is the site of oxygen reduction to water by the "strict anaerobe" Desulfovibrio gigas, Biochemical and biophysical research communications 193 (1993) 100-105.

[41] C.M. Gomes, G. Silva, S. Oliveira, J. LeGall, M.Y. Liu, A.V. Xavier, C. Rodrigues-Pousada, M. Teixeira, Studies on the redox centers of the terminal oxidase from Desulfovibrio gigas and evidence for its interaction with rubredoxin, The Journal of biological chemistry 272 (1997) 22502-22508.

[42] W. Lovenberg, B.E. Sobel, Rubredoxin: a new electron transfer protein from Clostridium pasteurianum, Proceedings of the National Academy of Sciences of the United States of America 54 (1965) 193-199.

[43] J. Meyer, J.-M. Moulis, Rubredoxin, in: A. Messerschmidt, R. Huber, K. Wieghardt, T. Poulos (Eds.), Handbook of Metalloproteins, John Wiley and Sons, Inc., 2001.

[44] P.R. Blake, J.B. Park, F.O. Bryant, S. Aono, J.K. Magnuson, E. Eccleston, J.B. Howard, M.F. Summers, M.W. Adams, Determinants of protein hyperthermostability: purification and amino acid sequence of rubredoxin from the hyperthermophilic archaebacterium Pyrococcus furiosus and secondary structure of the zinc adduct by NMR, Biochemistry 30 (1991) 10885-10895.

[45] J.V. Rodrigues, I.A. Abreu, L.M. Saraiva, M. Teixeira, Rubredoxin acts as an electron donor for neelaredoxin in Archaeoglobus fulgidus, Biochemical and biophysical research communications 329 (2005) 1300-1305.

[46] T.H. Smits, S.B. Balada, B. Witholt, J.B. van Beilen, Functional analysis of alkane hydroxylases from gram-negative and gram-positive bacteria, Journal of bacteriology 184 (2002) 1733-1742.

[47] F. Auchere, R. Sikkink, C. Cordas, P. Raleiras, P. Tavares, I. Moura, J.J. Moura, Overexpression and purification of Treponema pallidum rubredoxin; kinetic evidence for a superoxide-mediated electron transfer with the superoxide reductase neelaredoxin, J Biol Inorg Chem 9 (2004) 839-849.

[48] B.J. Henriques, L.M. Saraiva, C.M. Gomes, Combined spectroscopic and calorimetric characterisation of rubredoxin reversible thermal transition, J Biol Inorg Chem 11 (2006) 73-81.

[49] J. Wastl, E.C. Duin, L. Iuzzolino, W. Dorner, T. Link, S. Hoffmann, H. Sticht, H. Dau, K. Lingelbach, U.G. Maier, Eukaryotically encoded and chloroplast-located rubredoxin is associated with photosystem II, The Journal of biological chemistry 275 (2000) 30058-30063.

[50] R.E. Stenkamp, L.C. Sieker, L.H. Jensen, The structure of rubredoxin from Desulfovibrio desulfuricans strain 27774 at 1.5 A resolution, Proteins 8 (1990) 352-364.

[51] J. LeGall, M.Y. Liu, C.M. Gomes, V. Braga, I. Pacheco, M. Regalla, A.V. Xavier, M. Teixeira, Characterisation of a new rubredoxin isolated from Desulfovibrio desulfuricans 27774: definition of a new family of rubredoxins, FEBS letters 429 (1998) 295-298.

[52] E.F. Pettersen, T.D. Goddard, C.C. Huang, G.S. Couch, D.M. Greenblatt, E.C. Meng, T.E. Ferrin, UCSF Chimera--a visualization system for exploratory research and analysis, Journal of computational chemistry 25 (2004) 1605-1612.

[53] J.B. van Beilen, E.G. Funhoff, Alkane hydroxylases involved in microbial alkane degradation, Applied microbiology and biotechnology 74 (2007) 13-21.

[54] L. Yu, M. Kennedy, C. Czaja, P. Tavares, J.J. Moura, I. Moura, F. Rusnak, Conversion of desulforedoxin into a rubredoxin center, Biochemical and biophysical research communications 231 (1997) 679-682.

[55] B.J. Goodfellow, F. Rusnak, I. Moura, C.S. Ascenso, J.J. Moura, NMR solution structures of two mutants of desulforedoxin, Journal of inorganic biochemistry 93 (2003) 100-108.

[56] P.M. Pereira, Q. He, A.V. Xavier, J. Zhou, I.A. Pereira, R.O. Louro, Transcriptional response of Desulfovibrio vulgaris Hildenborough to oxidative stress mimicking environmental conditions, Archives of microbiology 189 (2008) 451-461.

[57] W. Zhang, D.E. Culley, M. Hogan, L. Vitiritti, F.J. Brockman, Oxidative stress and heat-shock responses in Desulfovibrio vulgaris by genome-wide transcriptomic analysis, Antonie van Leeuwenhoek 90 (2006) 41-55.

[58] W. Zhang, D.E. Culley, J.C. Scholten, M. Hogan, L. Vitiritti, F.J. Brockman, Global transcriptomic analysis of Desulfovibrio vulgaris on different electron donors, Antonie van Leeuwenhoek 89 (2006) 221-237.

[59] I.A. Abreu, D.E. Cabelli, Superoxide dismutases-a review of the metal-associated mechanistic variations, Biochimica et biophysica acta 1804 (2010) 263-274.

[60] J.J. Perry, D.S. Shin, E.D. Getzoff, J.A. Tainer, The structural biochemistry of the superoxide dismutases, Biochimica et biophysica acta 1804 (2010) 245-262.

[61] M. Kitamura, T. Nakanishi, S. Kojima, I. Kumagai, H. Inoue, Cloning and expression of the catalase gene from the anaerobic bacterium Desulfovibrio vulgaris (Miyazaki F), Journal of biochemistry 129 (2001) 357-364.

[62] T. Nakanishi, H. Inoue, M. Kitamura, Cloning and expression of the superoxide dismutase gene from the obligate anaerobic bacterium Desulfovibrio vulgaris (Miyazaki F), Journal of biochemistry 133 (2003) 387-393.

[63] I. Moura, P. Tavares, J.J. Moura, N. Ravi, B.H. Huynh, M.Y. Liu, J. LeGall, Purification and characterization of desulfoferrodoxin. A novel protein from Desulfovibrio desulfuricans (ATCC 27774) and from Desulfovibrio vulgaris (strain Hildenborough) that contains a distorted rubredoxin center and a mononuclear ferrous center, The Journal of biological chemistry 265 (1990) 21596-21602.

[64] L. Chen, P. Sharma, J. Le Gall, A.M. Mariano, M. Teixeira, A.V. Xavier, A blue non-heme iron protein from Desulfovibrio gigas, European journal of biochemistry / FEBS 226 (1994) 613-618.

[65] T. Santos-Silva, J. Trincao, A.L. Carvalho, C. Bonifacio, F. Auchere, P. Raleiras, I. Moura, J.J. Moura, M.J. Romao, The first crystal structure of class III superoxide reductase from Treponema pallidum, J Biol Inorg Chem 11 (2006) 548-558.

[66] M.J. Pianzzola, M. Soubes, D. Touati, Overproduction of the rbo gene product from Desulfovibrio species suppresses all deleterious effects of lack of superoxide dismutase in Escherichia coli, Journal of bacteriology 178 (1996) 6736-6742.

[67] J.F. Heidelberg, R. Seshadri, S.A. Haveman, C.L. Hemme, I.T. Paulsen, J.F. Kolonay, J.A. Eisen, N. Ward, B. Methe, L.M. Brinkac, S.C. Daugherty, R.T. Deboy, R.J. Dodson, A.S. Durkin, R. Madupu, W.C. Nelson, S.A. Sullivan, D. Fouts, D.H. Haft, J. Selengut, J.D. Peterson, T.M. Davidsen, N. Zafar, L. Zhou, D. Radune, G. Dimitrov, M. Hance, K. Tran, H. Khouri, J. Gill, T.R. Utterback, T.V. Feldblyum, J.D. Wall, G. Voordouw, C.M. Fraser, The genome sequence of the anaerobic, sulfate-reducing bacterium Desulfovibrio vulgaris Hildenborough, Nature biotechnology 22 (2004) 554-559.

[68] G. Silva, S. Oliveira, C.M. Gomes, I. Pacheco, M.Y. Liu, A.V. Xavier, M. Teixeira, J. Legall, C. Rodrigues-pousada, Desulfovibrio gigas neelaredoxin. A novel superoxide dismutase integrated in a putative oxygen sensory operon of an anaerobe, European journal of biochemistry / FEBS 259 (1999) 235-243.

[69] G. Silva, S. Oliveira, J. LeGall, A.V. Xavier, C. Rodrigues-Pousada, Analysis of the Desulfovibrio gigas transcriptional unit containing rubredoxin (rd) and rubredoxin-oxygen oxidoreductase (roo) genes and upstream ORFs, Biochemical and biophysical research communications 280 (2001) 491-502.

[70] A.S. Pereira, P. Tavares, F. Folgosa, R.M. Almeida, I. Moura, J.J.G. Moura, Superoxide reductases, Eur J Inorg Chem (2007) 2569-2581.

[71] J.V. Rodrigues, B.L. Victor, H. Huber, L.M. Saraiva, C.M. Soares, D.E. Cabelli, M. Teixeira, Superoxide reduction by Nanoarchaeum equitans neelaredoxin, an enzyme lacking the highly conserved glutamate iron ligand, J Biol Inorg Chem 13 (2008) 219-228.

[72] A.V. Coelho, P. Matias, V. Fulop, A. Thompson, A. Gonzalez, M.A. Carrondo, Desulfoferrodoxin Structure Determined by MAD Phasing and Refinement to 1.9 Angstroms Resolution Reveals a Unique Combination of a Tetrahedral Fes4 Centre with a Square Pyramidal Fesn4 Centre, J Biol Inorg Chem 2 (1997) 680-689.

[73] V.W. Huang, J.P. Emerson, D.M. Kurtz, Jr., Reaction of Desulfovibrio vulgaris two-iron superoxide reductase with superoxide: insights from stopped-flow spectrophotometry, Biochemistry 46 (2007) 11342-11351.

[74] J.P. Emerson, D.E. Cabelli, D.M. Kurtz, Jr., An engineered two-iron superoxide reductase lacking the [Fe(SCys)4] site retains its catalytic properties in vitro and in vivo, Proceedings of the National Academy of Sciences of the United States of America 100 (2003) 3802-3807.

[75] A.P. Yeh, Y. Hu, F.E. Jenney, Jr., M.W. Adams, D.C. Rees, Structures of the superoxide reductase from Pyrococcus furiosus in the oxidized and reduced states, Biochemistry 39 (2000) 2499-2508.

[76] I.A. Abreu, L.M. Saraiva, J. Carita, H. Huber, K.O. Stetter, D. Cabelli, M. Teixeira, Oxygen detoxification in the strict anaerobic archaeon Archaeoglobus fulgidus: superoxide scavenging by neelaredoxin, Molecular microbiology 38 (2000) 322-334.

[77] K.E. Nelson, R.A. Clayton, S.R. Gill, M.L. Gwinn, R.J. Dodson, D.H. Haft, E.K. Hickey, J.D. Peterson, W.C. Nelson, K.A. Ketchum, L. McDonald, T.R. Utterback, J.A. Malek, K.D. Linher, M.M. Garrett, A.M. Stewart, M.D. Cotton, M.S. Pratt, C.A. Phillips, D. Richardson, J. Heidelberg, G.G. Sutton, R.D. Fleischmann, J.A. Eisen, O. White, S.L. Salzberg, H.O. Smith, J.C. Venter, C.M. Fraser, Evidence for lateral gene transfer between Archaea and bacteria from genome sequence of Thermotoga maritima, Nature 399 (1999) 323-329.

[78] P.M. Matias, J. Morais, R. Coelho, M.A. Carrondo, K. Wilson, Z. Dauter, L. Sieker, Cytochrome c3 from Desulfovibrio gigas: crystal structure at 1.8 A resolution and evidence for a specific calcium-binding site, Protein Sci 5 (1996) 1342-1354.

[79] I.B. Coutinho, A.V. Xavier, Tetraheme cytochromes, Methods in enzymology 243 (1994) 119-140.

[80] J.R. Postgate, Dependence of sulphate reduction and oxygen utilization on a cytochrome in Desulphovibrio, The Biochemical journal 58 (1954) ix.

[81] R.O. Louro, Proton thrusters: overview of the structural and functional features of soluble tetrahaem cytochromes c3, J Biol Inorg Chem 12 (2007) 1-10.

[82] I. Bertini, G. Cavallaro, A. Rosato, Cytochrome c: occurrence and functions, Chemical reviews 106 (2006) 90-115.

[83] P.M. Matias, A.V. Coelho, F.M. Valente, D. Placido, J. LeGall, A.V. Xavier, I.A. Pereira, M.A. Carrondo, Sulfate respiration in Desulfovibrio vulgaris Hildenborough. Structure of the 16-heme cytochrome c HmcA AT 2.5-A resolution and a view of its role in transmembrane electron transfer, The Journal of biological chemistry 277 (2002) 47907-47916.

[84] P.M. Matias, I.A. Pereira, C.M. Soares, M.A. Carrondo, Sulphate respiration from hydrogen in Desulfovibrio bacteria: a structural biology overview, Progress in biophysics and molecular biology 89 (2005) 292-329.

[85] P.M. Matias, L.M. Saraiva, C.M. Soares, A.V. Coelho, J. LeGall, M.A. Carrondo, Nine-haem cytochrome c from Desulfovibrio desulfuricans ATCC 27774:primary sequence determination, crystallographic refinement at 1.8 and modelling studies of its interaction with the tetrahaem cytochrome c3, J Biol Inorg Chem 4 (1999) 478-494.

[86] P.M. Matias, C.M. Soares, L.M. Saraiva, R. Coelho, J. Morais, J. Le Gall, M.A. Carrondo, [NiFe] hydrogenase from Desulfovibrio desulfuricans ATCC 27774: gene sequencing, three-dimensional structure determination and refinement at 1.8 A and modelling studies of its interaction with the tetrahaem cytochrome c3, J Biol Inorg Chem 6 (2001) 63-81.

[87] R.S. Lemos, C.M. Gomes, M. Santana, J. LeGall, A.V. Xavier, M. Teixeira, The 'strict' anaerobe Desulfovibrio gigas contains a membrane-bound oxygen-reducing respiratory chain, FEBS letters 496 (2001) 40-43.

[88] G. Fauque, D. Herve, J. Le Gall, Structure-function relationship in hemoproteins: the role of cytochrome c3 in the reduction of colloidal sulfur by sulfate-reducing bacteria, Archives of microbiology 121 (1979) 261-264.

[89] G.P. Moss, Nomenclature of tetrapyrroles, European journal of biochemistry / FEBS 178 (1988) 277-328.

[90] A.V. Xavier, A mechano-chemical model for energy transduction in cytochrome c oxidase: the work of a Maxwell's god, FEBS letters 532 (2002) 261-266

Chapter II

[1] I. Bertini, C. Luchinat, G. Parigi, Paramagnetic constraints: An aid for quick solution structure determination of paramagnetic metalloproteins, Concepts in Magnetic Resonance 14 (2002) 259-286.

[2] I. Bertini, C. Luchinat, G. Parigi, R. Pierattelli, NMR spectroscopy of paramagnetic metalloproteins, Chembiochem 6 (2005) 1536-1549.

[3] M. Ubbink, J.A. Worrall, G.W. Canters, E.J. Groenen, M. Huber, Paramagnetic resonance of biological metal centers, Annu Rev Biophys Biomol Struct 31 (2002) 393-422.

[4] K. Pervushin, R. Riek, G. Wider, K. Wuthrich, Attenuated T2 relaxation by mutual cancellation of dipole-dipole coupling and chemical shift anisotropy indicates an avenue to NMR structures of very large biological macromolecules in solution, Proceedings of the National Academy of Sciences of the United States of America 94 (1997) 12366-12371.

[5] C.R. Sanders, F. Sonnichsen, Solution NMR of membrane proteins: practice and challenges, Magn Reson Chem 44 Spec No (2006) S24-40.

[6] G.M. Clore, C. Tang, J. Iwahara, Elucidating transient macromolecular interactions using paramagnetic relaxation enhancement, Current opinion in structural biology 17 (2007) 603-616.

[7] M.D. Vlasie, R. Fernandez-Busnadiego, M. Prudencio, M. Ubbink, Conformation of pseudoazurin in the 152 kDa electron transfer complex with nitrite reductase determined by paramagnetic NMR, Journal of molecular biology 375 (2008) 1405-1415.

[8] A.N. Volkov, Q. Bashir, J.A. Worrall, M. Ubbink, Binding hot spot in the weak protein complex of physiological redox partners yeast cytochrome C and cytochrome C peroxidase, Journal of molecular biology 385 (2009) 1003-1013.

[9] Q. Yi, J.E. Erman, J.D. Satterlee, Proton NMR studies of noncovalent complexes of cytochrome c peroxidase-cyanide with horse and yeast ferricytochromes c, Biochemistry 32 (1993) 10988-10994.

[10] P.N. Palma, I. Moura, J. LeGall, J. Van Beeumen, J.E. Wampler, J.J. Moura, Evidence for a ternary complex formed between flavodoxin and cytochrome c3: 1H-NMR and molecular modeling studies, Biochemistry 33 (1994) 6394-6407.

[11] M.A. Picarra-Pereira, D.L. Turner, J. LeGall, A.V. Xavier, Structural studies on Desulfovibrio gigas cytochrome c3 by two-dimensional 1H-nuclear-magnetic-resonance spectroscopy, Biochem J 294 (Pt 3) (1993) 909-915.

[12] L. Brennan, D.L. Turner, A.C. Messias, M.L. Teodoro, J. LeGall, H. Santos, A.V. Xavier, Structural basis for the network of functional cooperativities in cytochrome c(3) from Desulfovibrio gigas: solution structures of the oxidised and reduced states, Journal of molecular biology 298 (2000) 61-82.

[13] H. Shimada, S. Nagano, Y. Ariga, M. Unno, T. Egawa, T. Hishiki, Y. Ishimura, F. Masuya, T. Obata, H. Hori, Putidaredoxin-cytochrome p450cam interaction. Spin state of the heme iron modulates putidaredoxin structure, The Journal of biological chemistry 274 (1999) 9363-9369.

[14] A. Osyczka, K.V. Nagashima, K. Shimada, K. Matsuura, Interaction site for high-potential iron-sulfur protein on the tetraheme cytochrome subunit bound to the photosynthetic reaction center of Rubrivivax gelatinosus, Biochemistry 38 (1999) 2861-2865.

[15] T. Nogi, I. Fathir, M. Kobayashi, T. Nozawa, K. Miki, Crystal structures of photosynthetic reaction center and high-potential iron-sulfur protein from Thermochromatium tepidum: thermostability and electron transfer, Proc. Natl. Acad. Sci. U S A 97 (2000) 13561-13566.

[16] P. Lamosa, L. Brennan, H. Vis, D.L. Turner, H. Santos, NMR structure of Desulfovibrio gigas rubredoxin: a model for studying protein stabilization by compatible solutes, Extremophiles 5 (2001) 303-311.

[17] L. Krippahl, J.J. Moura, P.N. Palma, Modeling protein complexes with BiGGER, Proteins 52 (2003) 19-23.

[18] M. van Dijk, A.D. van Dijk, V. Hsu, R. Boelens, A.M. Bonvin, Information-driven protein-DNA docking using HADDOCK: it is a matter of flexibility, Nucleic Acids Res 34 (2006) 3317-3325.

[19] R.M. Almeida, S.R. Pauleta, I. Moura, J.J. Moura, Rubredoxin as a paramagnetic relaxation-inducing probe, Journal of inorganic biochemistry 103 (2009) 1245-1253.

[20] J. Sambrook, D. Russel, Molecular Cloning - A laboratory manual, 3rd ed., Cold Spring Harbor Laboratory Press, Cold Spring Harbor, New York, 2001.

[21] R. Keller, The Computer Aided Resonance Assignment Tutorial, CANTINA Verlag 2004.

[22] G.P. Moss, Nomenclature of tetrapyrroles. Recommendations 1986 IUPAC-IUB Joint Commission on Biochemical Nomenclature (JCBN), Eur J Biochem 178 (1988) 277-328.

[23] D.E. Stewart, J.E. Wampler, Molecular dynamics simulations of the cytochrome c3-rubredoxin complex from Desulfovibrio vulgaris, Proteins 11 (1991) 142-152.

[24] A.S. Oliveira, V.H. Teixeira, A.M. Baptista, C.M. Soares, Reorganization and conformational changes in the reduction of tetraheme cytochromes, Biophys J 89 (2005) 3919-3930.

[25] N. Bloembergen, Proton Relaxation Times in Paramagnetic Solutions, Journal of Chemical Physics 27 (1957) 2.

[26] I. Solomon, Relaxation Processes in a system of two spins, Physical Review 99 (1955) 7.

[27] C. Capeillere-Blandin, Flavocytochrome b2-cytochrome c interactions: the electron transfer reaction revisited, Biochimie 77 (1995) 516-530.

[28] M.L. Paddock, K.H. Weber, C. Chang, M.Y. Okamura, Interactions between cytochrome c2 and the photosynthetic reaction center from Rhodobacter sphaeroides: the cation-pi interaction, Biochemistry 44 (2005) 9619-9625.

[29] F. Auchere, S.R. Pauleta, P. Tavares, I. Moura, J.J. Moura, Kinetics studies of the superoxide-mediated electron transfer reactions between rubredoxin-type proteins and superoxide reductases, J Biol Inorg Chem 11 (2006) 433-444.

[30] C. Frazao, G. Silva, C.M. Gomes, P. Matias, R. Coelho, L. Sieker, S. Macedo, M.Y. Liu, S. Oliveira, M. Teixeira, A.V. Xavier, C. Rodrigues-Pousada, M.A. Carrondo, J. Le Gall, Structure of a dioxygen reduction enzyme from Desulfovibrio gigas, Nature structural biology 7 (2000) 1041-1045.

[31] D.E. Stewart, J. LeGall, I. Moura, J.J. Moura, H.D. Peck, Jr., A.V. Xavier, P.K. Weiner, J.E. Wampler, A hypothetical model of the flavodoxin-tetraheme cytochrome c3 complex of sulfate-reducing bacteria, Biochemistry 27 (1988) 2444-2450.

[32] A. Dolla, F. Guerlesquin, M. Bruschi, R. Haser, Ferredoxin electron transfer site on cytochrome c3. Structural hypothesis of an intramolecular electron transfer pathway within a tetra-heme cytochrome, J Mol Recognit 4 (1991) 27-33.

[33] D.E. Stewart, J. Legall, I. Moura, J.J. Moura, H.D. Peck, Jr., A.V. Xavier, P.K. Weiner, J.E. Wampler, Electron transport in sulfate-reducing bacteria. Molecular modeling and NMR studies of the rubredoxin--tetraheme-cytochrome-c3 complex, Eur J Biochem 185 (1989) 695-700.

[34] P.N. Palma, L. Krippahl, J.E. Wampler, J.J. Moura, BiGGER: a new (soft) docking algorithm for predicting protein interactions, Proteins 39 (2000) 372-384.

[35] E.F. Pettersen, T.D. Goddard, C.C. Huang, G.S. Couch, D.M. Greenblatt, E.C. Meng, T.E. Ferrin, UCSF Chimera--a visualization system for exploratory research and analysis, Journal of computational chemistry 25 (2004) 1605-1612.

Chapter III

[1] J.A. Peters, J. Huskens, D.J. Raber, Lanthanide induced shifts and relaxation rate enhancements, Progress in Nuclear Magnetic Resonance Spectroscopy 28 (1996) 283-350.

[2] G. Otting, Prospects for lanthanides in structural biology by NMR, Journal of biomolecular NMR 42 (2008) 1-9.

[3] S. Viswanathan, Z. Kovacs, K.N. Green, S.J. Ratnakar, A.D. Sherry, Alternatives to gadolinium-based metal chelates for magnetic resonance imaging, Chemical reviews 110 (2010) 2960-3018.

[4] P. Caravan, J.J. Ellison, T.J. McMurry, R.B. Lauffer, Gadolinium(III) Chelates as MRI Contrast Agents: Structure, Dynamics, and Applications, Chemical reviews 99 (1999) 2293-2352.

[5] G. Pintacuda, M. John, X.C. Su, G. Otting, NMR structure determination of protein-ligand complexes by lanthanide labeling, Accounts of chemical research 40 (2007) 206-212.

[6] M. Sattler, S. Fesik, Resolving Resonance Overlap in the NMR Spectra of Proteins from Differential Lanthanide-Induced Shifts, Journal of the American Chemical Society 119 (1997) 7885-7886.

[7] I. Bertini, C. Luchinat, Chapter 3 - Relaxation Coord. Chem. Rev. 150 (1996) 77-110.

[8] G. Otting, Protein NMR using paramagnetic ions, Annual review of biophysics 39 (2010) 387-405.

[9] C.F. Geraldes, C. Luchinat, Lanthanides as shift and relaxation agents in elucidating the structure of proteins and nucleic acids, Metal ions in biological systems 40 (2003) 513-588.

[10] B. Bleaney, Nuclear magnetic resonance shifts in solution due to lanthanide ions, J Magn Reson 8 (1972) 91-100.

[11] I. Bertini, M.B. Janik, Y.M. Lee, C. Luchinat, A. Rosato, Magnetic susceptibility tensor anisotropies for a lanthanide ion series in a fixed protein matrix, Journal of the American Chemical Society 123 (2001) 4181-4188.

[12] G.M. Clore, J. Iwahara, Theory, practice, and applications of paramagnetic relaxation enhancement for the characterization of transient low-population states of biological macromolecules and their complexes, Chemical reviews 109 (2009) 4108-4139.

[13] H. Yagi, K.V. Loscha, X.C. Su, M. Stanton-Cook, T. Huber, G. Otting, Tunable paramagnetic relaxation enhancements by [Gd(DPA)(3)] (3-) for protein structure analysis, Journal of biomolecular NMR 47 (2010) 143-153.

[14] A.D. Sherry, P. Caravan, R.E. Lenkinski, Primer on gadolinium chemistry, J Magn Reson Imaging 30 (2009) 1240-1248.

[15] C.F. Geraldes, S. Laurent, Classification and basic properties of contrast agents for magnetic resonance imaging, Contrast media & molecular imaging 4 (2009) 1-23.

[16] S. Aime, M. Botta, M. Fasano, E. Terreno, Lanthanide(iii) chelates for NMR biomedical applications, Chemical Society reviews 27 (1998) 19-29.

[17] P. Caravan, Strategies for increasing the sensitivity of gadolinium based MRI contrast agents, Chemical Society reviews 35 (2006) 512-523.

[18] J.P. Andre, C.F. Geraldes, J.A. Martins, A.E. Merbach, M.I. Prata, A.C. Santos, J.J. de Lima, E. Toth, Lanthanide(III) complexes of DOTA-glycoconjugates: a potential new class of lectin-mediated medical imaging agents, Chemistry (Weinheim an der Bergstrasse, Germany) 10 (2004) 5804-5816.

[19] L.R. Dick, C.F. Geraldes, A.D. Sherry, C.W. Gray, D.M. Gray, 13C NMR of methylated lysines of fd gene 5 protein: evidence for a conformational change involving lysine 24 upon binding of a negatively charged lanthanide chelate, Biochemistry 28 (1989) 7896-7904.

[20] D. Haussinger, J.R. Huang, S. Grzesiek, DOTA-M8: An extremely rigid, high-affinity lanthanide chelating tag for PCS NMR spectroscopy, Journal of the American Chemical Society 131 (2009) 14761-14767.

[21] S. Aime, N. D'Amelio, M. Fragai, Y.M. Lee, C. Luchinat, E. Terreno, G. Valensin, A paramagnetic probe to localize residues next to carboxylates on protein surfaces, J Biol Inorg Chem 7 (2002) 617-622.

[22] F. Rodriguez-Castaneda, P. Haberz, A. Leonov, C. Griesinger, Paramagnetic tagging of diamagnetic proteins for solution NMR, Magn Reson Chem 44 Spec No (2006) S10-16.

[23] X.C. Su, G. Otting, Paramagnetic labelling of proteins and oligonucleotides for NMR, Journal of biomolecular NMR 46 (2010) 101-112.

[24] G. Pintacuda, G. Otting, Identification of protein surfaces by NMR measurements with a pramagnetic Gd(III) chelate, Journal of the American Chemical Society 124 (2002) 372-373.

[25] M. Prudencio, J. Rohovec, J.A. Peters, E. Tocheva, M.J. Boulanger, M.E. Murphy, H.J. Hupkes, W. Kosters, A. Impagliazzo, M. Ubbink, A caged lanthanide complex as a paramagnetic shift agent for protein NMR, Chemistry (Weinheim an der Bergstrasse, Germany) 10 (2004) 3252-3260.

[26] P.B. Crowley, M.A. Carrondo, The architecture of the binding site in redox protein complexes: implications for fast dissociation, Proteins 55 (2004) 603-612.

[27] M. Ubbink, The courtship of proteins: understanding the encounter complex, FEBS letters 583 (2009) 1060-1066.

[28] S.C. Tam, R.J.P. Williams, Electrostatics and biological systems, Structure and Bonding (Berlin) 63 (1985) 103-151.

[29] F. Avecilla, J.A. Peters, C.F. Geraldes, X-ray Crystal Structure of a Sodium Salt of [Gd(DOTP)]5-: Implications for Its Second-Sphere Relaxivity and the 23Na NMR Hyperfine Shift Effects of [Tm(DOTP)]5-, Eur J Inorg Chem (23) (2003) 4179-4186.

[30] C. Rill, Z.I. Kolar, G. Kickelbick, H.T. Wolterbeek, J.A. Peters, Kinetics and thermodynamics of adsorption on hydroxyapatite of the [160Tb]terbium complexes of the bone-targeting ligands DOTP and BPPED, Langmuir 25 (2009) 2294-2301.

[31] D. Coman, H.K. Trubel, F. Hyder, Brain temperature by Biosensor Imaging of Redundant Deviation in Shifts (BIRDS): comparison between TmDOTP5- and TmDOTMA, NMR in biomedicine 23 277-285.

[32] E.F. Pettersen, T.D. Goddard, C.C. Huang, G.S. Couch, D.M. Greenblatt, E.C. Meng, T.E. Ferrin, UCSF Chimera--a visualization system for exploratory research and analysis, Journal of computational chemistry 25 (2004) 1605-1612.

[33] W.D. Cornell, P. Cieplak, C.I. Bayly, I.R. Gould, K.M. Merz Jr, D.M. Ferguson, D.C. Spellmeyer, T. Fox, J.W. Caldwell, P.A. Kollman, A second generation force field for the simulation of proteins,

nucleic acids, and organic molecules, Journal of the American Chemical Society 117 (1995) 5179-5197.

[34] R.M. Almeida, S.R. Pauleta, I. Moura, J.J. Moura, Rubredoxin as a paramagnetic relaxation-inducing probe, Journal of inorganic biochemistry 103 (2009) 1245-1253.

[35] S. Aime, A. Barge, M. Botta, A.S. de Sousa, D. Parker, Direct NMR Spectroscopic Observation of a Lanthanide-Coordinated Water Molecule whose Exchange Rate Is Dependent on the Conformation of the Complexes, Angew Chem Int ed
37 (1998) 2673-2675.

[36] J.F. Desreux, Nuclear magnetic resonance spectroscopy of lanthanide complexes with a tetraacetic tetraaza macrocycle. Unusual conformation properties, Inorganic chemistry 19 (1980) 1319-1324.

[37] C.F.C.G. Geraldes, A.D. Sherry, G.E. Kiefer, The solution structure of Ln (DOTP)5− complexxes. A comparison of lanthanide-induced paramagnetic shifts with the MMX energy-minimized structure, J Magn Reson 97 (1992) 290-304.

[38] I. Lazar, D.C. Hrncir, W.D. Kim, G.E. Kiefer, A.D. Sherry, Optimized synthesis, structure, and solution dynamics of 1,4,7,10-tetraazacyclododecane-1,4,7,10-tetrakis(methylenephosphonic acid) (H8DOTP), Inorganic chemistry 31 (1992) 4422-4424.

[39] R. Keller, The Computer Aided Resonance Assignment Tutorial, CANTINA Verlag 2004.

[40] D.E. Stewart, J.E. Wampler, Molecular dynamics simulations of the cytochrome c3-rubredoxin complex from Desulfovibrio vulgaris, Proteins 11 (1991) 142-152.

[41] I. Bertini, P. Turano, A.J. Vila, Nuclear Magnetic Resonance of Paramagnetic Metalloproteins, Chemical reviews 93 (1993) 2833-2932.

[42] L. Lo Conte, C. Chothia, J. Janin, The atomic structure of protein-protein recognition sites, Journal of molecular biology 285 (1999) 2177-2198.

Chapter IV

[1] W.G. Dos Santos, I. Pacheco, M.Y. Liu, M. Teixeira, A.V. Xavier, J. LeGall, Purification and characterization of an iron superoxide dismutase and a catalase from the sulfate-reducing bacterium Desulfovibrio gigas, Journal of bacteriology 182 (2000) 796-804.

[2] H. Cypionka, Oxygen respiration by desulfovibrio species, Annual review of microbiology 54 (2000) 827-848.

[3] A. Dolla, M. Fournier, Z. Dermoun, Oxygen defense in sulfate-reducing bacteria, Journal of biotechnology 126 (2006) 87-100.

[4] P.M. Pereira, Q. He, A.V. Xavier, J. Zhou, I.A. Pereira, R.O. Louro, Transcriptional response of Desulfovibrio vulgaris Hildenborough to oxidative stress mimicking environmental conditions, Archives of microbiology 189 (2008) 451-461.

[5] A.S. Pereira, P. Tavares, F. Folgosa, R.M. Almeida, I. Moura, J.J.G. Moura, Superoxide reductases, Eur. J. Inorg. Chem. (2007) 2569-2581.

[6] K.R. Strand, C. Sun, T. Li, F.E. Jenney, Jr., G.J. Schut, M.W. Adams, Oxidative stress protection and the repair response to hydrogen peroxide in the hyperthermophilic archaeon Pyrococcus furiosus and in related species, Archives of microbiology 192 (2010) 447-459.

[7] L. Chen, P. Sharma, J. Le Gall, A.M. Mariano, M. Teixeira, A.V. Xavier, A blue non-heme iron protein from Desulfovibrio gigas, European journal of biochemistry / FEBS 226 (1994) 613-618.

[8] F. Auchere, S.R. Pauleta, P. Tavares, I. Moura, J.J. Moura, Kinetics studies of the superoxide-mediated electron transfer reactions between rubredoxin-type proteins and superoxide reductases, J Biol Inorg Chem 11 (2006) 433-444.

[9] L. Chen, M.Y. Liu, J. Legall, P. Fareleira, H. Santos, A.V. Xavier, Purification and characterization of an NADH-rubredoxin oxidoreductase involved in the utilization of oxygen by Desulfovibrio gigas, European journal of biochemistry / FEBS 216 (1993) 443-448.

[10] C. Frazao, G. Silva, C.M. Gomes, P. Matias, R. Coelho, L. Sieker, S. Macedo, M.Y. Liu, S. Oliveira, M. Teixeira, A.V. Xavier, C. Rodrigues-Pousada, M.A. Carrondo, J. Le Gall, Structure of a dioxygen reduction enzyme from Desulfovibrio gigas, Nature structural biology 7 (2000) 1041-1045.

[11] C.M. Gomes, G. Silva, S. Oliveira, J. LeGall, M.Y. Liu, A.V. Xavier, C. Rodrigues-Pousada, M. Teixeira, Studies on the redox centers of the terminal oxidase from Desulfovibrio gigas and evidence for its interaction with rubredoxin, The Journal of biological chemistry 272 (1997) 22502-22508.

[12] M. Archer, R. Huber, P. Tavares, I. Moura, J.J. Moura, M.A. Carrondo, L.C. Sieker, J. LeGall, M.J. Romao, Crystal structure of desulforedoxin from Desulfovibrio gigas determined at 1.8 A resolution: a novel non-heme iron protein structure, Journal of molecular biology 251 (1995) 690-702.

[13] L. Yu, M. Kennedy, C. Czaja, P. Tavares, J.J. Moura, I. Moura, F. Rusnak, Conversion of desulforedoxin into a rubredoxin center, Biochemical and biophysical research communications 231 (1997) 679-682.

[14] B.J. Goodfellow, S.G. Nunes, F. Rusnak, I. Moura, C. Ascenso, J.J. Moura, B.F. Volkman, J.L. Markley, Zinc-substituted Desulfovibrio gigas desulforedoxins: resolving subunit degeneracy with nonsymmetric pseudocontact shifts, Protein Sci 11 (2002) 2464-2470.

[15] I. Bertini, C. Luchinat, G. Parigi, R. Pierattelli, NMR spectroscopy of paramagnetic metalloproteins, Chembiochem 6 (2005) 1536-1549.

[16] L. Krippahl, J.J. Moura, P.N. Palma, Modeling protein complexes with BiGGER, Proteins 52 (2003) 19-23.

[17] R.M. Almeida, S.R. Pauleta, I. Moura, J.J. Moura, Rubredoxin as a paramagnetic relaxation-inducing probe, Journal of inorganic biochemistry 103 (2009) 1245-1253.

[18] P. Raleiras, Superoxide Reductases, Chemistry, vol. Ph.D., Universidade Nova de Lisboa, Lisboa, 2005.

[19] K. Pervushin, The use of TROSY for detection and suppression of conformational exchange NMR line broadening in biological macromolecules, Journal of biomolecular NMR 20 (2001) 275-285.

[20] R. Keller, The Computer Aided Resonance Assignment Tutorial, CANTINA Verlag 2004.

[21] D.S. Garrett, Y.J. Seok, A. Peterkofsky, G.M. Clore, A.M. Gronenborn, Identification by NMR of the binding surface for the histidine-containing phosphocarrier protein HPr on the N-terminal domain of enzyme I of the Escherichia coli phosphotransferase system, Biochemistry 36 (1997) 4393-4398.

[22] L. Bordoli, F. Kiefer, K. Arnold, P. Benkert, J. Battey, T. Schwede, Protein structure homology modeling using SWISS-MODEL workspace, Nature protocols 4 (2009) 1-13.

[23] S. Jones, J.M. Thornton, Principles of protein-protein interactions, Proceedings of the National Academy of Sciences of the United States of America 93 (1996) 13-20.

[24] P. Lamosa, L. Brennan, H. Vis, D.L. Turner, H. Santos, NMR structure of Desulfovibrio gigas rubredoxin: a model for studying protein stabilization by compatible solutes, Extremophiles 5 (2001) 303-311.

[25] I. Bertini, Luchinat, C., Parigi, G., Paramagnetic constraints: An aid for quick solution structure determination of paramagnetic metalloproteins, Concepts in Magnetic Resonance 14 (2002) 27.

[26] P.B. Crowley, M.A. Carrondo, The architecture of the binding site in redox protein complexes: implications for fast dissociation, Proteins 55 (2004) 603-612.

[27] E.F. Pettersen, T.D. Goddard, C.C. Huang, G.S. Couch, D.M. Greenblatt, E.C. Meng, T.E. Ferrin, UCSF Chimera--a visualization system for exploratory research and analysis, Journal of computational chemistry 25 (2004) 1605-1612.

[28] R.A. Laskowski, E.G. Hutchinson, A.D. Michie, A.C. Wallace, M.L. Jones, J.M. Thornton, PDBsum: a Web-based database of summaries and analyses of all PDB structures, Trends in biochemical sciences 22 (1997) 488-490.

[29] S.J. de Vries, A.D. van Dijk, A.M. Bonvin, WHISCY: what information does surface conservation yield? Application to data-driven docking, Proteins 63 (2006) 479-489.

[30] W.D. Cornell, P. Cieplak, C.I. Bayly, I.R. Gould, K.M. Merz Jr, D.M. Ferguson, D.C. Spellmeyer, T. Fox, J.W. Caldwell, P.A. Kollman, A second generation force field for the simulation of proteins,

nucleic acids, and organic molecules, Journal of the American Chemical Society 117 (1995) 5179-5197.

[31] R.A. Sayle, E.J. Milner-White, RASMOL: biomolecular graphics for all, Trends in biochemical sciences 20 (1995) 374.

[32] P.N. Palma, L. Krippahl, J.E. Wampler, J.J. Moura, BiGGER: a new (soft) docking algorithm for predicting protein interactions, Proteins 39 (2000) 372-384.

[33] C.C. Page, C.C. Moser, X. Chen, P.L. Dutton, Natural engineering principles of electron tunnelling in biological oxidation-reduction, Nature 402 (1999) 47-52.

[34] L. Lo Conte, C. Chothia, J. Janin, The atomic structure of protein-protein recognition sites, Journal of molecular biology 285 (1999) 2177-2198.

[35] B.L. Victor, J.B. Vicente, R. Rodrigues, S. Oliveira, C. Rodrigues-Pousada, C. Frazao, C.M. Gomes, M. Teixeira, C.M. Soares, Docking and electron transfer studies between rubredoxin and rubredoxin:oxygen oxidoreductase, J Biol Inorg Chem 8 (2003) 475-488.

[36] K. Pervushin, R. Riek, G. Wider, K. Wuthrich, Attenuated T2 relaxation by mutual cancellation of dipole-dipole coupling and chemical shift anisotropy indicates an avenue to NMR structures of very large biological macromolecules in solution, Proceedings of the National Academy of Sciences of the United States of America 94 (1997) 12366-12371.

[37] C.R. Sanders, F. Sonnichsen, Solution NMR of membrane proteins: practice and challenges, Magn Reson Chem 44 Spec No (2006) S24-40.

[38] Z.X. Liang, M. Jiang, Q. Ning, B.M. Hoffman, Dynamic docking and electron transfer between myoglobin and cytochrome b(5), J Biol Inorg Chem 7 (2002) 580-588.

[39] Z.X. Liang, I.V. Kurnikov, J.M. Nocek, A.G. Mauk, D.N. Beratan, B.M. Hoffman, Dynamic docking and electron-transfer between cytochrome b5 and a suite of myoglobin surface-charge mutants. Introduction of a functional-docking algorithm for protein-protein complexes, Journal of the American Chemical Society 126 (2004) 2785-2798.

[40] J.A. Worrall, Y. Liu, P.B. Crowley, J.M. Nocek, B.M. Hoffman, M. Ubbink, Myoglobin and cytochrome b5: a nuclear magnetic resonance study of a highly dynamic protein complex, Biochemistry 41 (2002) 11721-11730.

[41] S.R. Pauleta, A. Cooper, M. Nutley, N. Errington, S. Harding, F. Guerlesquin, C.F. Goodhew, I. Moura, J.J. Moura, G.W. Pettigrew, A copper protein and a cytochrome bind at the same site on bacterial cytochrome c peroxidase, Biochemistry 43 (2004) 14566-14576.

[42] B.W. Sigurskjold, Exact analysis of competition ligand binding by displacement isothermal titration calorimetry, Analytical biochemistry 277 (2000) 260-266.

[43] L. Fielding, NMR methods for the determination of protein-ligand dissociation constants, Current topics in medicinal chemistry 3 (2003) 39-53.

[44] L. Fielding, S. Rutherford, D. Fletcher, Determination of protein-ligand binding affinity by NMR: observations from serum albumin model systems, Magn Reson Chem 43 (2005) 463-470.
[45] P.A. Williams, V. Fulop, Y.C. Leung, C. Chan, J.W. Moir, G. Howlett, S.J. Ferguson, S.E. Radford, J. Hajdu, Pseudospecific docking surfaces on electron transfer proteins as illustrated by pseudoazurin, cytochrome c550 and cytochrome cd1 nitrite reductase, Nature structural biology 2 (1995) 975-982.